MBE-Grown Long Wavelength InGaAlAs/InP Laser Diodes

by

Woo-Young Choi

Submitted to the Department of Electrical Engineering and
Computer Science
in partial fulfillment of the requirements for the degree of

Doctor of Philosophy in Electrical Engineering

at the

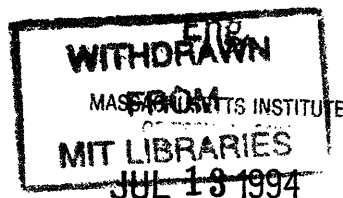MASSACHUSETTS INSTITUTE OF TECHNOLOGY

May 1994

Author . . . .
Department of Electrical Engineering and Computer Science
May 13, 1994

Certified by . . . .
Clifton G. Fonstad
Professor of Electrical Engineering
Thesis Supervisor

Accepted by . . . .
Frederic R. Morgenthaler
Chairman, Departmental Committee on Graduate Students

MBE-Grown Long Wavelength

InGaAlAs/InP Laser Diodes

by

Woo-Young Choi

Submitted to the Department of Electrical Engineering and Computer Science
on May 13, 1994, in partial fulfillment of the
requirements for the degree of
Doctor of Philosophy in Electrical Engineering

Abstract

An attempt was made to achieve high-performance $1.55\,\mu m$ semiconductor laser diodes based on the InGaAlAs material system with solid-source molecular beam epitaxy (MBE) technology. The primary motivation for this attempt was the possibility for enhanced QW laser performance with large conduction band offsets provided by InGaAlAs which, furthermore, can be realized with toxic-gas-free solid-source MBE technology. In order to realize this goal, the technique of growing high-quality InGaAlAs with MBE was first established and the resulting InGaAlAs bulk and quantum well samples were extensively characterized by double-crystal xray diffraction, transmission and photoluminescence measurements. $1.55\,\mu m$ graded-index separate-confinement strained multiple quantum well lasers were then designed, epitaxially grown, and fabricated into broad-area and ridge-waveguide devices. The resulting devices were characterized for their threshold currents and quantum efficiencies, and these were compared with other reported values obtained from different material systems and/or epitaxy techniques. In addition, in order to realize distributed-feedback (DFB) lasers that do not require any epitaxial regrowth, a novel ridge-waveguide DFB structure was proposed, analyzed, and fabricated with x-ray lithography. Finally, an assessment was made on the future of MBE-grown InGaAlAs lasers for the fiber-optic application.

Thesis Supervisor: Clifton G. Fonstad
Title: Professor of Electrical Engineering

Acknowledgments

Contents

List of Figures

6

9

List of Tables

Chapter 1

Introduction

The development of fiber-optic communication networks has been truly revolutionary in both a technological and a sociological sense. Technologically, the rapidity and forcefulness with which the fiber-optic technology has been installed in real applications are second to few of modern inventions. Less than thirty years after Kao and Hockman recognized in 1968 the possibility of light transmission through silica-based waveguides [1], the total length of installed fiber by the end of 1994 is estimated to be 14-million miles in the United States alone and 43-million miles in the entire world[1] [2]. It is also estimated that presently the US telephone industry alone installs about 125 miles of new fibers every hour [3]. All these vast amounts of fibers are bound to have great sociological impact. Perhaps this can be best illustrated by pointing out our ever-increasing dependence on telephones, facsimile machines, and electronic mail, and noticing the remarkable improvement in their service quality in recent years, which is largely due to newly installed fiber-optic networks. It is truly intriguing just to imagine what it will be like when the power of fiber optics is fully utilized with the realization of the so-called "national information infrastructure" in which high-performance fiber-optic networks will be widely available, even possibly to every single home as some proponents call for "fiber-to-the-home". It is not so extreme to believe that high-speed, highly intelligent, and highly user-friendly multi-

---

[1]By comparison, the circumference of the earth is about 25,000 miles.

media communication networks possible with fiber-optic technology will greatly, or even fundamentally, change the outlook of our society. In essence, the globe is becoming a much smaller and, hopefully, easier place to live with the tightening nets of optical fibers all over it.

There are clearly many factors responsible for the remarkable development of fiber-optic technology, but the successful realization of efficient and reliable light sources based on semiconductor laser diodes is, without doubt, a major one. Semiconductor laser diodes, another marvel of modern technological invention[2] by themselves, are compact, reliable, can be easily modulated, and provide light with the required wavelength for fiber-optic applications. This thesis is the results of efforts on the author's part – trivially small they may be in the context of the whole picture – to further improve the quality of semiconductor laser diodes used for fiber optics. In particular, an attempt was made to develop high performance laser diodes based on InGaAlAs material system with molecular beam epitaxy (MBE) technology. In the next sections, the motivations for this thesis work are discussed and a brief outline for this thesis is given.

1.1   Motivation: Why InGaAlAs?

In the current silica-based fiber-optic technology, the wavelength of choice is either $1.3\,\mu m$ where the fiber dispersion is minimum or $1.55\,\mu m$ where the loss is minimum. Light with such wavelengths can be obtained from the band-to-band radiative recombination process in semiconductor materials with proper band-gaps. The most widely used material system for fiber-optic application is the InGaAsP quaternary epitaxially grown on InP substrates. As is shown in Figure 1-1, the InGaAsP material system can cover the band-gap range from $1.35\,eV$ for binary InP to about $0.75\,eV$ for $In_{0.53}Ga_{0.47}As$, while maintaining lattice-matching to InP substrates. It can thus provide bulk or quantum wells (QWs) with the required band-to-band transition wavelength of 1.3 or $1.55\,\mu m$ as well as higher band-gap materials needed for

---

[2]For a description of the exciting early days of laser diode development, see [4]-[8].

InGaAsP, InGaAlAs Material Systems
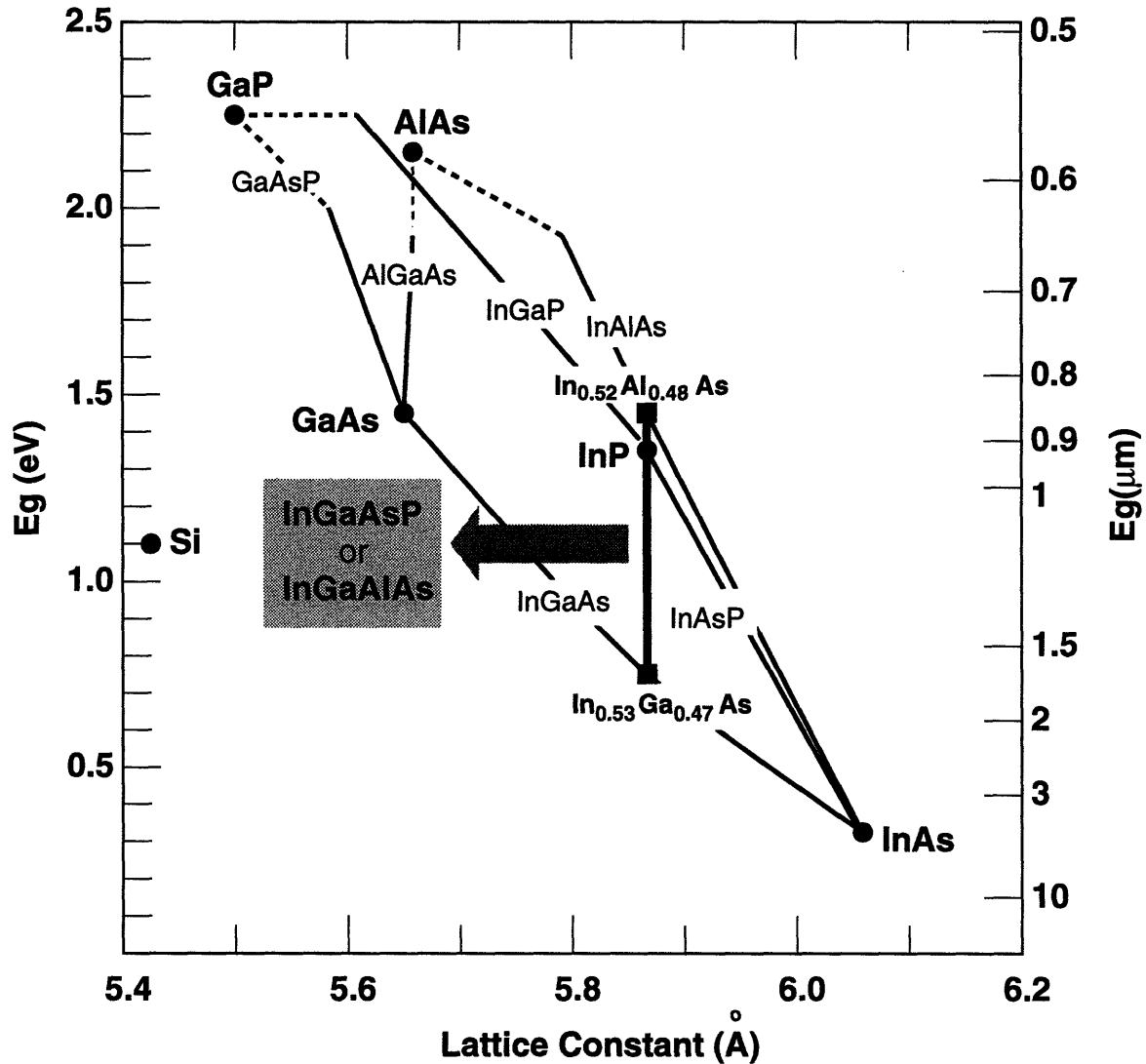
Figure 1-1: Band-gap vs. lattice constant diagram for material systems of InGaAsP and InGaAlAs. Binary (solid circles) and ternary (dotted lines for the indirect band-gap and solid lines for the direct band-gap) materials are shown that are the building-blocks for the quaternaries InGaAlAs and InGaAsP. (A portion of this figure was provided by J. Vlcek.)

optical and carrier confinement in a laser diode device structure. InGaAsP has been the material of choice for laser diode development for optical fiber applications from the early days of liquid phase epitaxy (LPE)-grown double heterostructure devices to today's state-of-the-art separate confinement heterostructure (SCH) strained multiple QW (MQW) devices. All the laser diodes that are currently deployed in the field are based on InGaAsP as well.

Our attempt, however, was to investigate the feasibility of using solid-source MBE technology to develop laser diodes for the same application based on an alternate material system of InGaAlAs lattice-matched to InP. The InGaAlAs material system can also scan the wavelength of interest for fiber-optic applications as seen in Figure 1-1. There are two reasons why one might consider InGaAlAs instead of InGaAsP [3]:

First, InGaAlAs has only one Group V element. In solid-source MBE, it is difficult to have good control over the material composition if more than one Group V element are involved as is the case for InGaAsP. In addition, phosphorus with its high vapor pressure has been very difficult to handle for solid-source MBE applications. As a result, if one wants to make laser diodes with solid-source MBE technology, InGaAlAs is a much easier material to deal with than InGaAsP. In fact, this is why the very earliest investigations into InP-based QW lasers were done with MBE-grown InGaAlAs [9] since it provided much better thickness and composition control which is particularly important for QWs. One might wonder why we should pursue lasers with solid-source MBE rather than LPE or gas-source MBE or metalorganic chemical vapor epitaxy (MOCVD). Although solid-source MBE has certain advantages in that it offers superior growth control over LPE and is free of toxic gases which have to be used in gas-source MBE or MOCVD, the choice of solid-source MBE for the present study was due to the constraint that only solid-source MBE was accessible to us. The goal was to see how far we can go within this given constraint.

Second, heterojunctions made with InGaAlAs materials have larger conduction band offsets than those with InGaAsP: close to 70 % of the total band offset resides

---

[3]It should be noted that these are reasons that were formulated at the beginning of this study a few years ago. These motivations are re-evaluated in the conclusion chapter with knowledge and insight obtained from the present study.

InGaAlAs QW   vs   InGaAsP QW
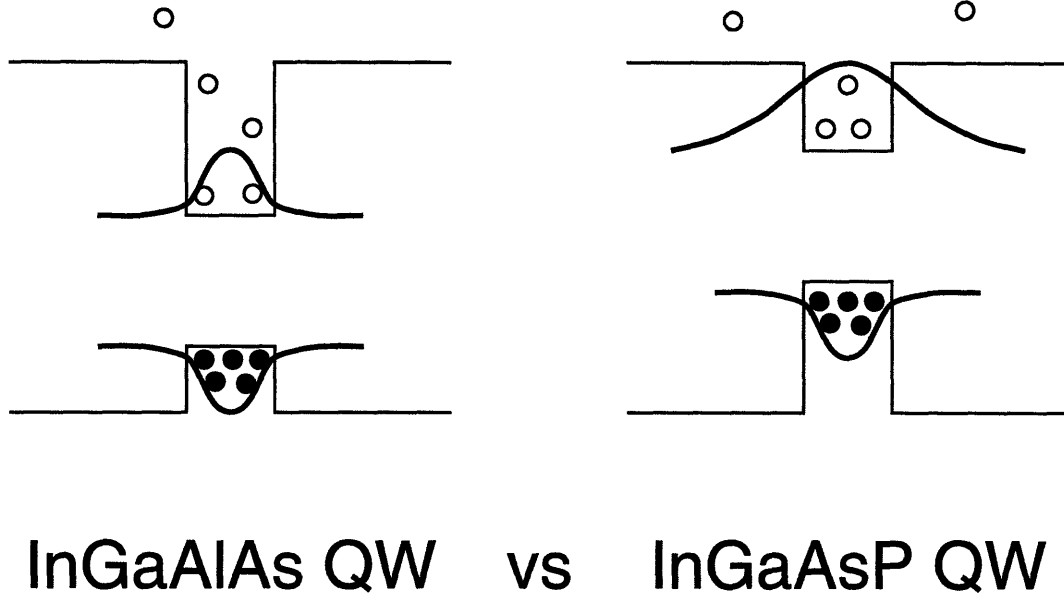
Figure 1-2: A schematic illustration for the advantages of InGaAlAs QWs over In-GaAsP. Holes with their large effective masses are well confined in both InGaAlAs and InGaAsP. Electrons, however, with small effective masses, are less likely to spill out of a InGaAlAs QW with larger barrier height than of a InGaAsP QW. In addition, electrons in a InGaAlAs QW, due to their better confinement, have wave-functions more symmetric to hole wave-functions, and this results in a larger optical transition probability for a InGaAlAs QW.

in the conduction band for InGaAlAs heterojunctions whereas only less than 40 % for InGaAsP [10]. This difference results in better electron confinement for InGaAlAs-based QWs than InGaAsP QWs. In QW laser diodes, efficient confinement of electrons is harder to achieve than holes since electron effective masses are much smaller. Consequently, larger barrier height for electrons is quite beneficial. Tightly confined electrons due to a larger barrier height enhance the carrier injection efficiency since they are less likely to "spill" out of QWs [11], and provide a larger electron-hole overlap integral with more symmetric electron and hole wave functions [12]. These two points are schematically illustrated in Figure 1-2. These can improve the laser device performance, and our goal was to investigate if these advantages can indeed be utilized for better performing InGaAlAs lasers.

1.2 Thesis Outline

Making high performance laser diodes requires expertise in several different disciplines. In particular, one should be able to grow high quality epitaxial materials and confirm their quality by various material characterization techniques, should have a good understanding of laser device physics so that one can design the required device layer structure, should be able to process epitaxially grown materials into complete devices, and should be capable of doing various device characterization measurements. Acquiring the necessary expertise to skillfully perform these four different elements was basically what was done for this thesis work. Figure 1-3 schematically illustrates this point along with some of the highlights that were achieved in the present study.

This thesis consists of five chapters including one for this introduction and one for the conclusion. The second chapter deals with the issues related to MBE growth and material characterizations. Basic principles of material characterization techniques utilized in the present study are briefly described, and examples of characterizations performed to find the optimal growth conditions and to determine certain physical parameters of strained MQW samples are discussed. In the third chapter, basic physics of strained QW lasers is briefly explained and issues investigated in depth for the actual implementation of strained QW lasers are discussed. In addition, laser diode fabrication processes and the resulting device characterizations are described. In the fourth chapter, a newly proposed ridge-waveguide distributed-feedback laser is introduced, and the results of numerical calculations of grating coupling coefficients as well as the actual fabrication with x-ray lithography are given.

MBE Growth of High Quality InGaAlAs

Material Characterizations

- X-ray Diffraction
- PL
- Absorption

GRIN-SCH Strained MQW Lasers

Ridge Waveguide DFB Lasers

Materials —————————— **Device Design**

Good Laser Devices

Processing —————————— **Device Characterization**

Broad-Area Lasers

Ridge Waveguide Lasers

  with AlAs Etch Stop Layers

Ridge Waveguide DFB Fabricated

  with X-ray Lithography

Light-vs-Current Measurement

Far-Field Measurement

Spectrum Measurement

Figure 1-3: A diagram showing four elements required for achieving good laser diodes. Also shown are some highlights of results achieved in the present study.

Chapter 2

Growth and Characterization of InGaAlAs Materials

The first step toward achieving high performance InGaAlAs laser diodes grown by MBE is realizing high quality MBE-grown InGaAlAs materials. This necessitates development of MBE growth techniques that provide high quality InGaAlAs materials, and skillful utilization of material characterization techniques with which qualities of MBE-grown materials can be assessed. These are the topics discussed in the chapter. In Section 2.1, a brief description is given of the MBE machine used in the present study. This description is limited to the features that are unique to us, leaving a general introduction to MBE technology to other excellent references [13]. InAlAs latticed-matched to InP, with high percentage of aluminium, is the most difficult material to grow with MBE, and a systematic study was done in order to optimize the MBE growth conditions for best-quality InAlAs. This study is discussed in Section 2.2. The most important material characterization technique for InGaAlAs epitaxy growth is perhaps the x-ray diffraction measurement which provides information on how close the compositions of resulting materials are to the target values. This information is then fed back to the subsequent growth as correction factors for a better control in composition. For this purpose, x-ray measurements were routinely done on just about all the MBE-grown samples in the present study. With double-crystal x-ray diffraction (DCXRD), the measurement accuracy is further enhanced and some

in-depth structural analyses of various layer structures are possible. Such analysis was done for a strained MQW structure and the results are discussed in Section 2.3. Optical characterizations such as photoluminescence (PL) and transmission measurements are also routinely done to assess the optical quality of epitaxially grown materials. With an understanding of some simple theories, it is possible to do in-depth studies into the physical nature of involved optical transitions. In Section 2.4, the results of such in-depth studies into excitons in strained MQWs by transmission and PL measurements are discussed.

2.1 MBE

Our MBE machine is a Riber 2300R model that was purchased in 1983. It consists of three chambers: growth and preparation chambers and a home-built loading chamber. Figure 2-1 schematically shows the MBE machine. The unique features in our machine are as follows. It can handle up to seven 2-inch wafers (or smaller pieces indium-bonded on molybdenum blocks) in one loading. It has a total of eight cells including two gallium and two aluminium cells, and an arsenic valved cracker. It also has a control software which can in principle automate the entire growth sequence once the sample is loaded into the growth chamber. This software was originally home-designed [14] but now is commercially available [15]. Our growth techniques of InGaAlAs on InP is not much different from the usual practices and examples of our standard growth and maintenance procedures can be found in [16].

One thing unique to us is our growth temperature calibration procedure. In MBE growth, the growth temperature is an extremely important parameter and has to be accurately controlled. The temperature is usually measured by a pyrometer which itself has to be calibrated, and the method of pyrometer calibration varies from one laboratory to another. In our case, we utilize the characteristic change in the reflection high-energy electron diffraction (RHEED) pattern from Group-V-stable to Group-III-stable condition. During the substrate temperature ramp-up before growth is initiated, the [110] azimuth RHEED pattern from the InP substrate under arsenic
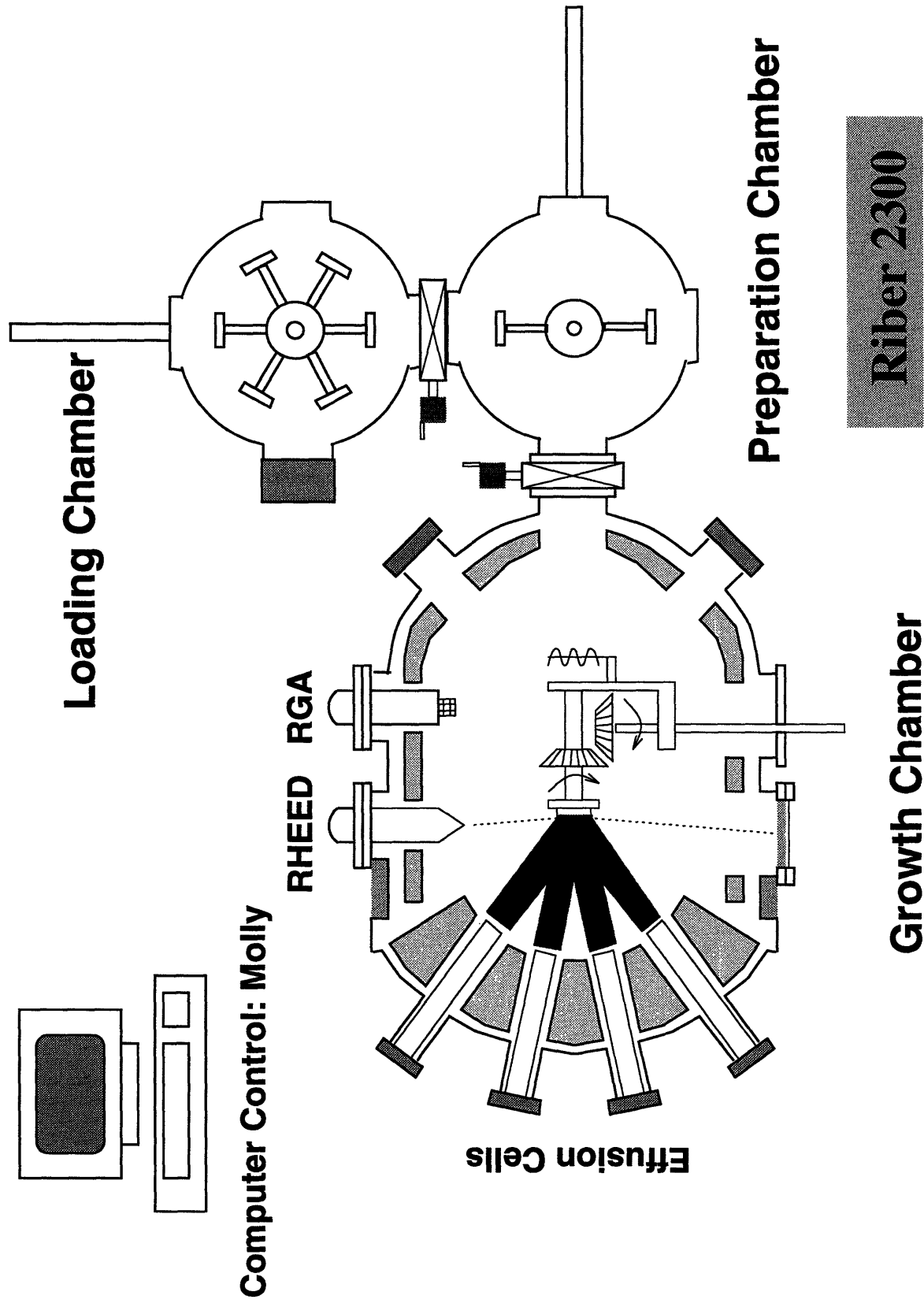
Figure 2-1: A schematic drawing of the MBE machine used in the present study. (A portion of this figure was provided by J. Vlcek.)

overpressure shows a change from 2x to 4x pattern at a characteristic temperature, and from the corresponding pyrometer temperature, pyrometer calibration can be done. This characteristic change in the RHEED pattern is usually abrupt and the transition temperature can be obtained repeatably within a few degrees of accuracy. Caution should be taken, however, since this characteristic temperature depends on the amount of arsenic overpressure as well as the substrate dopant types. The dependence on arsenic overpressure is an expected result since the transition from Group-V-stable to Group-III-stable surface should depend on the amount of arsenic available on the surface. In order to quantify this dependence, measurements of the RHEED transition temperatures were done under different arsenic overpressure values, and the results are shown in Figure 2-2. Also shown are the RHEED transition temperatures for InGaAs and InAlAs. These measurements were done while growing InGaAs and InAlAs on InP substrates with the growth rate of about $0.65\,\mu$m per hour. Determination of these transition temperatures for InGaAs and InAlAs is important since these are the high temperature limits for the arsenic-stable condition, an usual requirement for successful MBE growth of arsenides. The dependence of the RHEED transition temperature on the dopant types in InP substrates is presently not fully understood. Specifically, InP:S substrates have about 20 to 25 °C higher transition temperature than InP:Fe substrates. Two explanations are possible. First, the difference in the transition temperature is a true difference caused by some different surface state transition processes with sulfur and iron impurities. Second, the difference is a measurement error caused by possibly different amount of infra-red absorption due to InP:S and InP:Fe substrates. Although no careful experiments have been performed to determine the correct cause, there is an observation favoring the first explanation that the transition temperature of the epitaxially grown InGaAs or InAlAs does not depend on the substrate type.
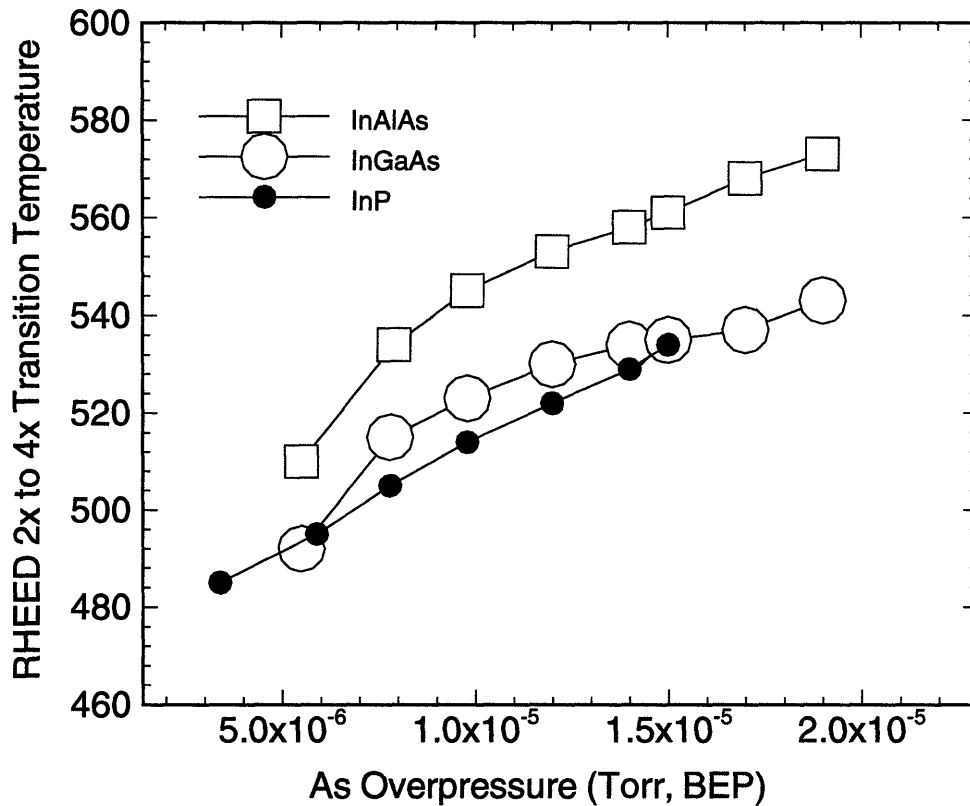
Figure 2-2: RHEED transition temperatures for InP substrate (InP:Fe), InGaAs and InAlAs at different As overpressure values. For InGaAs and InAlAs, the growth rate was about $0.65\,\mu$m per hour. Measurements were done while ramping up the growth temperature at a rate of 20 °C/min under given arsenic overpressure. The initial calibration of pyrometer was done according to the RHEED pattern change at the congruent sublimation temperature of GaAs, 640 °C. The As BEP values may have some errors since they were converted from the growth chamber pressure rather than measured with the flux ion gauge, which at the time of measurement was not functional.

2.2 MBE-Growth Optimization for InAlAs

The material quality of epitaxial InAlAs is known to suffer from the high reactivity of Al with oxygen-containing residual species [17], and alloy clustering [18, 19] presumably due to the large difference in In-As and Al-As bond energies. Consequently, MBE growth conditions that minimize these degrading effects need to be established before high performance device structures with InAlAs can be achieved. In growing InAlAs with an MBE machine that has ultra clean vacuum and high source purity, one has two controllable growth parameters that significantly affect the resulting material quality: substrate temperature and As overpressure. The task is, then, obtaining the optimal combination of these two that gives the best material quality. For this goal, InAlAs samples were grown by MBE with different combinations of growth temperature and As overpressure, and characterized by DCXRD measurements for the evaluation of crystalline quality, Hall measurements for electrical quality, and PL for optical quality. The results discussed in this section are also published in Reference [20].

2.2.1 MBE Growth

Five different growth conditions were selected within arsenic-stable growth condition, as shown in Figure 2-3, that correspond to five combinations of two different values of As overpressure at 8×10^{-6} and 1.5×10^{-5} Torr BEP, and three different temperatures at 475, 525, and 555 °C. Five 0.65-μm-thick InAlAs samples were grown under these conditions on the same day using pieces from the same (001) InP:Fe substrate. The InAlAs layers were intentionally doped with the identical amounts of Si at about 5×10^{16} cm^{-3}, the activation of which depends on growth conditions employed [21]. All the samples were capped with about 10-nm-thick undoped In$_{0.53}$Ga$_{0.47}$As so that any InAlAs surface oxidation is prevented and also the contact resistance for Hall measurement is reduced. In anticipation of enhanced In-desorption at higher growth temperature that may affect our investigation, Sample L2, H2, and H3 were grew with 4 °C higher (737 °C) In effusion cell temperature than Sample L1 and H1 (733 °C)

25
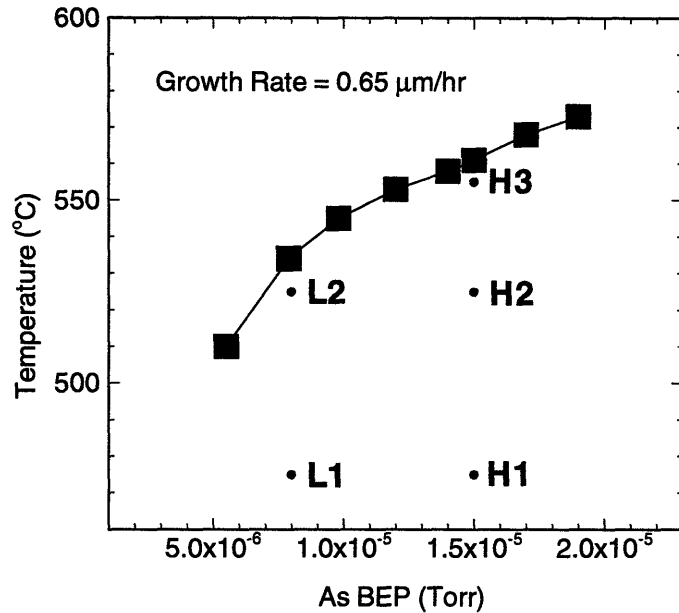
Figure 2-3: Five different growth conditions investigated with their ID's that are used in the text. Also shown are the As-rich to Group-III-rich transition temperature for InAlAs.

while the same Al cell temperature of 1042 °C was kept. The surfaces of all resulting samples were mirror-like with few defects observable under Nomarski microscopy.

2.2.2 Characterizations and Discussions

Three different DCXRD measurements were done on three different spots on each sample, and the average values of substrate and InAlAs peak separations and InAlAs peak full-width-at-half-maximum (FWHM) were determined. The details of DCXRD measurement set-up is given in Section 2.3. Figure 2-4 shows the amounts of InAlAs lattice mismatches determined from the x-ray peak separations, where the magnitudes of mismatches are no more than 1.03×10^{-3} (for H3) for all five samples. Also shown in the figure are the values of In cell temperature that would be required for perfectly lattice-matched InAlAs on InP with Al cell temperature fixed at 1042 °C. These values were estimated from the mismatch values shown and the measured In flux activation energy. It can be seen from the figure that As overpressure has little effect on lattice-matching for the range investigated here, but higher growth temperature
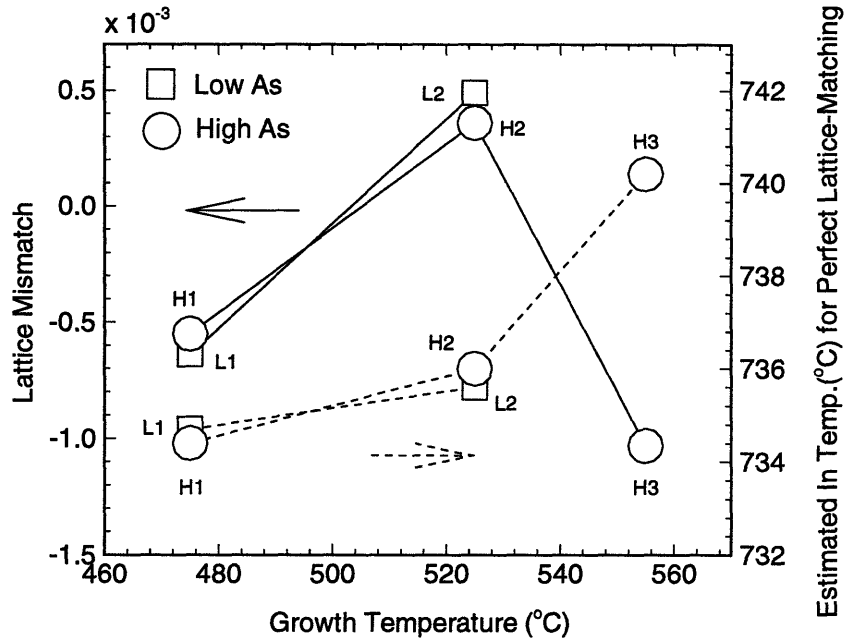
Figure 2-4: Lattice mismatches of five samples measured by DCXRD. Also shown is the estimated indium cell temperature that would be required for perfectly lattice-matched InAlAs on InP for each set of growth conditions.

causes enhanced In desorption and requires higher In cell temperature. This has a significant consequence in that one has to control growth temperature as well as effusion cell temperature in order to grow satisfactorily lattice-matched InAlAs on InP.

Figure 2-5 shows the results of material characterizations performed on different samples: top, DCXRD FWHM and 77 K Hall mobility and bottom, 10 K PL FWHM and integrated PL intensity. Hall measurements were done on about 0.5 cm by 0.5 cm van der Pauw samples with In dot contacts. PL measurements were done for three different spots from each sample, and the average values are shown. From these results, the following observations can be made: First, InAlAs qualities are better if grown under high As overpressure than low As, as can seen from the better qualities observed for H1 than L1, and H2 than L2. This is believed due to reduced As vacancies and/or reduced alloy clustering at high As overpressure. High As overpressure is expected to reduce alloy clustering since, with the resulting lower surface adatom mobilities, it can reduce the thermodynamically favored phase separation between
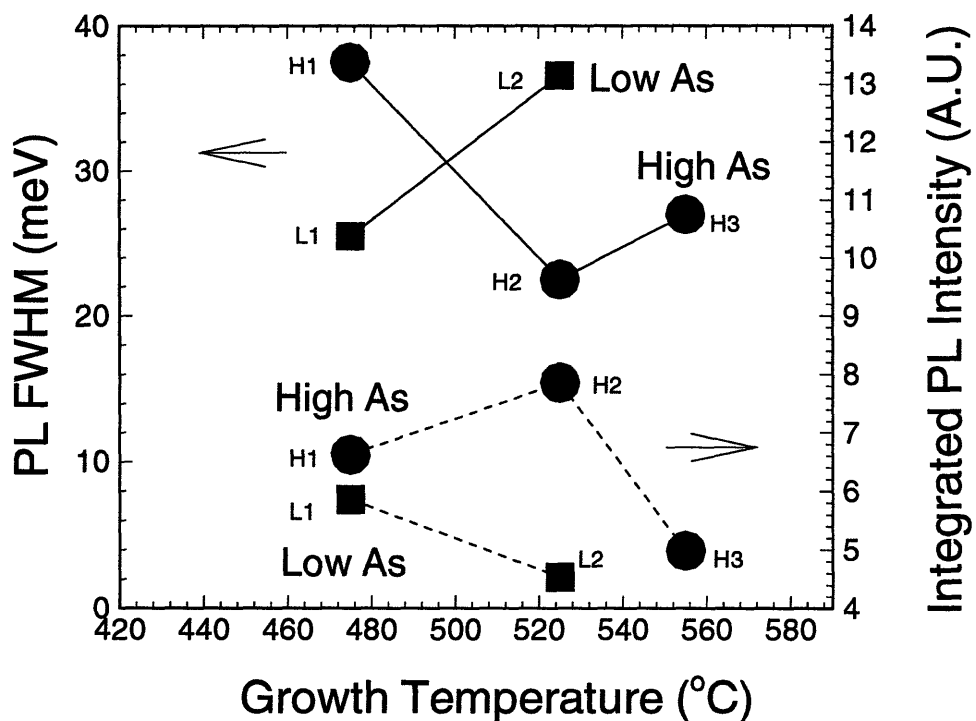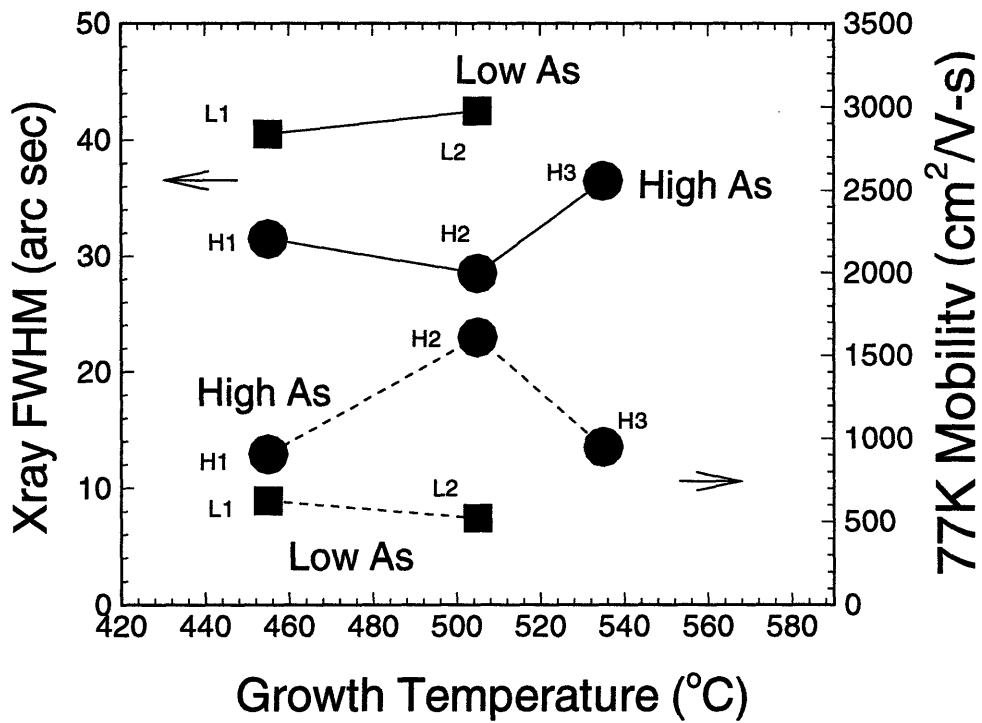
Figure 2-5: Results of various material characterizations for InAlAs grown under different conditions: top, DCXRD FWHM and 77 K Hall mobility and bottom, 10 K PL FWHM and integrated intensity.

InAs and AlAs. The only exception to this observation is PL FWHM where H1 has larger FWHM than L1, the cause of which is not presently known.

Second, InAlAs qualities are better if grown at high temperature given sufficient As overpressure, as can be seen by comparing qualities of H1 and H2. This is believed due to reduced impurity incorporation at high growth temperature. However, if growth temperature is too high causing a significant amount of As desorption, then the advantage of high growth temperature is offset by the degrading effects of As vacancies and/or enhanced alloy clustering. This can be seen from the poor qualities of H3 and L2. These two observations qualitatively agree with the results of Welch *et al.* who investigated the optical quality of InAlAs grown under different conditions [22].

It should be noted that the above x-ray FWHM data are considerably better than other reports: for example, that of Tournié *et al.* who obtained x-ray FWHM values comparable to the present work only if InAlAs layers were grown at very high temperature of 600 °C, or on top of a thick InGaAs or a InGaAs/InAlAs superlattice buffer [23]. As a summary, growth temperature of 525 °C and As overpressure of 1.5×10^{-5} Torr BEP gave the best InAlAs quality within the investigated range. This condition is believed to provide a sufficient amount of As to the growth surface, and reduces impurity incorporation. In addition, this growth temperature does not severely suffer from In desorption, which makes the task of lattice-matching more reliable.

2.3 DCXRD Characterization of Strained MQW

The utility of x-ray diffraction for the structural assessment of epitaxially grown semiconductor layers is well established. Among layer structures characterized by x-ray diffraction, those with MQWs or superlattices have received much attention since quantum confinement effects in such structures are the basis of many advanced heterostructure devices. In x-ray investigation of these structures, the compositions and thicknesses of wells and barriers can be accurately determined from the analysis of satellite peaks caused by the artificially added periodicity [25]. In this section, x-

ray investigations are discussed of compressively strained InGaAs MQW embedded in thick nominally lattice-matched top and bottom cladding layers, as used in the laser diode device structures. The result of this investigation is published in Reference [24].

Figure 2-6 shows two layer structures investigated by DCXRD in this section with their target composition and thickness values. Sample A is a p-i-n structure with four compressively strained QWs and quaternary InGaAlAs barriers and claddings of the same composition. Sample B is an actual device structure for graded-index separate confinement (GRINSCH) strained MQW laser diodes. All InGaAlAs quaternary layers have the same target composition as shown at the bottom of the figure. The GRINSCH layers in Sample B are linearly graded from $In_{0.52}Al_{0.48}As$ to $In_{0.52}Ga_{0.20}Al_{0.28}As$. InGaAs and InAlAs layers have the lattice matching target compositions, $In_{0.53}Ga_{0.47}As$ and $In_{0.52}Al_{0.48}As$, respectively. The goal of DCXRD investigation is to determine the compositions and thicknesses of wells and barriers in these structures. The samples are two of many samples with different strained MQW structures grown in order to optimize the strained MQW structure for 1.55 μm laser diodes.

The DCXRD measurements were done on a commercially available Bede Model 300 system from Bede Scientific Instruments Limited. Figure 2-7 schematically shows the DCXRD measurement set-up. The Cu-Kα radiation was generated by a Rigaku RU200 generator with the bias voltage and the beam current set at 60 kV and 200 mA, respectively. An InP substrate oriented for the (004) reflection was used for the first crystal. Rocking curves were measured for symmetric (004) reflection with the goniometer increment of two arc seconds and the count time of two seconds.

Figure 2-8 shows measured and simulated DCXRD spectra of Sample A (the details of the simulation are discussed later). The satellite peaks in the data show the $(\sin(4x)/\sin(x))^2$ dependence predicted by the theory [26, 27]. In order to analyze this data, it is first necessary to understand how x-ray diffraction from embedded strained MQW's is affected by the surrounding claddings. This is done by separating

Sample A		**Sample B**
		$Be = 1x\ 10^{19}$ 200 nm InGaAs
150 nm InGaAlAs	Top Cladding $Be = 5 \times 10^{17}$	1300 nm InAlAs
50 nm InGaAlAs	UID	150 nm InGaAlAs Graded
Well: 7 nm $In_{0.7}Ga_{0.3}As$ Barrier: 10 nm InGaAlAs	4 wells and 3 barriers UID	Well: 6 nm $In_{0.66}Ga_{0.34}$ As Barrier: 10 nm InGaAlAs
50 nm InGaAlAs	UID	150 nm InGaAlAs Graded
150 nm InGaAlAs	Bottom Cladding $Si = 5 \times 10^{17}$	650 nm InAlAs
InP:Fe		InP:S
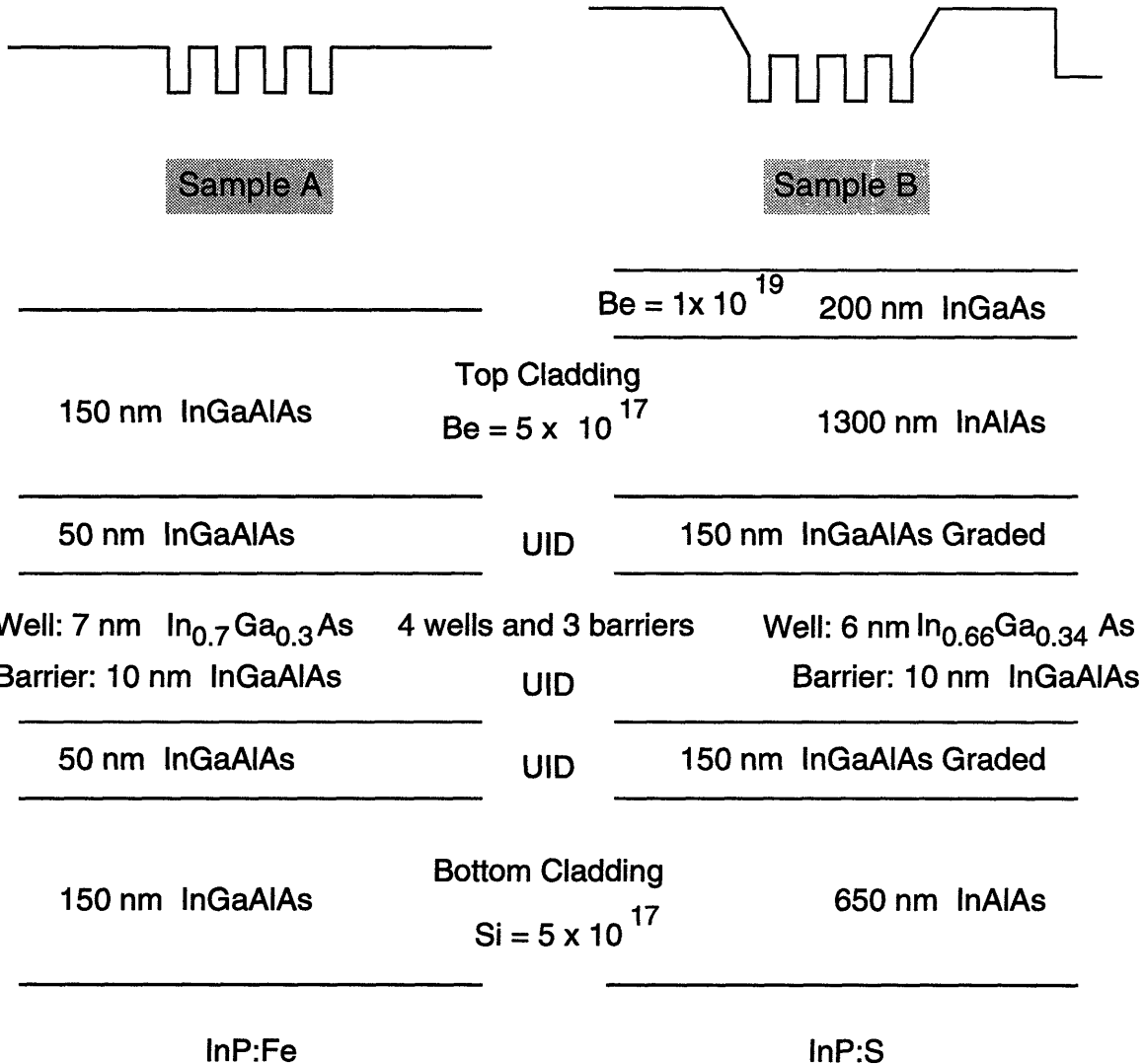
Quarternary Composition: In(0.52)Ga(0.20)Al(0.28)As

Figure 2-6: Target layer structures of two samples used for DCXRD investigation.

31
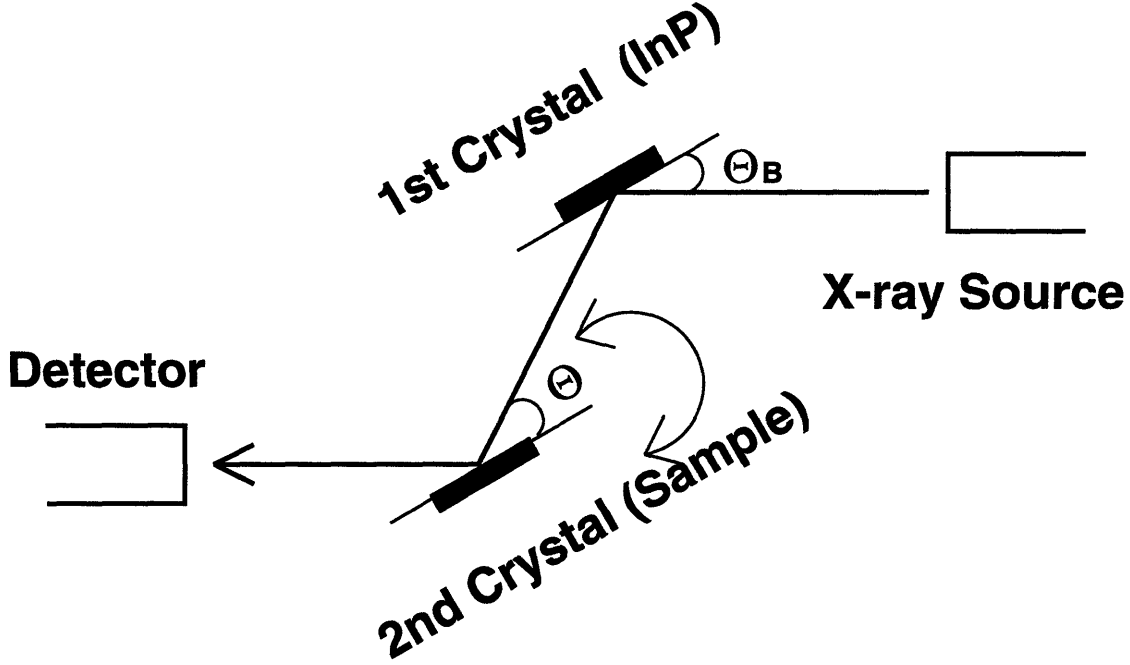
Figure 2-7: A schematic drawing for the DCXRD measurement set-up.

the total diffracted x-ray field into three different parts as

$$E_{total}(\Theta) = E_b(\Theta) + E_{mqw}(\Theta)\exp(iT_b) + E_t(\Theta)\exp(i(T_b + T_{mqw})) \qquad (2.1)$$

where E_b and E_t correspond to the diffracted x-ray fields due to the bottom and top cladding layers, respectively, and E_{mqw} to that of the MQW region. E_b, E_t and E_{mqw} are in general complex quantities and depend on the incident x-ray angle, Θ. For our analysis, only one polarization is considered and the dynamic effects are not considered. T_b and T_{mqw} are the layer thicknesses of the bottom cladding and the MQW region, respectively. Notice that T_{mqw} is defined as the thickness of four wells and four barriers. Phase factors are introduced to account for the spacial shifts of the MQW region and the top cladding layer. This separation is shown schematically in Figure 2-9. The measured x-ray intensity is then

$$|E_{total}|^2 = |E_b|^2 + |E_{mqw}|^2 + |E_t|^2 + 2|E_bE_{mqw}|\cos(T_b + \theta_{b,mqw})$$

$$(2.2)$$

$$+2|E_bE_t|\cos(T_b + T_{mqw} + \theta_{b,t}) + 2|E_{mqw}E_t|\cos(T_{mqw} + \theta_{mqw,t})$$

32

Figure 2-8: Measured and simulated DCXRD scans of Sample A. The input parameters for simulation determined from the analysis are shown in the figure.

$$E_b \qquad E_{mqw} \exp(iT_b) \qquad E_t \exp(i\,(T_b + T_{mqw}\,))$$

$$|\!\!\leftarrow\!\!- - - - - - - - - - - - - -\!\!\rightarrow\!\!\leftarrow\!\!- - - - - - - - - -\!\!\rightarrow\!\!\leftarrow\!\!- - - - - - - - - - -\!\!\rightarrow\!\!|$$

$$T_b \qquad\qquad T_{mqw} \qquad\qquad T_t$$

Figure 2-9: A diagram for separating an embedded strained MQW structure into three different regions: bottom cladding, wells and barriers, and top cladding.

where $\theta_{b,mqw}$, $\theta_{b,t}$ and $\theta_{mqw,t}$ represent the phase differences between corresponding x-ray fields. From the above expression, it can be easily observed that the product terms representing coupling between x-ray fields from different layers have significant contributions only in the range of Θ where $|E_b|$ or $|E_t|$ is significant. In typical DCXRD scans of embedded strained MQW structures, most dominant satellite peaks are located away from the cladding peak and, consequently, they are easily resolvable and can be described by the analytical expression derived for MQWs without cladding layers [26, 27]. This is different from the case of lattice-matched MQWs embedded in thick cladding layers in which the satellite peaks are not as easily resolvable and suffer more severe interference from the cladding layers. Although the effect of the substrate is neglected in the above analysis, it can be treated just like another cladding layer and the same results can be obtained.

For the complete determination of the strained MQW structure in Sample A, it is necessary to determine four independent parameters: well composition, or the vertical lattice spacing inside the wells $(a_{\perp,w})$; well thickness, or the number of monolayers inside the wells (N_w); barrier composition, or the vertical lattice spacing inside the barriers $(a_{\perp,b})$; and barrier thickness, or the number of monolayers inside the barriers (N_b). It is assumed that all of the wells and barriers are of identical composition and thickness, a situation which can be easily achieved with MBE. Further, it is assumed that there is no strain relaxation inside the wells and all the strains are coherently incorporated by tetragonal distortion. This is evidenced by the sharp satellite peaks

34

in the DCXRD scan and a narrow and strong excitonic PL peak with full width at half maximum of 6.5 meV at 10 K from Sample A. The task is then reduced to obtaining four independent equations involving the above four parameters. This can be done in the following manner:

1. Since the barriers and claddings are of the same composition, $a_{\perp,b}$ can be determined from the separation between cladding and substrate peaks in the DCXRD scan.

2. The position of the zeroth-order satellite peak should correspond to the average vertical lattice spacing in the strained MQW region, $a_{\perp,0}$, or

$$a_{\perp,0} = \frac{N_w \times a_{\perp,w} + N_b \times a_{\perp,b}}{N_w + N_b} \qquad (2.3)$$

where $a_{\perp,0}$ can be easily determined from the position of the zeroth-order satellite peak. If the zeroth-order peak is located close to the cladding peak, then the positions of higher order peaks can be used to determine the correct zeroth-order peak position without the interference of the cladding layers.

3. From the known expression for the satellite peak periodicity [27], we obtain

$$\Lambda = \frac{\lambda}{2\cos(\theta)\Delta\theta} \qquad (2.4)$$

where Λ is the spacial periodicity in MQWs ($= N_w d_w + N_b d_b$), λ x-ray wavelength, $\Delta\theta$ the separation between two adjacent satellite peaks, and θ is the angle around which the satellite peak separation is determined.

4. Finally, the total epilayer thickness t can be expressed as

$$t = \gamma N_b a_{\perp,b} + n\Lambda \qquad (2.5)$$

where n is the number of quantum wells and γ corresponds to the ratio of the total cladding thickness to the barrier thickness which can be easily determined from the target growth durations for claddings and barriers. The total epilayer

35

thickness can be measured by a profilemeter measurement on a step created by selectively etching the epilayer.

By simultaneously solving the above four equations, it is possible to uniquely determine all four parameters, $a_{\perp,w}$, N_w, $a_{\perp,b}$, and N_b. To determine the quaternary composition for barriers and claddings from $a_{\perp,b}$, the bandgap of the quaternary was measured from low temperature PL (1.10 eV at 10K) and the corresponding composition was calculated. The resulting layer structure is 73 Å $In_{0.692}Ga_{0.308}As$ for the wells and 98 Å $In_{0.550}Ga_{0.196}Al_{0.254}As$ for the barriers. Using these values, a simulation was done with a commercially available software package called RADS (Rocking Curve Analysis by Dynamic Simulation) supplied by Bede Scientific Instruments Limited, and the result is shown in Figure 2-8. No iterative changes in input parameters were performed to obtain better matching between measurement and simulation. The matching as shown is excellent, indicating the accuracy of the present analysis. It should be noted that the determined values are the average values over the sample area probed by the x-ray beam, which is about 1 mm by 1 mm.

To estimate the margin of error involved in the analysis, an error analysis was performed. The major sources of uncertainties were considered to be in determining the exact peak positions from the x-ray data ($\pm$ 10 arc seconds in an enlarged figure) and the epilayer thickness from a profilemeter measurement ($\pm$ 100 Å or about $\pm$ 2 %). By calculating compositions and thickness from the input parameters that span the entire uncertainty range, histograms of possible compositions and thicknesses were obtained. From these, it can be said that the well indium composition is in the range of 0.692 $\pm$ 0.005 (or $\pm$0.7 %) with 79 % confidence, and the well and barrier thicknesses are 73 $\pm$ 2.5 Å(or $\pm$ 3.4 %) and 98 $\pm$ 2.5 Å(or $\pm$ 2.6 %), respectively, both with 73 % confidence. The larger margin of error in thickness than composition is due to the large uncertainty in thickness measurement by the profilemeter, which is the accuracy limiting factor.

Figure 2-10 shows the results of DCXRD measurement and simulation for a complete laser diode structure of Sample B. Due to the complex layer structure, the entire layer structure can not be determined by DCXRD results alone. However, the same

Wells: 6.2 nm $In_{0.656}Ga_{0.344}As$

Barriers: 9.8 nm $In_{0.550}Ga_{0.196}Al_{0.254}As$

Claddings: $In_{0.551}Al_{0.449}As$

Simulation
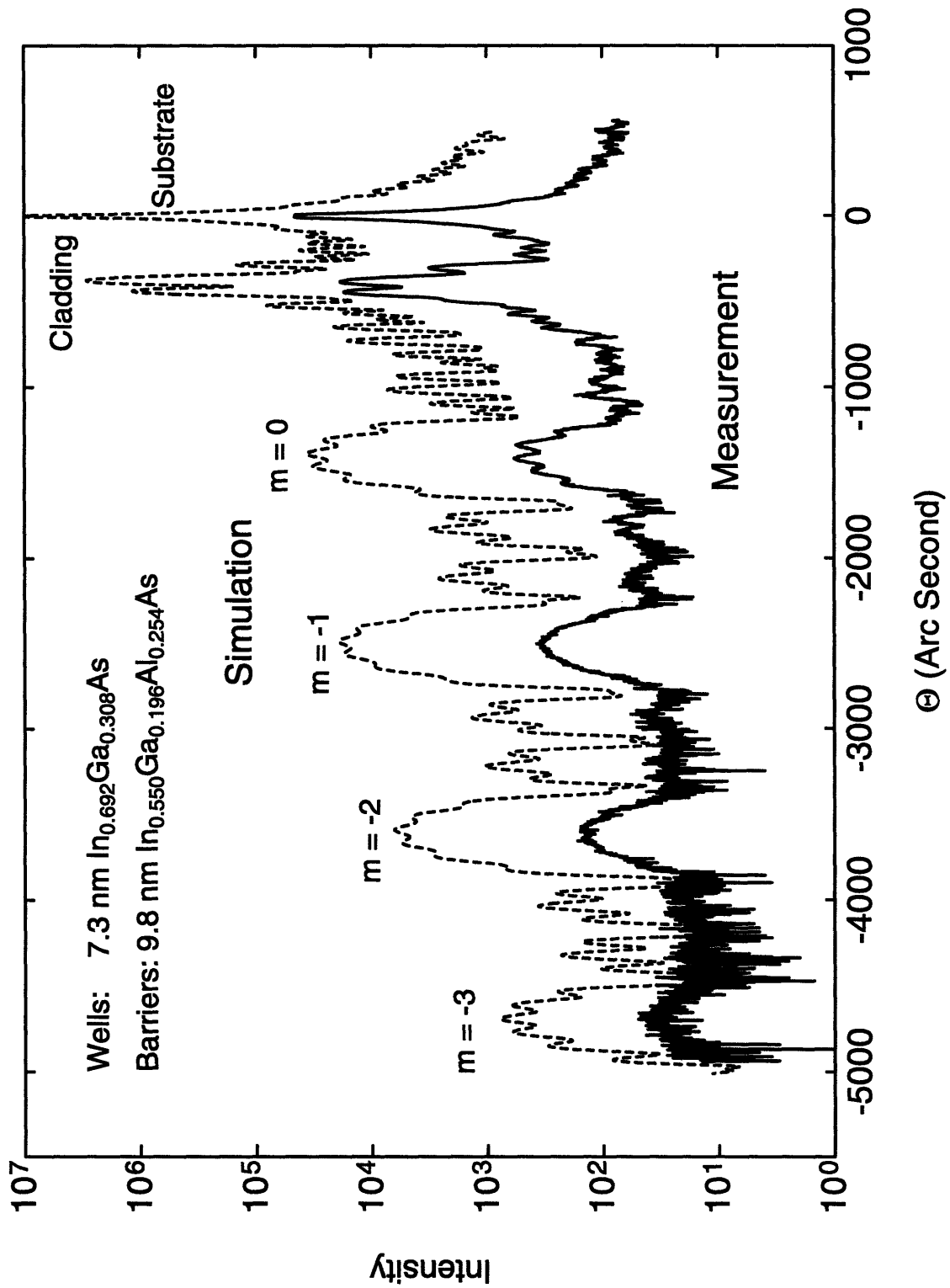
Measurement

Θ (Arc Second)

Intensity
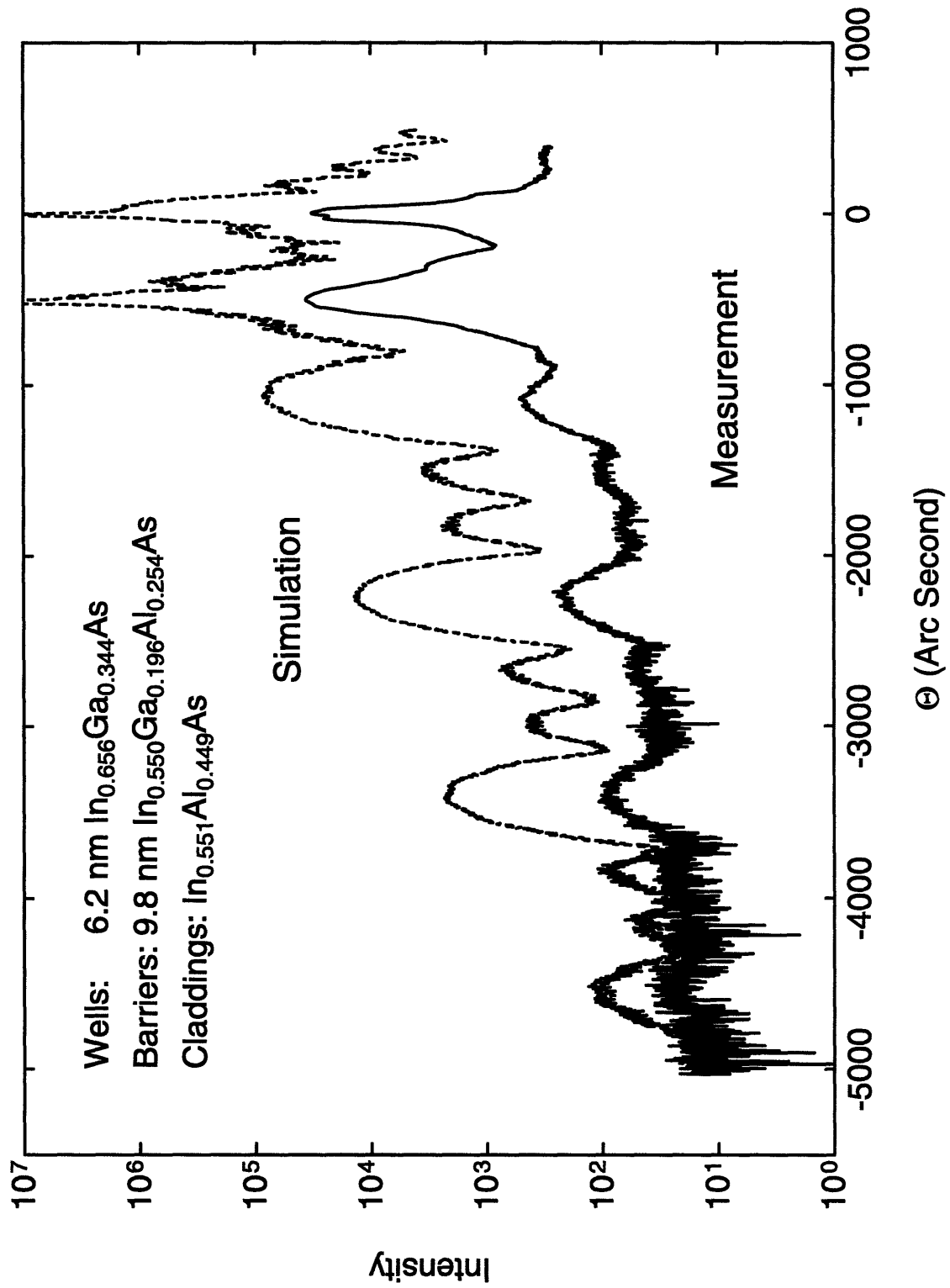
Figure 2-10: Measured and simulated DCXRD scans of Sample B. The input parameters for simulation that are determined from the analysis are shown in the figure.
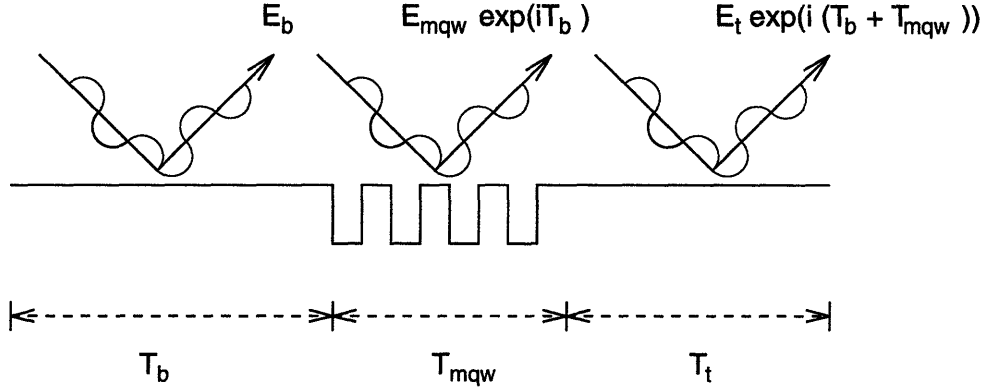
values for barrier composition and thickness as in Sample A can be used for Sample B, since both samples were grown on the same day with the same target values for barrier composition and thickness. Also, it can be assumed without too much difficulty that the initial 98 Å of the top GRINSCH region has the same composition as the barrier, providing four complete quantum wells and barriers as required. Two remaining conditions are obtained from the satellite peak periodicity and the zeroth-order satellite peak position. Then, the laser diode active region structure can be completely determined, as shown in Figure 2-10. For the simulation, the top contact layer was assumed to be lattice-matched ($In_{0.53}Ga_{0.47}As$) and the top and bottom GRINSCH regions were each modeled by five layers of constant compositions linearly varying from the barrier quaternary to InAlAs cladding. With the exceptions of the broader cladding layer peak and larger background noise, the agreement between measurement and simulation is excellent, indicating the accuracy of the analysis for a complete laser diode structure.

By comparing the target layer structure with that determined by DCXRD, we can verify that the effusion cell temperatures were set correctly for desired material compositions with the exception of the aluminium cell, whose temperature should have been higher by about 6 °C. This information can be used for the subsequent MBE growths for a better control of cell temperatures. In addition, the accurate device structure determination by DCXRD as was done for Sample B is essential for the correct analysis of device characteristics. In these regards, DCXRD characterization is essential for successful growth of InGaAlAs materials on InP and, in particular, for strained MQWs for device applications.

2.4 Characterization of Excitons in Strained MQWs

Excitons in quantum wells have received much attention in recent years. This is because investigations of excitonic transitions provide valuable information for better understanding of QW physics, and there exists a large potential for utilizing enhanced excitonic effects in QWs for practical device applications. The properties of excitons

$In_{0.47}Ga_{0.255}Al_{0.275}As$	120 nm	$Be = 5 \times 10^{17}$
$In_{0.47}Ga_{0.255}Al_{0.275}As$	40 nm	UID
Well: $In_{0.652}Ga_{0.348}As$	A:2.5, B:5.0, C:7.5 nm	UID
$In_{0.47}Ga_{0.255}Al_{0.275}As$	8.5 nm	
$In_{0.47}Ga_{0.255}Al_{0.275}As$	40 nm	UID
$In_{0.47}Ga_{0.255}Al_{0.275}As$	160 nm	$Si = 5 \times 10^{17}$

InP:Fe

Figure 2-11: Layer structures for strained MQWs

in QWs depend greatly on the details of QW structure such as well composition and thickness, and such dependence needs to be thoroughly understood for any practical applications of excitons. In this section, we investigate excitonic transitions in compressively strained InGaAs MQWs on InP by transmission[1] and PL measurements. Specifically, quantitative exciton parameters such as transition energies, exciton binding energies and radii are estimated from transmission measurements. Comparisons are made between strained and lattice-matched QWs. From PL measurements, luminescence characteristics are qualitatively analyzed as a function of well thickness and temperature. These results have been reported in Reference [28] and [29].

2.4.1 Experiments

Three strained MQW samples are investigated that have four strained QWs and grown by MBE under the same growth condition on the same day. As can be seen in Figure 2-11, the samples have the identical p-i-n structure except for the different

---

[1]The transmission measurements and data analyses were performed by Yuzo Hirayama, a visiting scientist from Toshiba, Japan.

well thicknesses of 2.5, 5.0 and 7.5 nm for Sample A, B, and C, respectively. P-i-n structure was used because it is the device structure of interest for laser diode applications, and the built-in field in such a structure was expected to enhance the signal levels for PL and photomodulated transmission (PMT) measurements. The layer composition and thickness were accurately determined from DCXRD measurements and simulations in the same manner as discussed in Section 2.3. The well composition is $In_{0.652}Ga_{0.348}As$, corresponding to 0.83 % compressive strain. All the strained layers are believed free of major strain relaxations as evidenced by dislocation-free surface morphology, sharp satellite peaks observed in DCRXD measurements, and narrow and strong low-temperature PL peaks.

Transmission measurements were performed at room temperature (RT) utilizing a tungsten lamp, a 0.275 m single-path monochrometer, a PbS detector, and a lock-in amplifier. Since InP substrates are transparent to the wavelength of interest, a simple, normal incidence transmission geometry was used. The results from the measurement were corrected for any extrinsic effects by subtracting the background signals obtained in the same measurement configuration without a sample. To enhance the signal-to-noise ratio for Sample A and B, two pieces of wafers are stacked together for the measurement, enhancing the effective total well thickness. PMT technique was also performed in which the transmission modulation created by the chopped external laser excitation produces signals that are derivative of transmission spectra. Details of these transmission and PMT measurements can be found elsewhere [30]. For PL measurements, an Ar laser, a 0.5 m single-path monochrometer, a PbS detector, and a lock-in amplifier were used. The sample temperature was varied from 10 K to RT in a cryostat with a He refrigerator and a heater. The estimated laser excitation level is roughly 1 W/cm^2. Schematic drawings of these three measurement set-ups are shown in Figure 2-12.

2.4.2 Results and Discussions

Figure 2-13 shows RT absorption spectra of three samples. Absorption spectra were converted from the transmission data using the relation between transmittivity T and

(a) Transmission Measurement
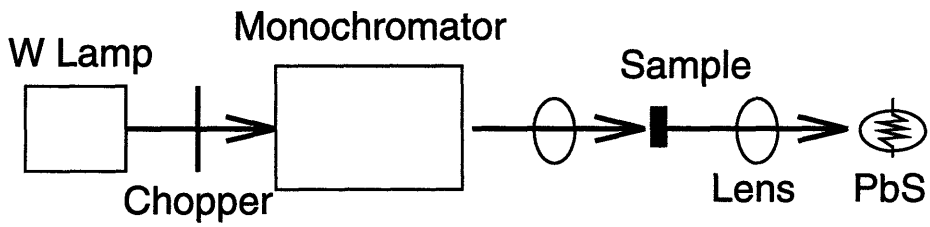
(b) Photo-Modulated Transmission Measurement
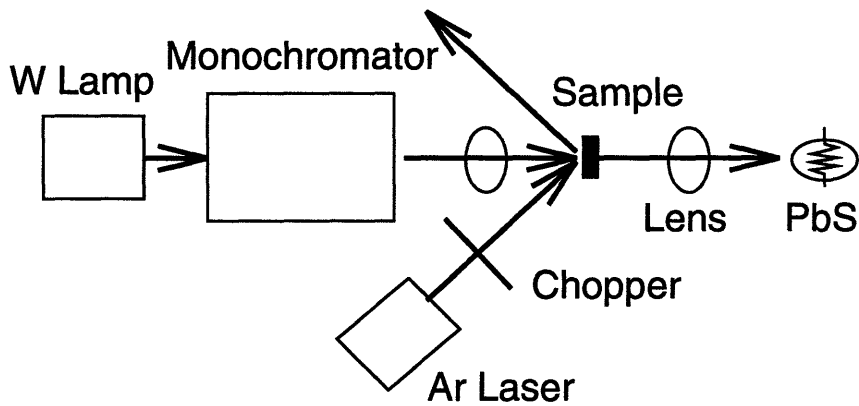
(c) Photoluminescence Measurement
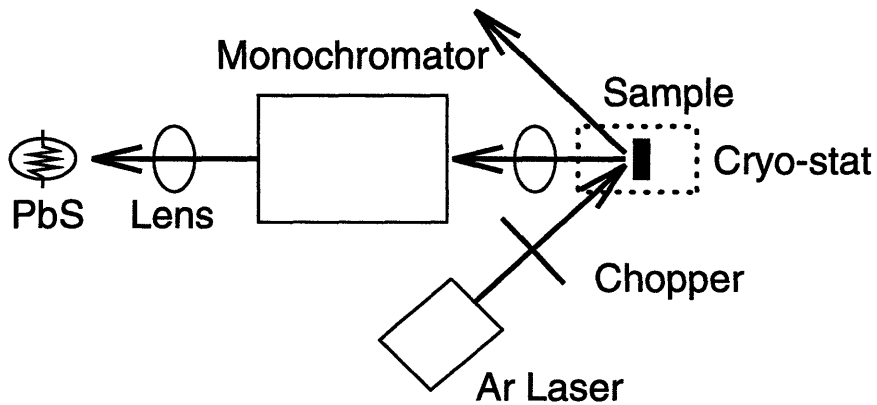
Figure 2-12: Schematic drawings for transmission (a), photo-modulated transmission (b), and photoluminescence (c) measurement set-ups.
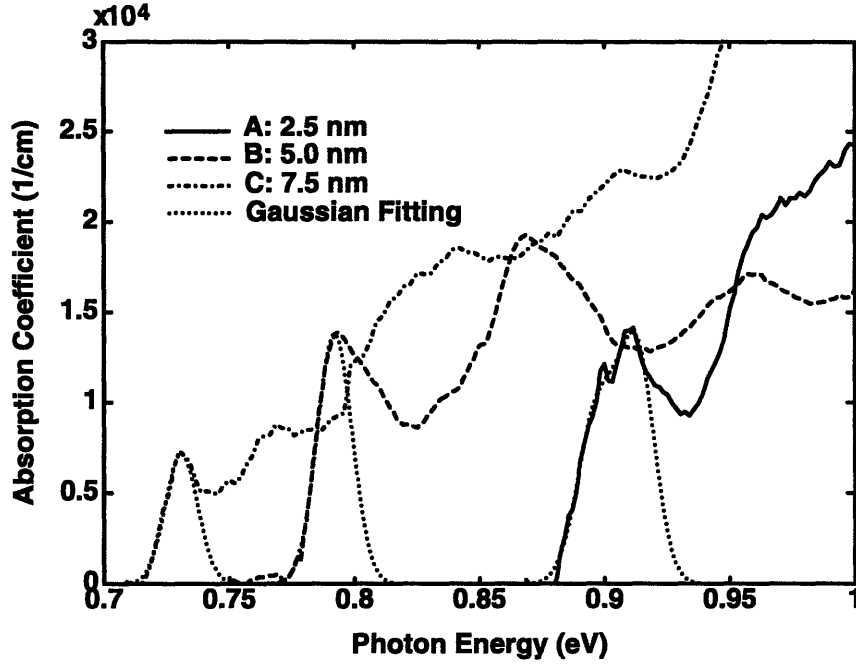
Figure 2-13: Absorption spectra of three strained MQW samples

absorption coefficient α, given as

$$T = (1 - R)^2 \frac{\exp(-\alpha d)}{(1 - R^2) \exp(-2\alpha d)} \tag{2.6}$$

where R is the reflection coefficient, which was assumed to be constant over the wavelength of interest, and d is the total QW thickness. Clear excitonic transitions are observed for e1-hh1 (heavy-hole ground state to electron group state) transitions in all three samples. Sample A is observed to have double peaks at the absorption edge both in transmission and PMT measurements. This is believed due to vertical (different wells) or lateral (different regions) nonuniformity in quantum confinement energies caused by a monolayer fluctuation in well thickness. Since wells are very thin in Sample A, a small fluctuation in well thickness results in a considerable fluctuation in the confinement energy. The separation between two peaks agree well with the calculated value for the confinement energy difference in wells whose thicknesses differ by a monolayer. Figure 2-14 shows PMT and absorption spectra for Sample C with assignments for observed peaks. Five transitions including parity-forbidden e1-hh2 and e2-hh1 transitions are observed. Transition energies were determined based on PMT
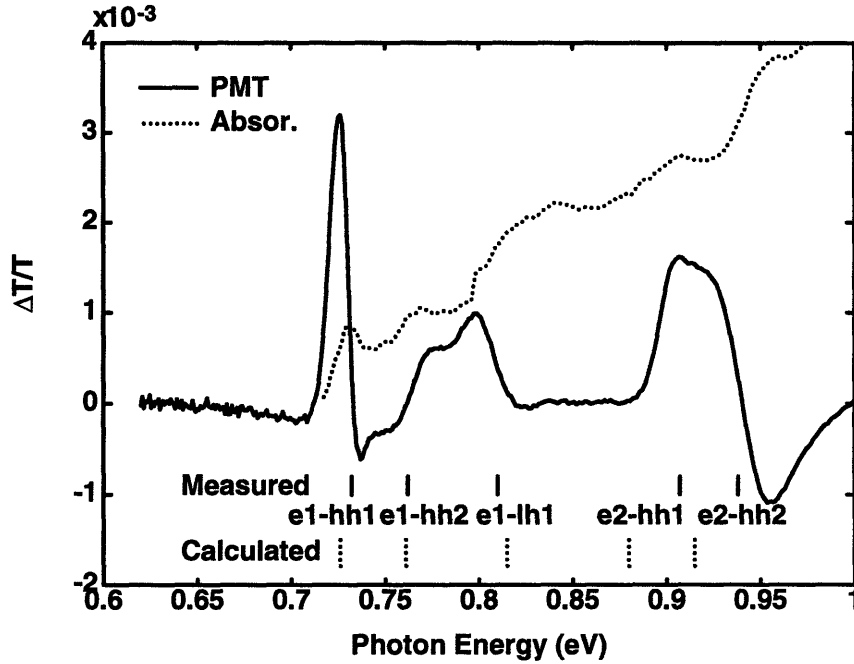
Figure 2-14: PMT and absorption spectra for Sample C.

measurements, which, due to their derivative-like signals, can be more accurate [31]. Transition energies were also calculated by solving the energy levels of electrons and holes in finite-barrier QWs. The values of band offsets between wells and barriers were determined from the model solid theory [32]. For simplicity, the bulk electron and hole effective mass values with energy-dependent nonparabolicity correction for electrons were used. Corrections due to the strain or the built-in electric field were not considered. Even with this relatively simple model, the calculated values agree well with the experimentally determined values for the ground state transitions, but the agreement is not as good for the excited states. This is probably due to uncertainties in the values of effective masses and/or band-offsets that were used for the calculations. From the separations of e1-hh1 and e1-lh1 peaks (for Sample A with double peaks, the more dominant peak at the higher energy was taken as the e1-hh1 peak for this estimation), the values of heavy and light hole splitting are estimated to be 75 meV, 78 meV and 79 meV for Sample A, B and C, respectively. Compared to these, 7.2-nm-wide lattice-matched InGaAs/InAlAs multiple QWs characterized in the same manner have the splitting of only 39 meV.

Sample	L_z (nm)	S (eV/cm)	E_b (meV)	λ_{ex} (nm)	μ (m_o)
A	2.5	406	7.8	13.1	0.038
B	5.0	240	7.3	13.8	0.038
C	7.5	116	5.8	17.2	0.031
LM QW	7.2	213	8.0	12.2	0.046

Table 2.1: Estimated exciton parameters in strained MQWs

To estimate the exciton parameters, integrated intensities S of excitonic absorption are first estimated from the areas of Gaussian curves fitted to the lower energy sides of e1-hh1 transitions in the absorption spectra as shown in Figure 2-13. Two separate Gaussian curves are used for Sample A. From the expression for S as given in Reference [33], the value of exciton radius λ_{ex} can be determined. Furthermore, solving in a variational manner the equation for exciton binding energy E_b as a function of λ_{ex} and and reduced in-plane effective mass μ, E_b and μ can be estimated [34]. Details of these estimations can be found in Reference [30]. Table 2.1 lists all the estimated parameters for three strained MQW samples as well as for a reference lattice-matched InGaAs/InAlAs MQW sample characterized in the same manner. It is clear that e1-hh1 excitons in compressively strained QWs have lower binding energies and larger radii than those in lattice-matched QWs. This is due to the reduction in the value of reduced in-plane effective mass caused by the compositional change as well as compressive strain. In fact, this reduction in the reduced in-plane effective mass value, along with the larger splitting between heavy and light hole quantized levels as observed above, is what makes compressive strained QW lasers better than unstrained QW lasers. From Table 2.1 it can be also seen that with the same well composition, the narrower QWs have excitons of larger exciton binding energies and smaller radii, as expected from the tighter exciton confinement in narrower QWs.

While RT absorption is dominated by the free excitonic effect, this is not the case for RT PL. Figure 2-15 shows PL and absorption spectra of three samples together. The amplitude of each absorption and PL spectra is normalized to so that comparisons between them can be made easily. For Sample B and C, the PL peaks are at slightly higher energies than absorption peaks. The separations between PL and ab-
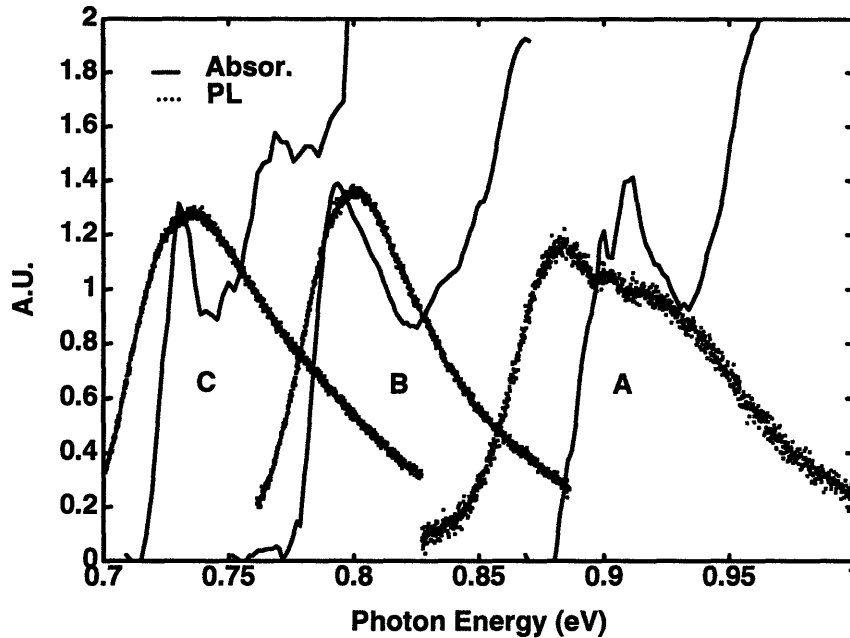
Figure 2-15: Absorption vs. PL for three strained MQW samples

sorption peaks (about 7 meV for B, and 5 meV for C) are close to the exciton binding energies estimated in Table 2.1. This indicates that RT luminescence is dominated by band-to-band rather than excitonic recombination. More quantitative analysis will require a detailed lineshape fitting that includes both excitonic and band-to-band recombinations [35]. In the case of Sample A, a careful examination reveals there are three peaks, two of which have slightly higher energies than corresponding absorption peaks. Those two peaks with corresponding absorption peaks are believed to be related to band-to-band recombination. The nature of the lowest energy PL peak is presently not clear, although one possibility is that it is related to bound excitons due to defects. It shows up only in PL and not in absorption probably because PL favors transitions with the lowest transition energy and/or shortest lifetime.

PL measurements were done at various temperatures ranging from 10 K to RT so that luminescence characteristics can be investigated as a function of temperature. Figure 2-16 shows the PL peak positions for different cryostat temperatures. The data for Sample B and C are vertically shifted for an easier comparison. Interestingly, all three samples show different temperature dependence. For Sample C, two clearly

45
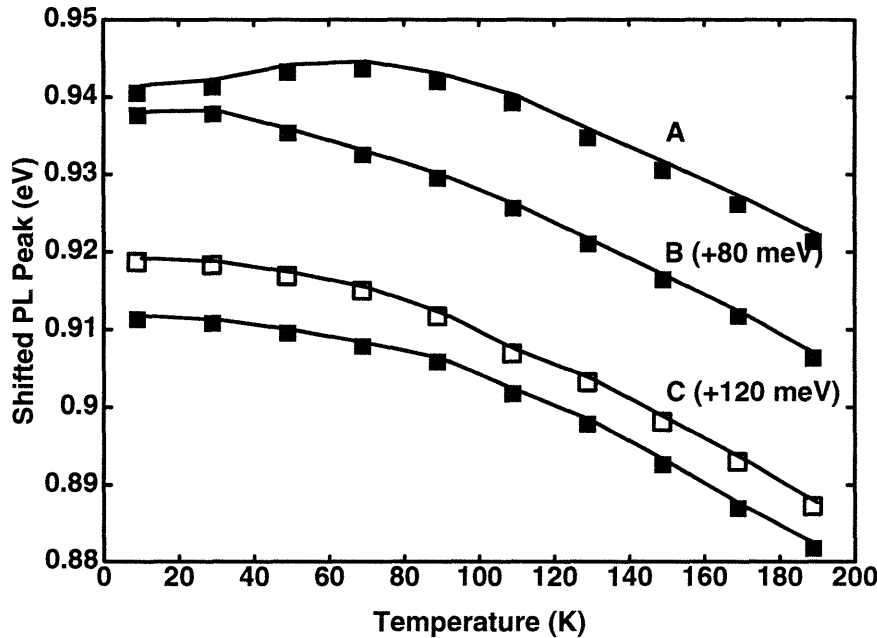
Figure 2-16: PL peak positions at different temperature

resolvable peaks are observed up to 190 K. PL spectra for Sample C at a few selected temperatures are shown in Figure 2-17 for a comparison. At low temperature, the low-energy peak is dominant but as temperature increases the high-energy peak becomes more dominant, and at around 210 K the lower energy peak gets completely buried in the high-energy peak. The separation between these two peaks as estimated by least square lineshape fitting with two Gaussian curves is about 7.5 meV at low temperature but decreases to 5.5 meV at around 100 K. These observations can be explained by assigning the high-energy peak to band-to-band and the lower-energy peak to excitonic transition. The separation of 5.5 meV is comparable to the exciton binding energy estimated earlier. At low temperature, the binding energy is larger probably because excitons are bound by impurities or interface defects [36]. Band-to-band recombination can be observed even at very low temperature for Sample C probably because the exciton binding energy of Sample C is very small. Similar observation has been made in GaAs QWs [37]. For Sample B, only one clearly resolvable peak is observed throughout the entire temperature range. It should be noted, however, that at around 100 K a shoulder develops in the higher energy side of the dominant peak
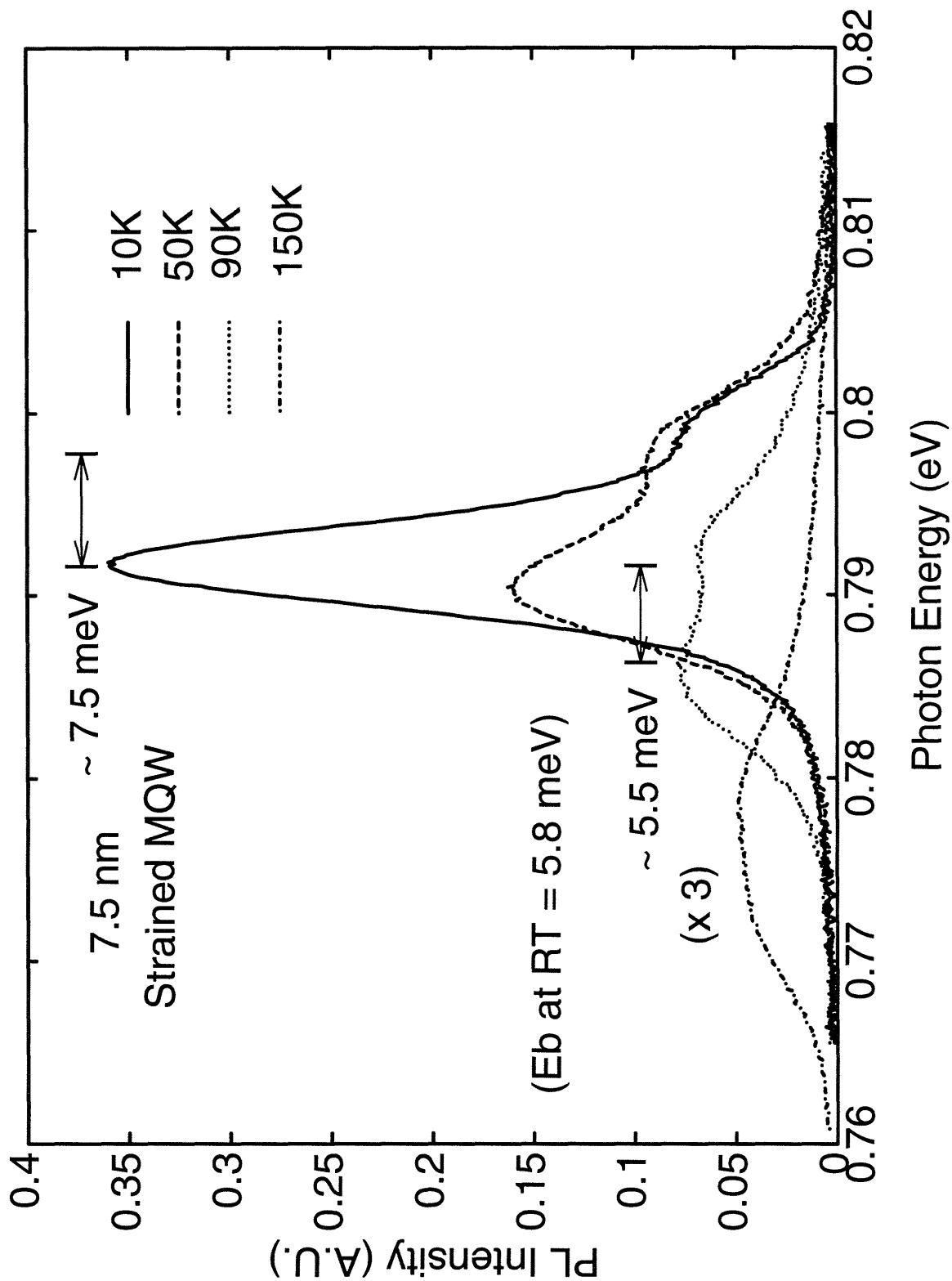
Figure 2-17: PL spectra at different temperature for a 7.5-nm-wide strained MQW sample, Sample C. Two distinct peaks are observable from all of them. The peak separation is about 7.5 meV at low temperature but decreases to about 5.5 meV at high temperature.

that eventually becomes the dominant peak above 200 K. Again, this is interpreted as the shifting from excitonic transition at low temperature to band-to-band transition at high temperature for the dominant recombination process. Sample A shows pronounced lowering of the peak energy at low temperature presumably due to the increase in exciton binding energy due to bound excitons. The increase is estimated to be about 8 meV by projecting the PL peak position at low temperature from the high-temperature values with the calculated bandgap dependence on temperature. Compared to 2 meV estimated for Sample C, this larger increase is believed due to the smaller well thickness in Sample A. Although the exact nature of these bound excitons will require more detailed studies, this clearly demonstrates that binding energies of bound excitons depend on the well thickness. From the above observations, the dominant recombination process for the samples under present study is determined to be due to bound excitons for temperature below 100 K, and, at least for Sample B and C, free excitons between 100 to 200 K and band-to-band transitions above 200 K.

Chapter 3

Design, Fabrication, and Characterization of InGaAlAs Strained MQW Laser Didoes

Once MBE growth and relevant materials characterization techniques are established, as discussed in the previous chapter, the next steps are to design the optimal laser layer structure, epitaxially grow the structure, process the resulting material into complete devices, and characterize the resulting laser devices. These are the topics discussed in this chapter. For the optimal device structure, compressively strained MQWs are utilized, as they are the basis of the current state-of-the-art laser diodes. A brief description of the advantages of compressively strained QWs for laser applications is given in Section 3.1. Although the decision for using compressively strained QWs can be easily made, there still remain a number of issues that require careful considerations before high performance lasers can be achieved. These issues, such as determinations of the exact QW and SCH structures , are discussed in Sections 3.2. Laser structures resulting from these considerations were grown by MBE, and broad-area and ridge-waveguide lasers were fabricated. Their device characteristics as well as the processing steps are discussed in Section 3.3.

3.1 Why Strained QWs?

It is now well known that strained QWs greatly enhance laser device performance. For example, lasers with the lowest threshold current density [38] and the highest modulation speed [39] are all based on compressively strained QWs (InGaAs QWs on GaAs). Since our device structures will utilize strained QWs too, the advantages of strained QWs for laser applications are briefly discussed. This is done in a qualitative manner emphasizing only the essential elements and leaving more detailed descriptions to other references [40]. The discussion is limited to the laser threshold current density since this is the most important parameter among many laser parameters enhanced by strained QWs, and our efforts in this study are mainly focused on obtaining InGaAlAs lasers with as low threshold current densities as possible. Although a recent report indicates that tensile strained QW lasers have device performance as good as compressively strained QW lasers [41], only compressively strained QWs are discussed here since the advantage of tensile strain QW lasers are less well understood and the present study considers only compressively strained QWs.

The first step toward understanding why strained QW lasers do better is understanding why QW lasers, without even any built-in strain, do better than bulk lasers. QW lasers usually have about one tenth of the threshold current density required for bulk lasers and it is of great interest to identify what gives such a reduction. In order to make this identification, we start with the expression for the gain and investigate what different contributions are made by QWs and bulk to the gain. For a fair comparison, we assume for the time being that the active region thickness is the same for QW and bulk lasers.

The gain $g(E)$ for a photon of energy E with the k-selection rule can be expressed as

$$g(E) \propto M^2 \times \rho_{\text{red}}(E) \times [f_c(E_c) + f_v(E_v) - 1] \qquad (3.1)$$

where, with E_c (E_v) the electron (hole) energy measured into the conduction (valence) band from the band edge and E_g the band-gap, $E = E_c + E_v + E_g$; M is the matrix element for the optical transition; ρ_{red} is the reduced (or joint) density of states for

electrons and holes; f_c (f_v) is the electron (hole) quasi-Fermi factor, given as

$$f_{c(v)}(E_{c(v)}) = \frac{1}{\exp\left[(E_{c(v)} - E_{fc(fv)})/k_B T\right] + 1} \qquad (3.2)$$

with $E_{fc(fv)}$ being the electron (hole) quasi-Fermi energy measured into the conduction (valence) band from the band edge.

The matrix element M is related to the amount of perturbation caused by the incident electric field to the electron and hole wave-functions. Since the basic Bloch functions are of the same nature for both QWs and bulk, the only difference in M between QWs and bulk lies in their polarization dependence [42]. If we are only concerned with the TE gain as lasing usually occurs with the TE polarization, QWs have slightly larger matrix elements than bulk at the zone center since the zone center optical transitions in QWs are dominated by heavy holes – because light holes shift more away from the bulk band edge – which allow only the TE-active transitions and do not "waste" any transitions into the TM polarization. This advantage for QWs, however, is easily lost as injected carriers require optical transitions away from the zone center where there is a significant amount of heavy- and light-hole coupling. Consequently, it is fair to say that there is no major difference between QW and bulk matrix elements.

If we assume the electron and hole effective masses in QWs are not much different from their bulk values, QWs have smaller $\rho_{red}(E)$ than bulk since step-like $\rho_{red}(E)$ in QWs is always smaller than parabolic $\rho_{red}(E)$ in bulk. This slight disadvantage for QWs, however, is compensated by the last factor $[f_c(E_c) + f_v(E_v) - 1]$ which can be much larger for QWs than bulk with the same amount of injected carriers. To explain why this is the case, we now show that less injected carriers are needed in QWs than in bulk to reach the same values for the quasi-Fermi factors at the gain peaks. This is schematically demonstrated by Figure 3-1 in which the amounts of electrons required to reach certain values of f_c at the gain peak are graphically represented. Here, only electrons in the conduction band are considered for simplicity but the same argument should apply to holes in the valence band. When the pumping level is low so that
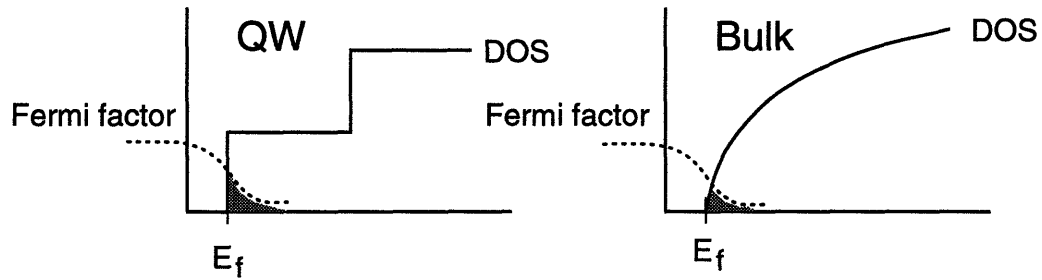
(a) Low Pumping: $N_{QW} > N_{Bulk}$
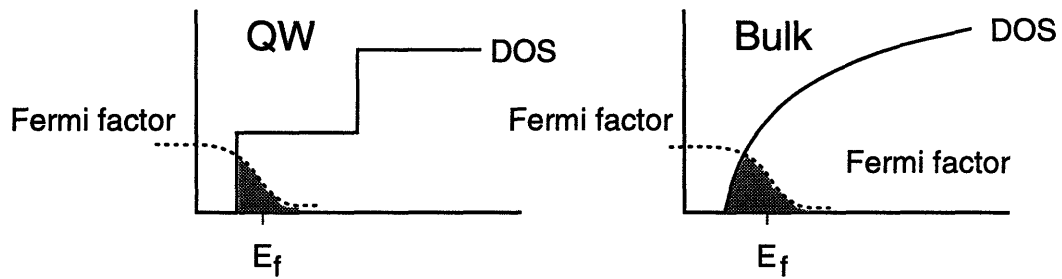
(b) High Pumping: $N_{QW} < N_{Bulk}$

Figure 3-1: A schematic demonstration of different amounts of injected carriers for QWs and bulk. The injected carrier density is determined by the product of the density of states and the Fermi factor, and is represented by the area of the shaded region. When the pumping level is low $N_{QW} > N_{Bulk}$, but when the pumping level is high $N_{QW} < N_{Bulk}$.
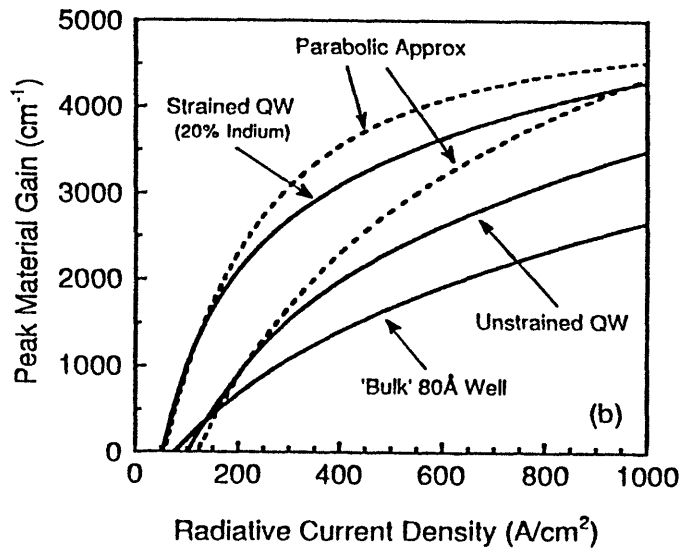
Figure 3-2: Calculated gain vs. radiative current density for bulk, unstrained QW and strained QW obtained from Reference [43]. Dotted curves are from calculations based on the parabolic approximation for the valence band, and solid curves on the Luttinger-Kohn model for the valence band. The solid curves are used for comparisons made in the text.

E_{fc} is just above the band edge, there are less injected electrons in bulk than in QWs for a given f_c at the gain peak (Figure 3-1 (a)). This is simply because bulk has a much smaller density of states around the band edge than QWs. However, when the pumping level is large so that the gain is sufficient enough to compensate mirror as well as internal losses as is required for lasing, less electrons are required for QWs than for bulk (Figure 3-1 (b)). This is because in QWs the gain peak is right at the band edge due to their step-like density of states whereas in bulk the gain peak is way into the band, thus "wasting" all the injected carriers populated near the band edge.

This difference is quantitatively illustrated by Figure 3-2 in which the gains for bulk, unstrained QW, and strained QW are calculated at different injection current densities [43]. Here it is assumed that all the injected carriers recombine radiatively.

As can be seen from the figure, the bulk lasers become transparent (zero gain) with a smaller injected current density but for the usual amount of the material gain needed for lasing (about 2000 cm^{-1} or so), QW lasers require about 70 % as much current injection as bulk lasers. This reduction is due to the more efficient use of injected carriers in QWs with their step-like density of states.

Having identified the cause for about 30 % reduction, we now need to look for the rest of the factor-of-ten reduction for QW J_{th} from bulk J_{th}. The rest is due to the fact that usual QW lasers have much thinner active layers than bulk lasers, and thus have a smaller volume to pump. The laser threshold current density can be expressed as

$$J_{th} = q\, d \int R(n_{th}, E)\, dE, \tag{3.3}$$

where q is the electron charge, d is the total active layer thickness, and $R(n_{th}, E)$ is the radiative recombination rate with the transition energy E and the carrier density n_{th} which provides sufficient gain to satisfy the lasing condition. Here again we assume that all injected carriers recombine radiatively. This expression simply means that the current density in the amount of J_{th} needs to be supplied in order to refurbish electrons and holes that keep disappearing due to recombination and to maintain the required carrier density of n_{th}. QW lasers have about factor of ten thinner active layers than bulk lasers and along with about 30 % reduction identified before, it may seem that QW lasers should have larger than factor-of-ten reduction in J_{th} from bulk lasers. In reality, this does not happen since QW lasers with their thinner active layers also have the smaller confinement factor than bulk. This necessitates QW lasers to have higher gain, which in turn requires higher n_{th}, causing larger $R(n_{th}, E)$ and larger J_{th}. Knowing that QW lasers have about one tenth of J_{th} for bulk lasers, it is easy to see that the scaling effect reduces QW laser J_{th} by about factor of seven. It is interesting to note that this is much larger than the reduction in J_{th} due to the quantum confinement effect which has been estimated to be about factor of one and half. In other words, QW lasers benefit more from simple scaling than from quantum

confinement[1]. The same observation is made in Reference [44].

Having shown that QW lasers have lower J_{th} than bulk lasers, we now need to investigate why strained (compressively) QW lasers have even lower J_{th} than unstrained QW lasers. The major difference between these two lies in the valence band structure. With compressive strain, the valence band structure changes such that heavy hole in-plane effective masses become much lighter and heavy- and light-hole bands split significantly (the heavy hole band above the light hole band). These changes affect the three major elements for the gain expression given in Eq. 3.1 in the following manner. First, the matrix element becomes higher for strained QWs since with the heavy- and light-hole splitting, most optical transition even away from the zone center is dominated by heavy holes with their TE-active only transitions. Second, the reduced density of states for strained QWs is lower than that of unstrained QWs since strained QWs have much smaller in-plane hole effective masses. Third, most importantly, the quasi-Fermi factors are much higher with a given amount of injected carriers for strained QWs than unstrained QWs.

The primary reason for the third factor is that the hole in-plane masses are much smaller in strained QWs than unstrained QWs. In order to explain how lighter hole effective masses result in lower J_{th} for strained QW lasers, we first obtain from Eq. 3.1 the condition for population inversion, or reaching zero gain, as

$$f_c(E_c) + f_v(E_c) = 1. \tag{3.4}$$

Substituting expressions for $f_c(E_c)$ and $f_v(E_v)$ as given in Eq. 3.2 into Eq. 3.4, it can be easily shown that the above population inversion requirement is equivalent to

$$E_{fc} + E_{fv} + E_g = E. \tag{3.5}$$

---

[1]It should be noted that another important laser performance parameter, differential gain – dg/dn, the incremental change in gain with respect to the injected carrier density – is much higher for QW than bulk lasers because the step-like density of states of QWs gives much more carriers populated right at the band edges than the parabolic density of states of bulk. This is a direct result of quantum confinement.

This is the famous Bernard-Duraffourg condition for population inversion in semiconductor [45]. Since the transition with the minimum E is between electrons and holes right at the respective band edges, the minimum required separation between the electron and hole quasi-Fermi energies to reach population inversion is E_g. As carriers are injected into an unstrained QW in which holes are much heavier – thus larger density of states – than electrons, both E_{fc} and E_{fv} shift but E_{fc} has to shift more in order to maintain charge neutrality. This forces E_{fc} beyond the conduction band edge when the Bernard-Duraffourg condition is satisfied, as shown in Figure 3-3 (a). It is easy to see from Figure 3-3 that the minimum number of carriers are required when E_{fv} can move as much as E_{fc}, or the density of states for holes is the same as that of electrons, since then the Bernard-Duraffourg condition is achieved with E_{fc} and E_{fv} just reaching the respective band edges. In addition, the required carrier density will be smaller if both electron and hole densities of states are smaller since there simply will be less carriers populated when population inversion is reached, as shown in Figure 3-3 (c). These are precisely what strained QWs provide: Compressive strained QWs are made of lower band-gap materials which provide lighter electron and hole effective masses, and with the built-in strain the heavy hole in-plane mass becomes much lighter than its bulk value, thus providing a more symmetric density of states compared to that of electrons. This advantage results in about factor-of-two reduction in J_{th} for strained QW lasers from J_{th} for unstrained QW lasers given the usual amount of threshold gain of about $2000 \, \mathrm{cm}^{-1}$, as can be seen from Figure 3-2.

3.2 Design of Strained MQW Lasers

3.2.1 Strained QW Design

The first question in designing strained QW lasers is how to determine QW composition and thickness. Although it is desirable to have as much strain as possible, strain should not cause dislocations due to strain relaxation and QWs with a given amount of strain should provide the target lasing wavelength. The lasing wavelength

(a) Unstrained QW
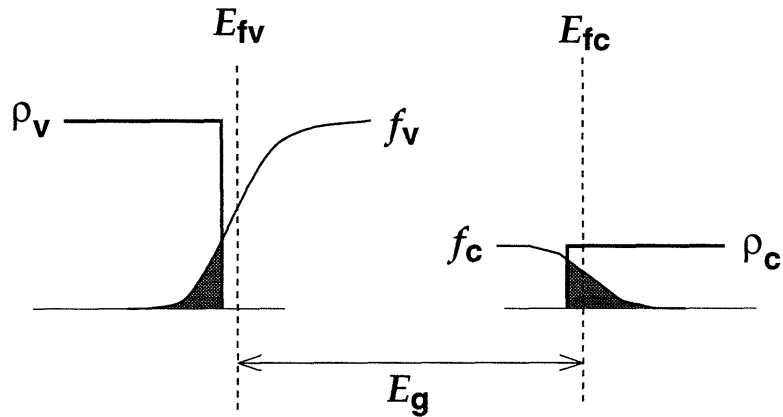
(b) Strained QW
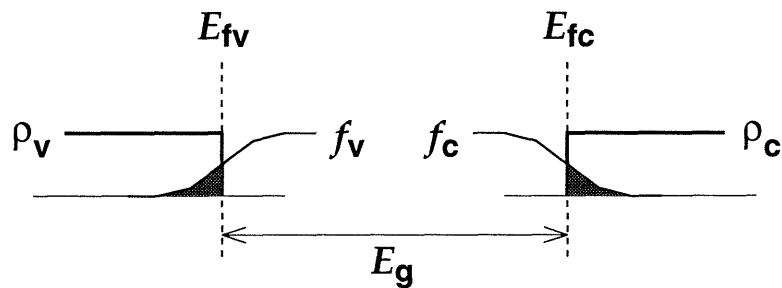
(c) Strained QW with smaller ρ
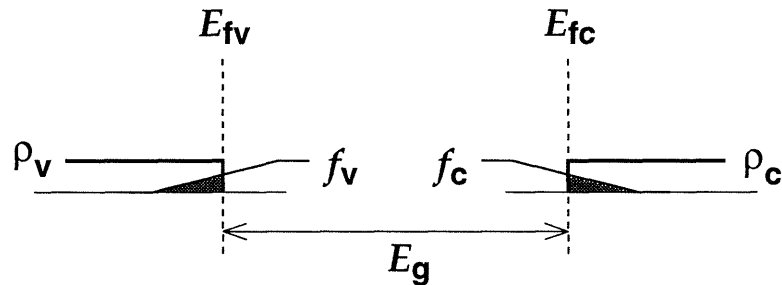
Figure 3-3: QWs at population inversion with three different types of electron and hole densities of states: (a) asymmetric, (b) symmetric, and (c) symmetric and smaller values. Population inversion requires the separation of E_{fc} and E_{fv} to be as much as E_g for all three cases. But depending on the density of states the required amount of injected carriers, as shown by the shaded area, can be quite different. More symmetric density of states is beneficial since it more efficiently utilizes injected carriers to shift both electron and hole quasi-Fermi energies, and smaller density of states is beneficial since there simply are fewer injected carriers when population inversion is reached. Both of these advantages are obtained with compressively strained QWs.
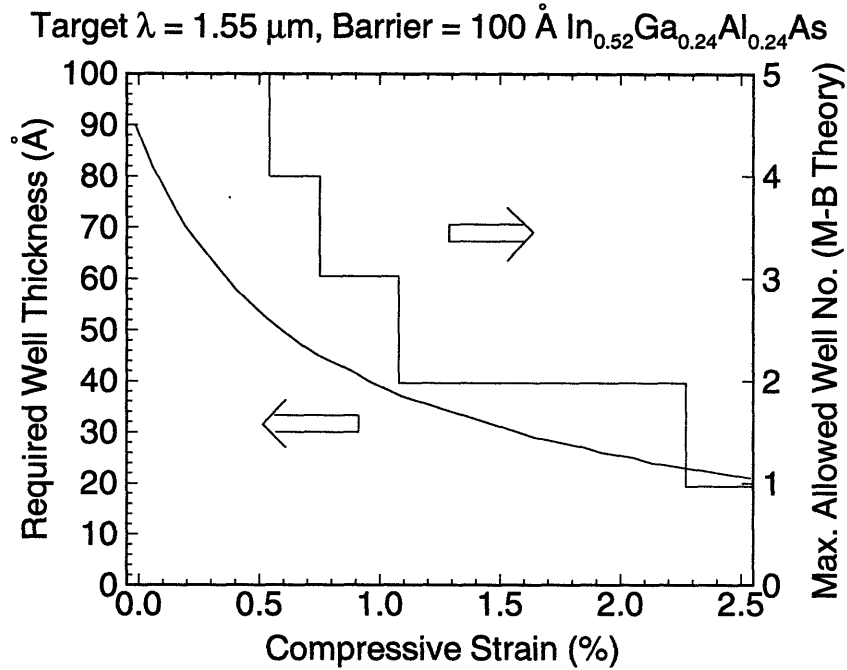
Figure 3-4: Calculated strained QW thickness giving 1.55 μm lasing wavelength for a given amount of compressive strain, and the maximum number of unrelaxed QWs with given strain and well thickness for 1.55 μm. The barrier structure is fixed with 100-Å-thick $In_{0.52}Ga_{0.24}Al_{0.24}As$.

will depend on the ground state electron-hole transition energy in a QW, which is determined by well composition, thickness, and the amount of strain incorporated. A strained layer will relax if its thickness goes beyond a certain critical value at which it is energetically favorable to form dislocations rather than to sustain strain. In order to obtain strained QW well structures that satisfy above two requirements, calculations were performed in which QW thickness required for the lasing wavelength of 1.55 μm was determined for different amounts of compressive strain. This is shown in Figure 3-4. The lasing wavelength was determined for well composition necessary for the given strain by solving quantized energy levels for electrons and holes with finite barriers. The barrier material was fixed at 100 Å $In_{0.52}Ga_{0.24}Al_{0.24}As$ lattice-matched to InP. The barrier heights for electrons and holes were obtained from band offset values calculated with the model solid theory [32]. Bulk values were used for electron and hole effective masses without corrections due to band-mixing or strain. As can be seen from the figure, larger strain requires smaller QW thickness. Since

multiple, rather than single, QWs are anticipated for actual device applications and these strained MQWs may face the strain relaxation problem, the maximum number of pseudomorphic QWs for given strain and well thickness was also calculated. For this calculation, Mathews and Blakeslee's (M-B) model for the critical layer thickness [46] was used. Since the original M-B model is derived for a single layer of a strained film and is not suitable for a MQW structure as in the present case, an approximation was made in the following manner. For a given MQW structure, the weighed (with respect to thickness) average lattice constant of wells and barriers was determined first and the critical layer thickness for this lattice constant was calculated according to the M-B model. If the total well and barrier thickness is larger than the calculated critical layer thickness, then the MQW structure under consideration was determined to be relaxed. The step-like line in Figure 3-4 shows the maximum number of unrelaxed QWs for a given amount of strain with well thickness determined for $1.55\,\mu m$ lasing. It is shown in the figure that 40-Å-thick, one percent compressively strained QW gives $1.55\,\mu m$ lasing wavelength, and as many as three QWs of such a composition can be grown without relaxation. This strained QW structure, whose composition corresponds to $In_{0.68}Ga_{0.32}As$, was chosen for our target structure for the laser application.

3.2.2 Verification of Strained QW Design

The above design needs to be verified, however, since the M-B model is a thermodynamic model and, strictly speaking, does not apply to films grown under the MBE growth condition which is far from the thermodynamic equilibrium. Although there exists a kinetic model that may be more accurate for MBE-grown layers [47, 48], this model involves fitting parameters that can not be easily obtained and is not much of help in practice. Consequently, an experimental verification is needed for the above strained QW structure that it is indeed free of dislocations when grown under the growth condition to be employed for actual device applications. Further, with reports in the literature that the M-B critical layer thickness is a conservative estimate [49], it is of strong interest for the device application to find out how many QWs with the
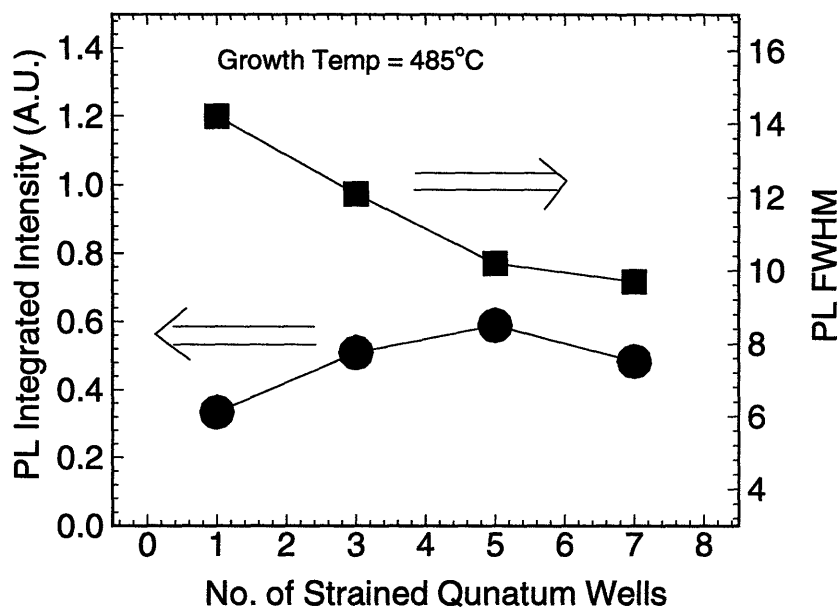
Figure 3-5: PL integrated intensities and FWHM's for strained QW samples with different total well numbers.

above composition can be grown without significant degradation in material quality. For this purpose, MBE samples of strained MQWs were grown that have different numbers of wells: 1, 3, 5, and 7. The wells were 40-Å-thick $In_{0.68}Ga_{0.32}As$, as determined to be the target structure, and the barriers were 100-Å-thick lattice-matched InAlAs. Wells and barriers were clad by 2000-Å-thick lattice-matched InAlAs layers. Care was taken to grow these samples under identical growth conditions on the same day. The resulting samples were characterized by 10 K PL. Figure 3-5 shows the PL integrated intensities and FWHM's of these samples as a function of the total well number. If there is no strain relaxation and the wells are of good quality, then the integrated intensity is expected to increase with the increasing well number since more wells provide more volumes for luminescence. On the other hand, the linewidth is expected to decrease with the increasing well number since, with the identical amount of excitation for each sample, there should be fewer collected carriers per well for samples with more wells and, therefore, less band-filling and smaller linewidth[2]. In

---

[2]This assumes our PL linewidth is limited by the band-filling effect, which is justified by the observation that PL linewidth of the single QW sample decreases with less excitation power.
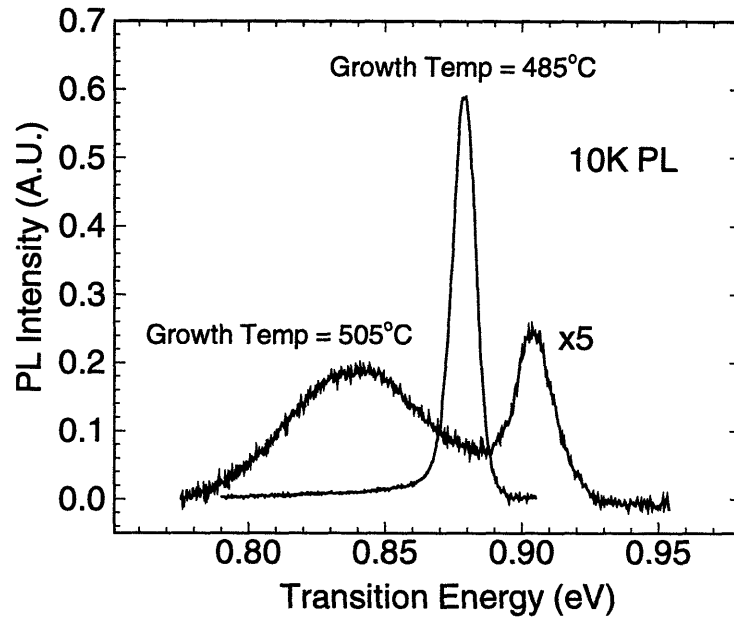
Figure 3-6: PL spectra of strained QWs grown at different temperature.

strain-relaxed QWs, however, it is well known that dislocations reduce PL intensity and broaden linewidth [50]. As can be seen from the figure, the PL integrated intensity increases initially but decreases for the seven-well sample, and the rate of FWHM decrease changes also for the seven-well sample. This observation is interpreted that the seven-well sample is suffering from strain relaxation. This sets the upper limit of the number of strained QWs to seven for our target strained QW structure.

In addition to the maximum number of strained QWs, it is also necessary to determine MBE growth condition in which the required strained MQW structure can be grown. This is because strain relaxation in MBE-grown thin films is a kinetic phenomenon and depends on such parameters as growth temperature. In order to determine safe growth temperature with which at least five stained QWs of the desired composition can be grown, two samples with five 40 Å $In_{0.68}Ga_{0.32}As$ QWs were grown at two different temperature settings of around 485 °C (this is one of the samples used in the previous investigation of the maximum number of unrelaxed strained QWs) and 505 °C, and were characterized by 10 K PL. Figure 3-6 shows their remarkably different PL spectra. The sample grown at 505 °C has two peaks: one at higher

energy with smaller FWHM and the other at lower energy with much larger FWHM. The sample grown at 485 °C, however, has only one sharp peak. Since the only difference between these two samples was MBE growth temperature, it is interpreted that growth at 505 °C caused strain relaxation but 485 °C did not. The peak at the lower energy for the sample grown at 505 °C is believed due to luminescence from portions of QWs that have been relaxed, and the higher-energy peak from portions not relaxed. This interpretation also explains the difference in the overall PL intensity between two samples since dislocations due to strain relaxation is known to reduce PL intensity. The observation that the higher-energy peak of the sample grown at 505 °C is at higher energy than the peak of the sample grown at 485 °C is believed due to enhanced loss of indium at high growth temperature. Although PL data alone cannot completely ascertain above interpretations, it is clear that our target strained QW structure should not be grown at too high temperature. Consequently, the active region of most strained QW lasers in the present study were grown around 485 °C. This, along with higher temperature of 525°C for the optimal InAlAs cladding layers determined in the previous chapter, required precise temperature control during the MBE growth of laser devices.

3.2.3 SCH Layer Design

QW lasers utilize SCH layers in order to enhance the optical confinement factor. The optical confinement factor represents the amount of overlap between the field intensity and the gain medium. Since the transverse spread of the field is much larger than quantum well width, the confinement factor is very small if QWs are simply inserted between top and bottom cladding layers. Instead, an additional waveguide core region, called SCH, is placed surrounding QWs, that guides the wave more tightly and, hence, enhances the confinement factor. This is schematically shown in Figure 3-7.

If SCH has a graded index profile, it is called graded-index SCH (GRINSCH). A GRINSCH structure has an advantage over a simple SCH structure in that it prevents "carrier spill" out of the wells and, hence, has higher current injection efficiency [11,

refractive index

VS   or

$$\Gamma \ll \Gamma_{SCH}, \Gamma_{GRINSCH}$$
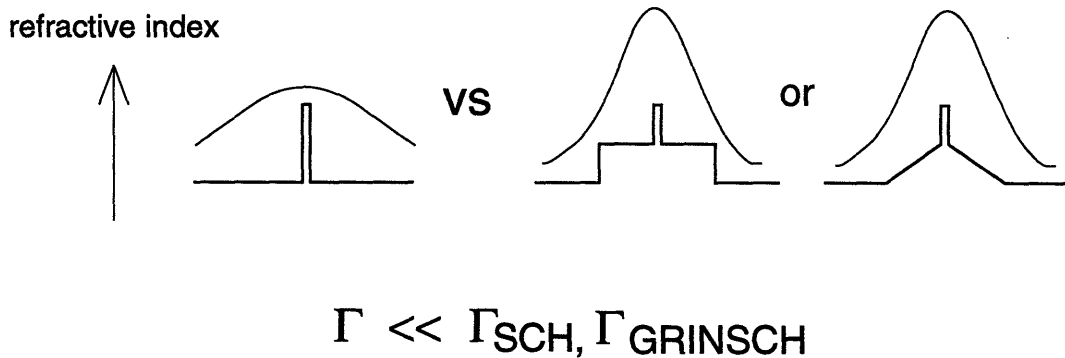
Figure 3-7: Confinement factor enhancement by SCH

51]. Consequently, the GRINSCH structure is used in the present work. Growing continuously graded layers is, in fact, a challenge in itself since Ga and Al fluxes need to be continuously changed while the resulting lattice constant is kept the same so that lattice-matching is maintained. With our MBE machine, such control can be done relatively easily with a computerized growth control capability [52]. As a demonstration of this capability, Figure 3-8 shows the result of an Auger electron depth profile measurement for a linearly graded InGaAlAs sample. It clearly shows that Ga and Al atomic concentrations are nicely graded as intended.

In using the GRINSCH structure, the optimal GRINSCH layer thickness needs to be determined so that the confinement factor can be maximized. Figure 3-9 shows calculated confinement factor dependence on GRINSCH layer thickness, where the GRINSCH layer is linearly graded from cladding material $In_{0.52}Al_{0.48}As$ to barrier $In_{0.52}Ga_{0.24}Al_{0.24}As$. For the calculation, our target strained QW structure determined above – 40-Å-thick $In_{0.68}Ga_{0.32}As$ wells and 100-Å-thick $In_{0.52}Ga_{0.24}Al_{0.24}As$ barriers – were used. Calculations were done for structures with three and six QWs for comparison. For simplicity in calculation, linearly graded regions were approximated by steps of 300-Å-thick homogeneous materials. The confinement factors were determined by solving the multi-layer waveguide problem with the transfer matrix method. As can be seen in the figure, the confinement factor does not depend too strongly on GRINSCH layer thickness; around 2000 Å, the confinement factors reach the maximum values for both three- and six-QW cases. As expected, the sample with

Target Layer Structure

100 nm $In_{0.52}(Ga_{1-x}Al_x)_{0.48}As$
linearly graded from x=1 to 0.5, 0.5 to 1

5 x 9.5 nm InGaAs wells
4 x 8 nm barriers
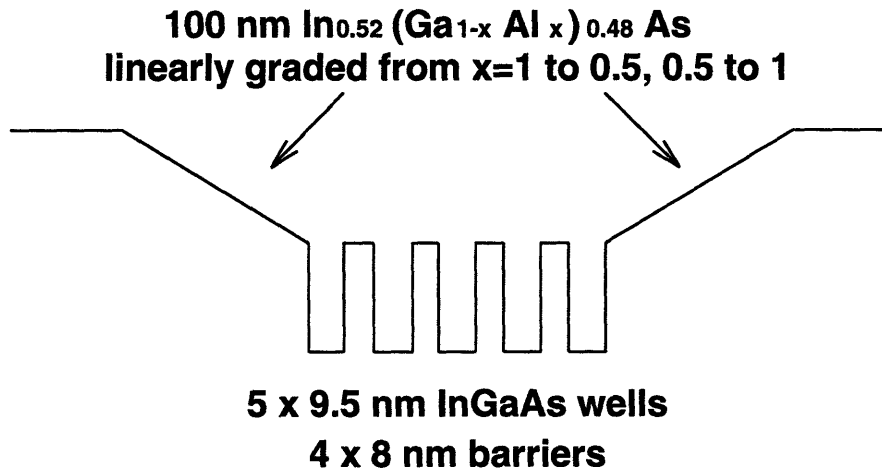
Auger Electron Spectroscopy

Atomic Conc.

— Al
--- Ga

Sputtering Time
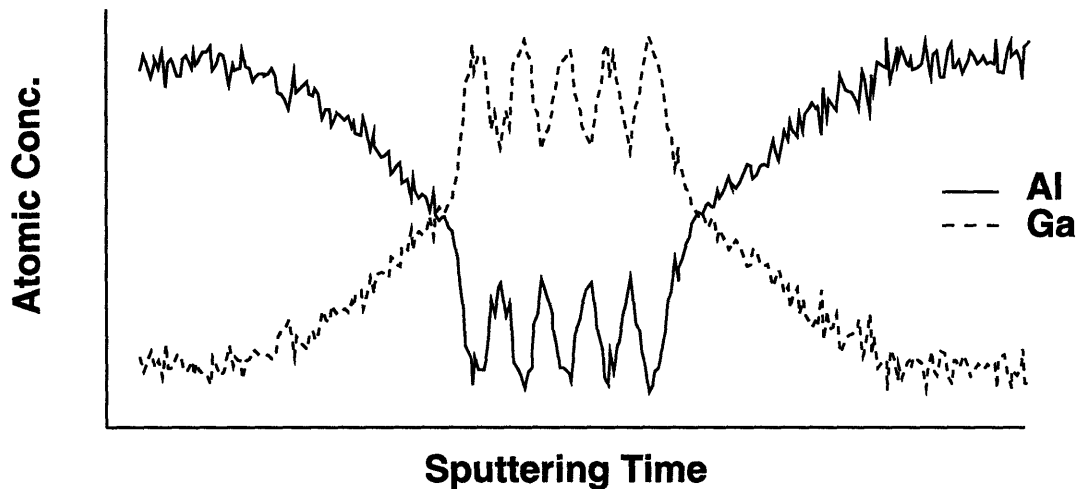
Figure 3-8: Confirmation of a graded InGaAlAs layer structure by Auger electron depth profile measurement. The top figure shows the target layer structure and the bottom the result of an Auger measurement. This measurement was performed at the Surface Analysis Laboratory of MIT Center for Material Science and Engineering with the help of Ms. Elizabeth Shaw.
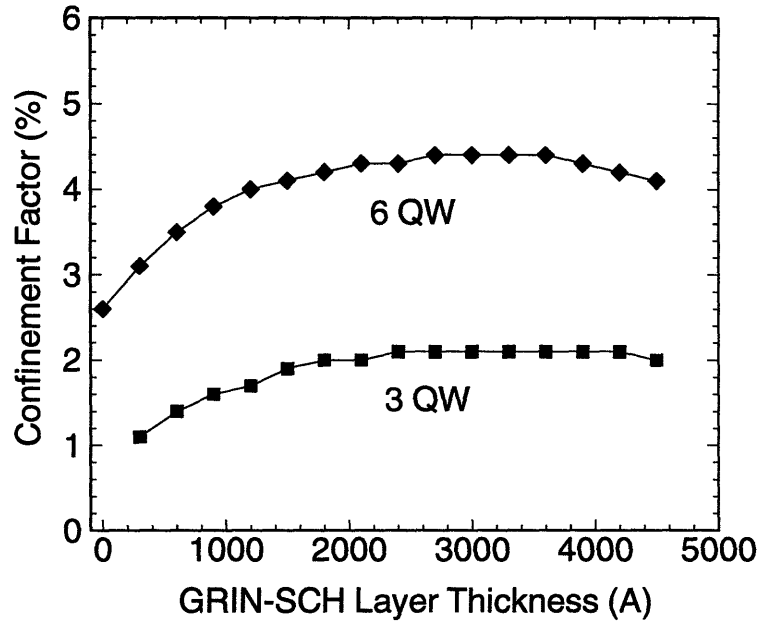
Figure 3-9: Dependence of the optical confinement factor on GRINSCH layer thickness.

six QWs has about factor of two larger confinement factor than the structure with three QWs. Since thickness of SCH layers do not have to be thicker than needed – in fact, for high speed operations, the SCH layers should be as thin as possible to minimize carrier transport time through them [53] – GRINSCH layer thickness was fixed at 2000 Å for our target device structures.

3.3 Device Results

3.3.1 Broad-Area Devices

Actual laser diode samples were grown by MBE with the above determined target layer structure. Figure 3-10 shows one such laser structure. Besides strained QWs, GRINSCH layers, and top and bottom cladding layers, it also has a highly Be-doped p^+ layer for the ohmic contact purpose. With reduced MBE growth temperature of about 350 °C, it was possible to dope this layer up to 5×10^{19} cm^{-3} Be.

In order to determine quality of the resulting laser materials, broad-area lasers

1000 Å
p+ InGaAs

1.5 μm
InAlAs
Be: 1 x 10^{18}

0.7 μm
InAlAs
Si: 1 x 10^{18}

n+ InP

2000 Å
Graded from InAlAs to
$In_{0.52}Ga_{0.24}Al_{0.24}As$

4 x 40 Å $In_{0.68}Ga_{0.32}As$ Wells

3 x 100 Å $In_{0.52}Ga_{0.24}Al_{0.24}As$ Barriers
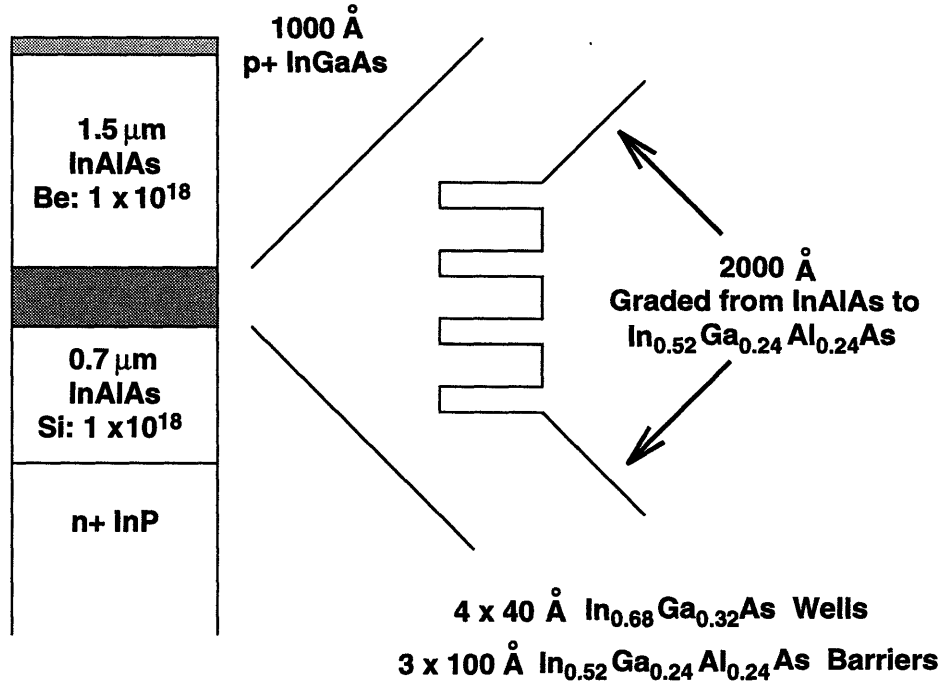
Figure 3-10: Layer structure of a strained multiple quantum well graded-index separate confinement laser

were fabricated in the following manner. First, 50- or 100-μm-wide stripes were patterned by wet-chemically etching[3] the top contact and most of the top cladding layer with a photoresist mask. Cr/Au top contact metal was evaporated on and patterned by lift-off. The back side was lapped down to about 100 μm and Cr/Au was deposited on the back for n-side metallization.

The finished sample was cleaved into laser bars of different cavity length and L-I (light vs. current) characterizations were done. Since the currents required for these large area devices to lase are very high, the characterization was done only with pulsed currents. The pulse duration was 200 nsec and the repetition rate was about 1 kHz. For the laser output power measurement, light from one facet of a device was collected into an integrating sphere with an InGaAs PIN detector located at one port. The induced photocurrent was converted into voltage with a fast trans-impedance amplifier[4]. This detection circuitry was calibrated with a known amount

---

[3]5:1:1 H_2O:H_2O_2:H_3PO_4 was used for this wet-chemical etching, which etches about 1 μm of InGaAs or InAlAs per minute.

[4]This trans-impedance amplifier was designed and made with the help of Dr. Anton Failla, a visiting scientist from Italy.

66

of optical power from a commercial 1.5 μm laser diode[5].

Figure 3-11 shows the resulting threshold current densities and inverse external quantum efficiencies at various cavity length. Each data point in the figure represents the best result obtained from 5 to 10 different devices with the same cavity length. The threshold current density was determined by dividing the measured threshold current with the device area. This quantity gets smaller as the cavity length gets larger since longer devices have smaller mirror losses. The lowest threshold current density achieved in the present study was 700 A/cm^2 for an about 2.5-mm-long device.

The external quantum efficiency η_{ext} can be easily converted from the slope of the L-I curve, using

$$\eta_{ext} = \frac{2q}{\hbar\omega} \frac{d\mathrm{P}}{d\mathrm{I}} \qquad (3.6)$$

This can be taken as the ratio of differential light output power (dP) to differential input power which, ignoring other resistive voltage drops, is the product of differential current (dI) and the bandgap energy in eV in the active layer ($\hbar\omega/q$). The factor of 2 is added because light power is usually measured from one facet. η_{ext} can be further divided into

$$\eta_{ext} = \eta_{int} \times S \qquad (3.7)$$

where η_{int} is the internal quantum efficiency, or the ratio of the radiative recombination rate to the total recombination rate which includes nonradiative as well as radiative recombination rates. S is the photon escape efficiency, or the ratio of the number of photons that escape out of the cavity to the number of photons generated. Since all generated photons either escape or get absorbed by the internal loss, S can be expressed as

$$S = \frac{\alpha_m}{\alpha_m + \alpha_{int}}, \qquad (3.8)$$

where α_m, the mirror loss, represents the photon escape rate and the sum of α_m and α_{int}, the internal loss, represents the photon generation rate. α_{int} is due to free carrier absorption, heterojunction interface scattering loss, and all other physical processes

---

[5]This laser was kindly donated by Dr. Peter Whitney at Lasertron.
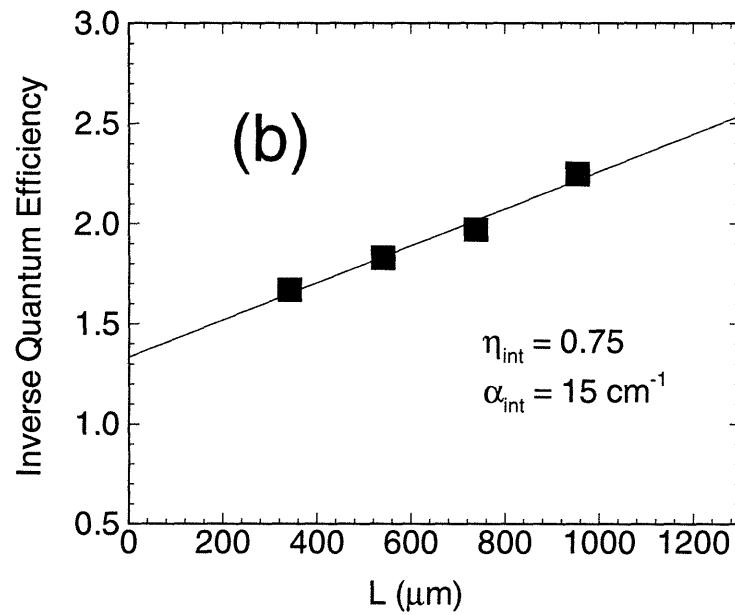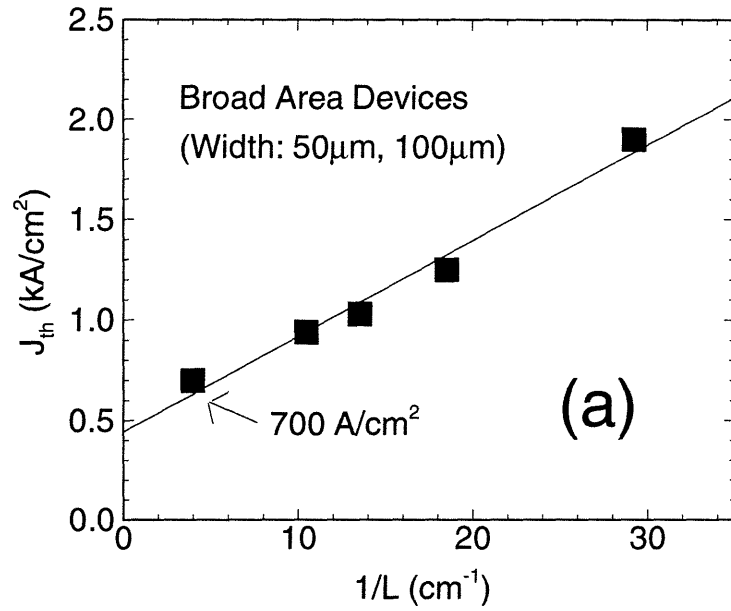
Figure 3-11: Broad-area laser device characterizations. (a) Threshold current density vs. inverse cavity length. (b) Inverse external quantum efficiency vs. cavity length.

(except the band to band absorption) that may consume photons. If the two facets
are identical,

$$\alpha_{\mathrm{m}} = \frac{1}{\mathrm{L}} \ln\left(1/\mathrm{R}\right) \tag{3.9}$$

with L being the cavity length, and R the mirror reflectivity. Inserting Eq.(3.8) and
Eq.(3.9) into Eq.(3.7), we get

$$\eta_{\mathrm{ext}}^{-1} = \eta_{\mathrm{int}}^{-1} \ [1 + \frac{\alpha_{\mathrm{int}}\mathrm{L}}{\ln(1/\mathrm{R})}]. \tag{3.10}$$

From this, it becomes clear that η_{ext} approaches to η_{int} as L goes to zero, and α_{int} can
be obtained from the slope of line in which η_{ext}^{-1} is plotted against L. This is precisely
what was done for data shown in Figure 3-11 (b). The estimated η_{int} is 0.75 and α_{int}
$15\,\mathrm{cm}^{-1}$.

In order to evaluate quality of the presently investigated laser material, published
results of 1.5 μm strained QW lasers with similar amounts of compressive strain and
QW numbers are compiled and compared in Table 3.1. From this comparison, the
following observations can be made. First, lasers with InGaAlAs strained MQW
structures have somewhat higher η_{int} than those with InGaAsP with the exception
of CBE-grown Sample (a). It is plausible that InGaAlAs QWs provide higher carrier
injection efficiency and better electron confinement with the larger conduction band
offset than InGaAsP and, consequently, higher η_{int}.

Second, lasers grown by MBE (Sample (e) and the present work) have larger α_{int}
than others grown by MOCVD or CBE. The major difference between these two
different sets of lasers lies in the cladding materials – InAlAs for MBE lasers and InP
for others – and it is plausible that inferior quality of MBE-grown InAlAs claddings
is the cause for larger α_{int}. It is well known that laser performance suffers from poor
material quality of AlGaAs layers if MBE growth is done at too low temperature [60].
This is usually blamed to bulk [61] or interface [62] nonradiative recombinations.
Nonradiative recombinations, however, would affect η_{int}, and in light of the above-
observed larger α_{int}, it would be interesting if a systematic study can be performed
on the loss mechanisms of MBE-grown InAlAs.

Comparisons of 1.5 μm Strained MQW Laser Diodes

Institution	Growth Technique	QW Structure (Strain)	J_{th} (cavity length)	α_{int}	η_{int}
AT&T Bell Labs [a]	CBE	4 InGaAs/InGaAsP (0.47 %)	370 A/cm^2 (3 mm)	3.8 cm^{-1} *	0.9
USC [b]	MOCVD	4 InGaAsP/InGaAsP (0.9 %)	324 A/cm^2 (1.5 mm)	5.6 cm^{-1}	0.63
Philips [c]	MOCVD	4 InGaAs/InGaAsP (1.2 %)	392 A/cm^2 (2 mm)	3.8 cm^{-1} *	0.54 *
Bell Core [d]	MOCVD	3 InGaAs/InGaAlAs & (1.2 %)	400 A/cm^2 (3 mm)	6.1 cm^{-1}	0.83
UCSB [e]	MBE	3 InGaAlAs/InGaAlAs (1.1 %)	538 A/cm^2 (1.2 mm)	9.4 cm^{-1}	0.83
Present Work	MBE	4 InGaAs/InGaAlAs (1.0 %)	700 A/cm^2 (2.5 mm)	15 cm^{-1}	0.75

*: Measurement done for single QW laser

&: Claddings are made of InP

Table 3.1: Comparions of published strained MQW (3 or 4 wells) laser performances. The data are obtained from References [54,55] for (a), [56] for (b), [57] for (d), and [59] for (e).

Third, Sample (e) grown by the same solid-source MBE has better performance than the present study. It is believed that wider strained QWs (100 Å) obtained in Sample (e) by the use of quaternary $In_{0.7}Ga_{0.2}Al_{0.1}As$ are the reason for the difference. The advantage of wider QW is that it gives an enhanced electron-hole overlap integral which results in higher values for optical transition matrix elements [12]. We have also proposed the very same concept of using wider strained quaternary InGaAlAs QWs for laser applications [63], but it has not been successfully implemented due to lack of prolonged growth period with our MBE machine toward the later part of the present study. It should be noted that strained quaternary InGaAsP QW lasers have been successfully tried with improved device performance as was done for Sample (b) in Table 3.1.

3.3.2 Ridge-Waveguide Devices

Once laser materials are grown and their qualities are verified with broad-area laser characterizations, devices that provide better lateral confinement of both injected carriers and optical waves need to be fabricated. The best lateral confinement scheme is using heterojunctions which require epitaxial regrowth. Regrowth, however, is not easily allowed with MBE-grown InGaAlAs materials because MBE is not very suitable for growth on nonplanar substrates which would be required for buried heterostructures. In addition, oxidation of aluminium in InAlAs would present a serious problem for the oxide removal step before the initiation of regrowth. Consequently, the lateral confinement in the present study is achieved by a more straightforward method of ridge waveguides, in which ridges formed by etching away portions of top claddings provide the required lateral confinement. In designing ridge-waveguide devices, there are two important parameters: width and height of the ridge as defined in Figure 3-12. In general, width of the ridge should be as narrow as possible in order to allow only the fundamental lateral mode and to minimize the volume of the pumped active region. Lithographic constraints set the limit of ridge width to 2 to 3 μm since a contact opening has to be made on top of the ridge. As for ridge height, the larger it is the better lateral confinement it provides since there will be less injected current

71
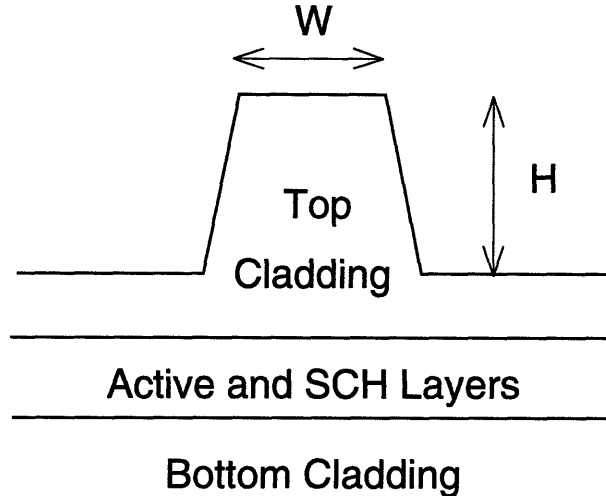
Figure 3-12: A schematic drawing of a ridge-waveguide laser

spreading and larger difference in effective indices inside and outside the ridge region. However, the etching should not be done beyond the active region since this will induce defects on the etched surfaces inside the active region. In practice, the ridge is formed by etching away the top cladding close to the top SCH layer but never beyond it. This requires a precise control of the ridge etching and, as a result, the technique of an etch stop layer with suitable selective etching is very attractive. Such a technique has been tried for InGaAsP ridge-waveguide devices with a mixture of H_3PO_4 and HCl acids selectively etching InP top cladding over InGaAsP SCH layers [64]. For our application, an AlAs etch stop layer was used with the selective etching solution of the succinic acid that etches InGaAlAs but not AlAs [65]. A 30-Å-thick etch stop layer was placed during the MBE growth of a laser material between the top cladding and GRINSCH layers so that the maximum confinements of the current and the wave can be achieved. In our experience of growing AlAs layers on InP, the thickness of 30 Å is below the critical layer thickness for strain relaxation under the MBE growth condition employed, and no material quality degradation due to the strained AlAs layer was observed from in-situ monitoring of RHEED, nor from x-ray and photoluminescence characterizations.

Ridge-waveguide devices were fabricated from a laser material grown by MBE whose layer structure is shown in Figure 3-13. This layer structure is very similar to

2000 Å
p+ InGaAs

30 Å AlAs

2.0 µm
InAlAs
Be: 1 x 10^{18}

well: 5 x 95 Å InGaAs
barrier: 4 x 80 Å In$_{0.52}$Ga$_{0.24}$Al$_{0.24}$As

1.0 µm
InAlAs
Si: 1 x 10^{18}

1800 Å GRINSCH

n+ InP
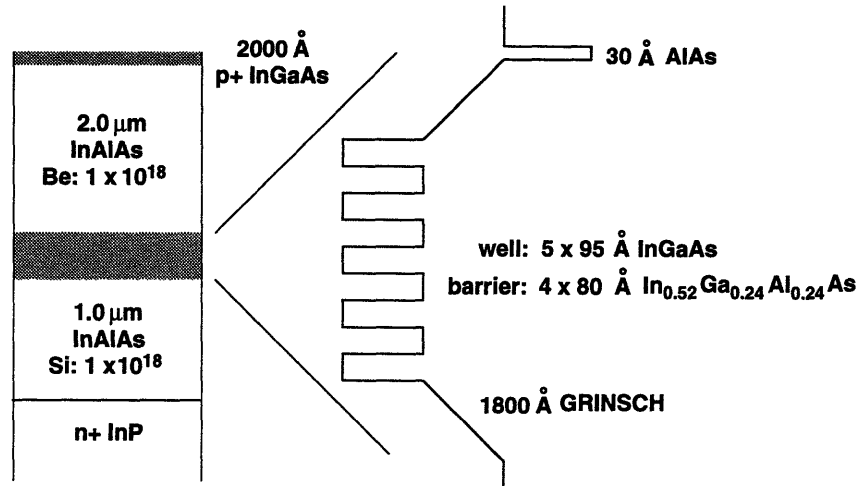
Figure 3-13: InGaAlAs MQW laser diode layer structure with an AlAs etch stop layer

the strained MQW laser structure shown in Figures 3-10 except that lattice-matched MQWs are used instead of strained MQWs. This type of lattice-matched MQW lasers had been tried in the early stage of the present study before the optimal strained QW structure was determined. The ridge-waveguide processing steps described below can be equally applicable to a laser structure with strained MQWs. In order to fabricate ridge-waveguide devices, stripes of various width were first formed by etching two parallel channels next to the stripe. The etching was done first with 5:1:1 mixture of DI water, phosphoric acid (H$_3$PO$_4$) and hydrogen peroxide (H$_2$O$_2$), which etches InAlAs with the etch rate of about 1 µm/min. The duration of etching was carefully timed so that the bottom of the etched channel was approximately 1500 Å above the etch stop layer. Immediately after this etching, the sample was immersed into the selective etching solution until the AlAs layer was exposed. The selective etching solution was made up of 15 parts succinic acid solution – 200 g of succinic acid in one liter of DI water – and 1 part hydrogen peroxide. The pH of the solution was regulated to the value of 4.2 by adding ammonium hydroxide (NH$_4$OH). The etch rate of InAlAs in this solution is about 60 nm/min and it takes more than 25 minutes for this etchant to break through the 3-nm-thick AlAs etch stop layer [66]. The etching was done in two steps since the etch rate of the selective etching solution was too slow to etch the entire top cladding layer by itself. The selective etching process can
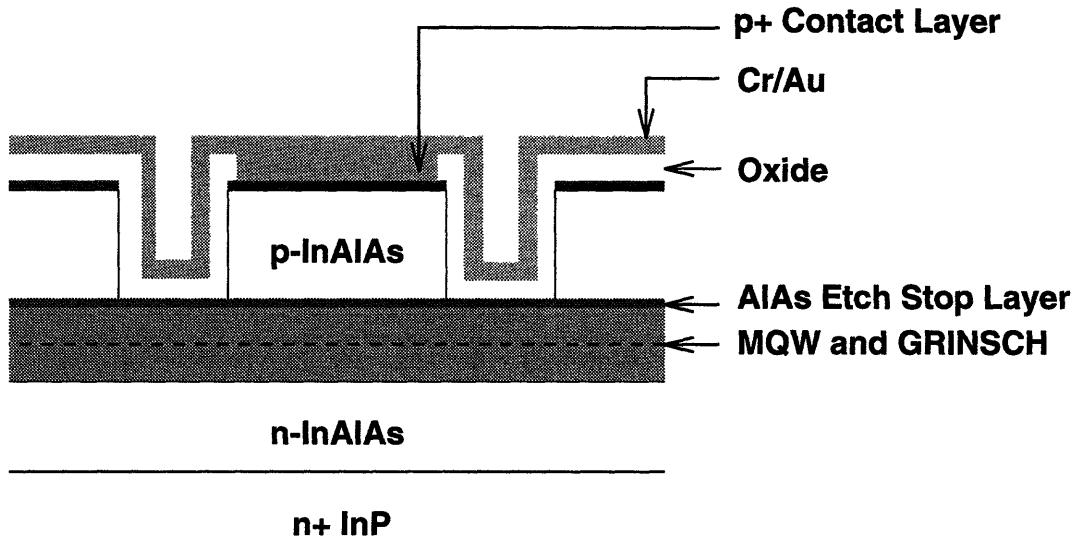
Figure 3-14: A schematic drawing for a ridge-waveguide laser with an etch stop layer.

be monitored by periodically inspecting the sample under the microscope; the slight roughness caused by the heavy Be doping on the top surface is maintained during the etching until the shiny AlAs layer is completely exposed, at which point the etching can be terminated. It was found, however, that the selective etching solution did not etch InAlAs very well if the sample was exposed to the air for long during the microscopic inspection. The cause of this is believed to be the surface oxidation of the exposed InAlAs that is not readily removed by the selective etching solution. Consequently, the best results were obtained if the exposure of the sample to the air during the selective etching process was minimized. After the selective etching, 2000-Å-thick PECVD SiO_x was deposited and contact openings were made on top of the stripes. Then, Cr/Au was sputtered for p-side metallization. Here, sputtering was done since it provided the required step coverage for the ridges with stiff side-walls. After lapping, AuGe (or Cr/Au) was evaporated to the back side of the sample. The finished ridge-waveguide device is schematically shown in Figure 3-14. Once the device fabrication was finished, the sample was cleaved into bars of different lengths and then cut into individual devices for characterizations. Figure 3-15 shows the light output power versus current for a 3-μm-wide device with a cavity length of 290 μm under pulsed current excitation. The device lases at 30 mA and has the external quantum efficiency of about 0.21 for a facet. It has the lasing wavelength of 1.52 μm
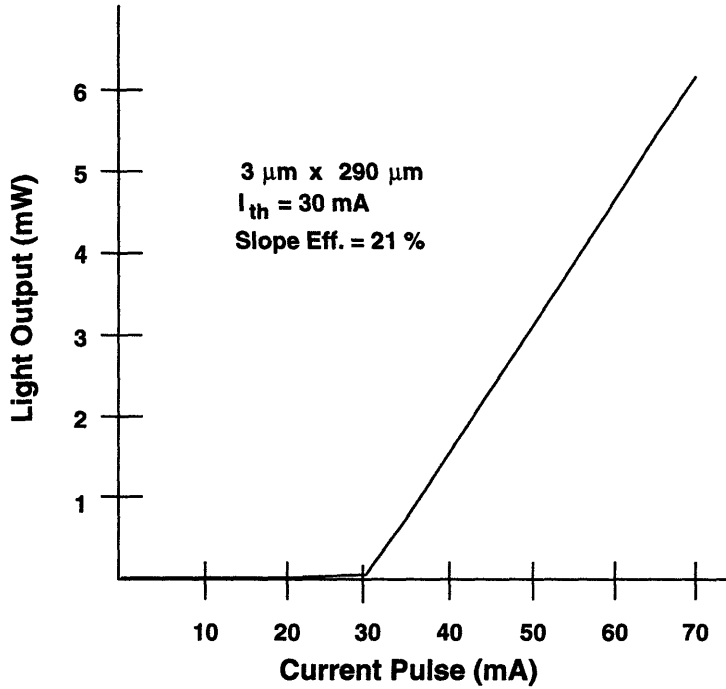
Figure 3-15: Light vs current for an InGaAlAs ridge-waveguide laser

and the far-field full width at half-maximum of about 15° as can be seen in Figure 3-16 and Figure 3-17, respectively. All the characterization was done at room temperature with 200-nsec-wide current pulses under nonpackaged probing contacts.
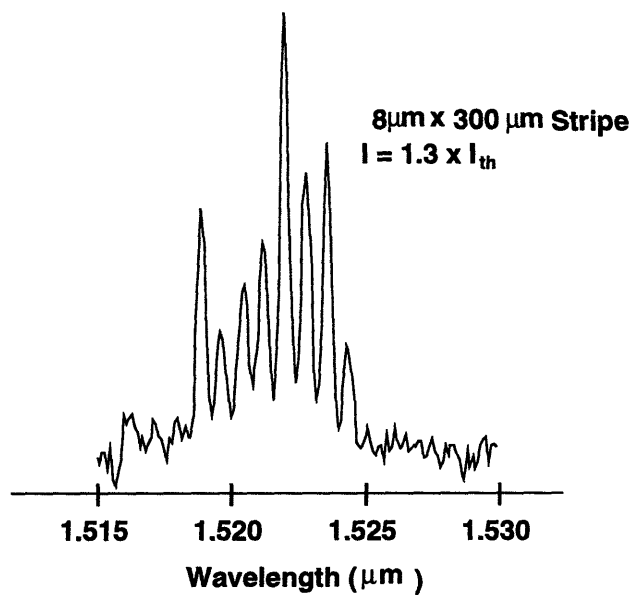
Figure 3-16: Lasing spectrum of an InGaAlAs ridge-waveguide laser
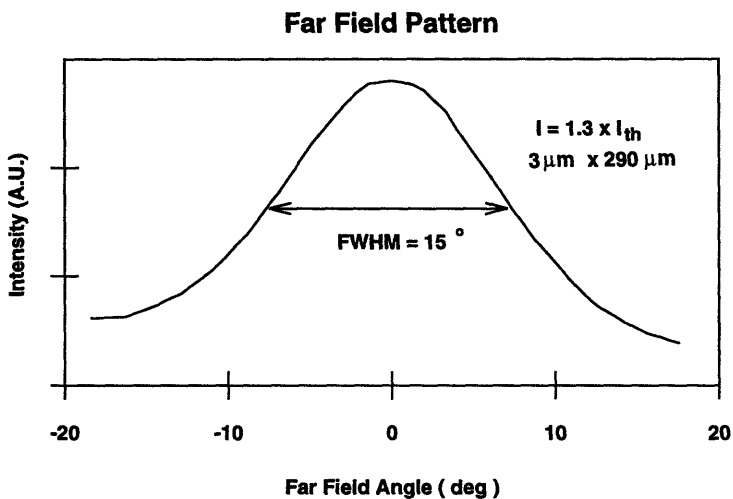
Figure 3-17: Far field pattern of an InGaAlAs ridge-waveguide laser

Chapter 4

Ridge-Waveguide Distributed-Feedback Lasers

4.1 Introduction

InP-based lasers must have excellent spectral characteristics in addition to low threshold currents and high quantum efficiencies in order to satisfy the requirements of long-haul optical communication, where the basic issues are to send from one place to another as much information as fast as possible with as little regeneration as possible. Although the details of how transmitter spectral characteristics affect the performance of given optical networks depend on particular modulation techniques employed, it is generally required that a semiconductor laser should have a single mode, or only one peak in its wavelength spectrum, and the linewidth of this single peak should be as narrow as possible. The single mode characteristic is achieved only if the two-dimensional transverse (parallel to the laser facets) waveguide inside the laser supports only the fundamental mode, and the cavity resonance condition supports only one dominant longitudinal (along the laser cavity) mode. The first requirement is easily satisfied by the proper design of the vertical layer structure and the lateral confinement structure, but the second one involves more work and this is the topic discussed in this chapter. No attempts have been made in the present study to address the issue of narrow linewidth since the laser linewidth study can be

done only after mature laser device technology is established, and even then with very sophisticated characterization techniques, which are beyond the scope of the present work.

A cleaved-facet semiconductor laser generally has multiple longitudinal modes as is experimentally shown in Figure 3-16 in the previous chapter. This is because the mode spacing in a Fabry-Perot cavity formed by two cleaved-facet mirrors is usually smaller than the laser gain spectrum width and, consequently, many modes can lase simultaneously when their gains are larger than the cavity threshold gain (or mirror loss) which is equal for all the Fabry-Perot modes. This point is illustrated in the upper part of Figure 4-1.

In order to achieve the desired single mode operation, a cavity design is required in which resonance modes with different resonance wavelengths have different values of threshold gains. If, in addition, design is properly done so that the gain peak is located near the resonance mode with the smallest threshold gain, then the lasing will occur predominantly at that resonance wavelength. The most common way of making such a cavity is using distributed-feedback (DFB). In a DFB laser, a periodic perturbation on the dielectric constant in the form of gratings is introduced, and the resonant wavelength which is closest to the Bragg wavelength of the introduced periodic perturbation has the smallest threshold gain. Lasing will occur only at this wavelength, thus achieving the single mode operation. This point is illustrated in the lower part of Figure 4-1.

Conventional DFB lasers require either epitaxial regrowth if gratings are located in the bottom or top cladding layer, or growth initiation on a corrugated substrate if gratings are first fabricated on the substrate. Neither of these methods is feasible in the present approach of making InGaAlAs 1.5 μm lasers with solid-source MBE technology since MBE is not best suited either for regrowth nor for growth on a patterned substrate. Since the single mode operation is an absolute requirement for 1.5 μm lasers for the optical communication application, a new approach that can overcome the above obstacle was called for. The approach that was developed in this work is the use of a ridge-waveguide (RWG) DFB laser. The concept of a

Cleaved-Facet Laser

Threshold Gain

Laser Gain

λ

Multiple Mode Operation

DFB Laser

Threshold Gain

Laser Gain

λ
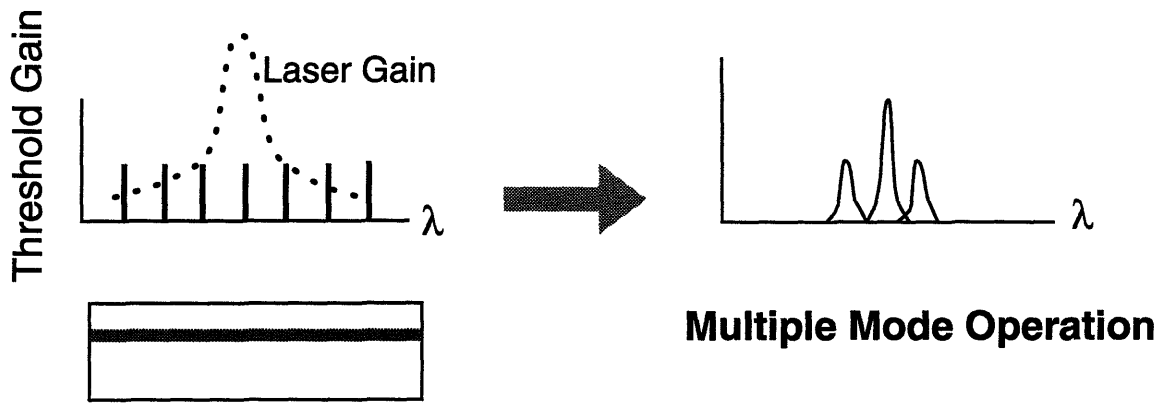
Single Mode Operation
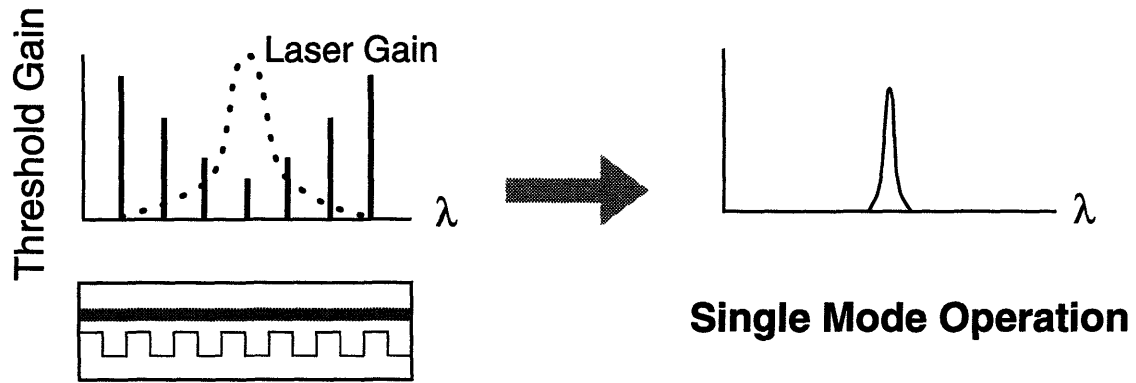
Figure 4-1: Multiple-mode operation for a cleaved-facet laser vs. single-mode operation for a DFB laser.
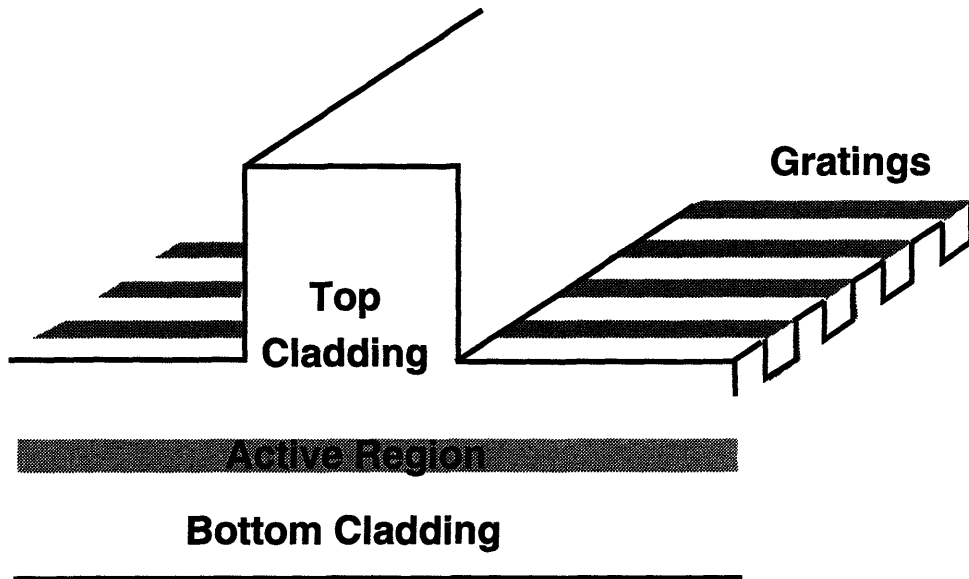
Figure 4-2: A schematic drawing of a Ridge-Waveguide DFB (RWGDFB) laser.

RWGDFB laser is schematically shown in Figure 4-2. As its name implies, RWGDFB is a DFB laser based on the ridge-waveguide device. Gratings are made on top of etched channels next to the ridge after the ridge formation, and, as a result, the grating fabrication step is entirely decoupled from the epitaxy step. In this way, all the complications of epitaxial regrowth and growth on the patterned substrate are avoided. With this proposed device structure, there are two issues that need to be addressed.

First, will this device work? Whether a DFB laser has the single-mode operation or not depends, first of all, on the strength of coupling coefficient κ, which represents the amount of coupling between the wave and the grating. The question if the proposed RWGDFB structure has a large enough κ can be answered by direct calculation of κ with a numerical method. The numerical method employed and the resulting κ values along with their dependence on various structural parameters are given in Section 4.2.

Second, can it be made? Although the proposed RWGDFB is a simple structure, fabricating it turns out to be a major challenge primarily because gratings have to be

made on a nonplanar structure. We attacked this problem with x-ray lithography and were able to fabricate the required RWGDFB structures. The developed fabrication steps are described in Section 4.4. In addition, while investigating the RWGDFB laser, it was realized that the proposed device structure has many advantages over the conventional DFB structures in which gratings are buried. These advantages are discussed in Section 4.3. With this realization, the above-mentioned simulation and fabrication works were done for a laser layer structure with InP claddings rather InAlAs so that our new DFB structure can appeal more directly to the DFB research community in which InP claddings are routinely used.

4.2 Coupling Coefficient Calculation

4.2.1 Method of κ Calculation

The coupled-mode theory is used for κ calculation [67]. According to the coupled-mode theory, the magnitude of κ for rectangular-shape gratings is given as [68],

$$\mid \kappa \mid = \frac{(n_2^2 - n_1^2)}{n_{\text{eff}} \lambda} \frac{\sin(\pi m \gamma)}{m} \Gamma, \tag{4.1}$$

where n_1 and n_2 are refractive indices of materials above and below the gratings; n_{eff} is the effective mode index of the waveguide; λ is the wavelength of interest; m is the grating order; γ is the grating duty cycle defined as Λ_1/Λ where Λ_1 and Λ are defined in the inset of Figure 4-3; Γ is the field overlap integral with the grating region, or the fraction of the unperturbed mode intensity residing inside the grating region. Although the perturbational approach of the coupled-mode theory may not be adequate for κ calculation if gratings are very deep in the conventional DFB structures [69], it is not the case for us since the amount of perturbation even with very deep gratings in the present investigation is very small as can be seen from the small κ values calculated in later sections.

In order to determine κ, numerical values of n_{eff} and Γ are required for a given RWGDFB structure. Both of these are determined from the fundamental mode pro-
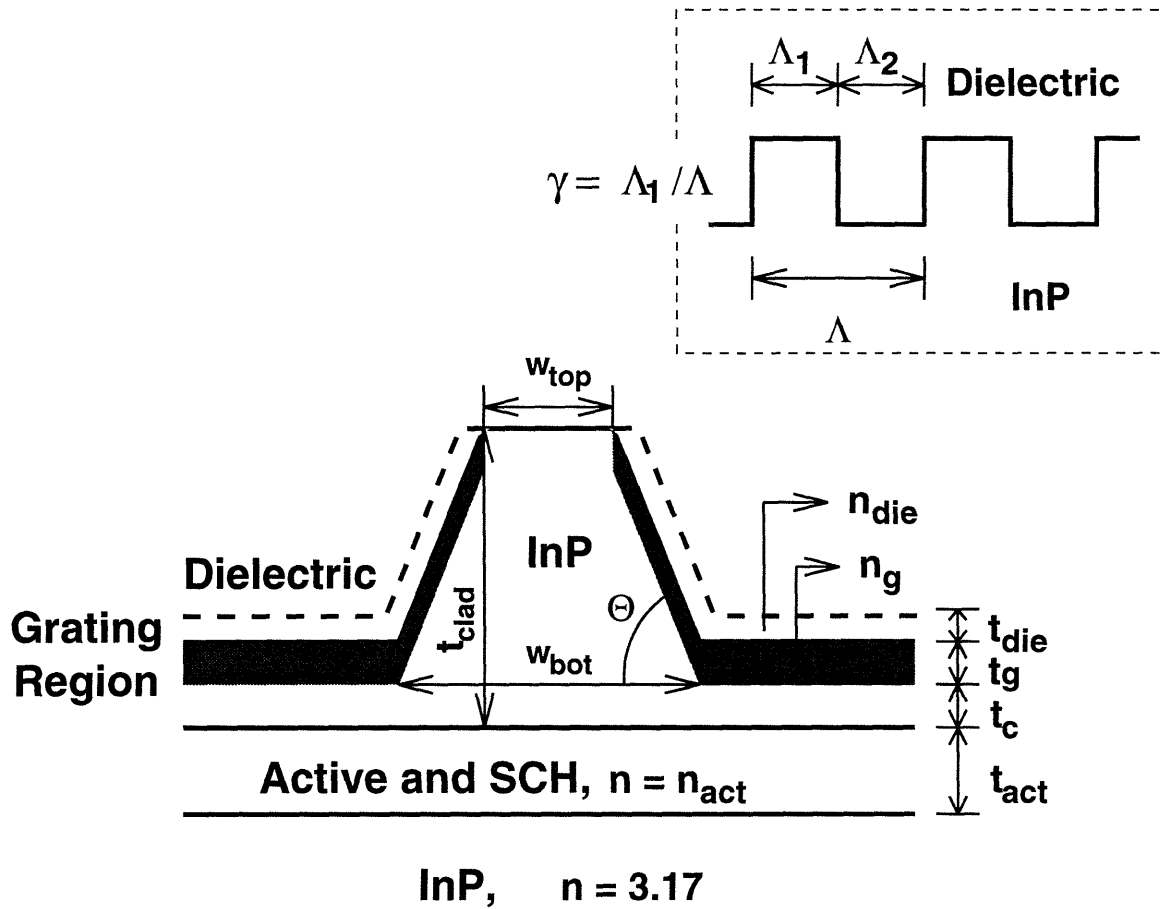
Figure 4-3: A generic RWGDFB structure with definitions for various parameters that are used for the fundamental mode profile calculation with the imaginary-distance beam propagation method. Approximations are made for n_{act} and n_g, details of which can be found in the text.

file calculated numerically with the imaginary-distance beam propagation method (IDBPM), which has been implemented by Jerry Chen and others at MIT [70]. Figure 4-3 shows a generic waveguide structure used for the field profile calculation by the IDBPM. Here, the grating region is represented by a homogeneous layer with a weighed average dielectric constant between the materials above (dielectric) and below (InP) the gratings [71], or in terms of refractive indices,

$$n_g^2 = \frac{\Lambda_1}{\Lambda} n_{die}^2 + \frac{\Lambda_2}{\Lambda} n_{InP}^2. \tag{4.2}$$

For simplicity in numerical calculations and in order to generalize many different active and SCH layer structures possible, the active and SCH layers are lumped together into one homogeneous layer with an effective refractive index, n_{act}, and thickness, t_{act}. n_{act} is determined in a similar manner to n_g, or

$$n_{act}^2 = \frac{\sum_i t_i n_i^2}{t_{act}}, \tag{4.3}$$

where t_i and n_i correspond to thickness and refractive index in each layer making up the active and SCH layers, and t_{act} is the total thickness or $\sum_i t_i$. This type of approximation is frequently used for MQW waveguides and the error in the propagation constant due to the approximation is known to be very small [72]. This approximation is not expected to cause any significant errors in our determination of κ, either, since we are only concerned with the field intensity in the grating region where the very details of the active and SCH layers do not matter too much as long as they are properly accounted for in an effective manner. Only the fundamental lateral mode with TE polarization is considered for calculation since it is most relevant for practical laser applications, especially so if compressively strained QWs are utilized. The wavelength of 1.55 μm and the first order grating (m = 1 in Eq. 4.1) are used for κ calculations.

The grid sizes used for IDBPM calculations are 0.1 and 0.02 μm within the area of 10 μm by 2.5 μm for x and y axes, respectively. The definition for of x and y axes can be seen in Figure 4-4. Under these conditions, the calculation takes a few minutes
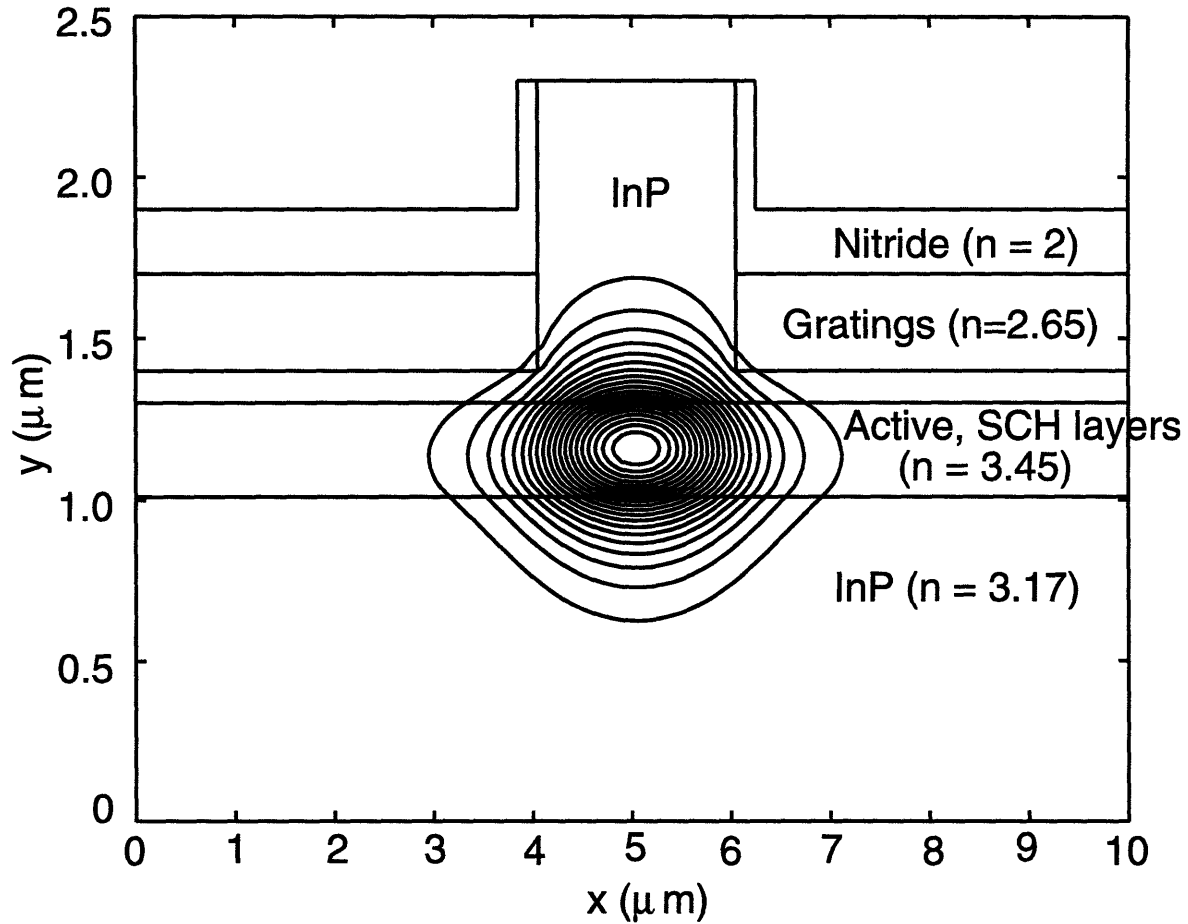
Figure 4-4: An example of a contour plot of the field intensity obtained by the IDBPM.

on a RS6000 workstation before the eigen mode profile and n_{eff} converge. Figure 4-4 shows a result of such IDBPM calculation in a contour plot of the field intensity along with the values of refractive indices used.

4.2.2 Dependence of κ on Active and SCH Layer Structures

InP-based lasers can employ many different active and SCH layer structures. A double-heterostructure (DH) laser, for example, can have a bulk InGaAsP active layer without any SCH layers, whereas a strained single QW laser has much thicker SCH layers than the active region. Since the different transverse field profiles resulting from such differences affect κ, it is necessary to understand the influence of the active and SCH layer structures on κ before other factors are considered. In order to cover

the wide ranges of n_{act} and t_{act} produced by Eq. 4.3 for different active and SCH layer structures, three sets of n_{act} and t_{act} are determined for laser structures found in the literature and their κ values in identical RWG structures are calculated and compared: $n_{act} = 3.57$ and $t_{act} = 0.2\,\mu$m representing a typical DH laser with a bulk InGaAsP active layer of $\lambda = 1.55\,\mu$m, $n_{act} = 3.45$ and $t_{act} = 0.31\,\mu$m obtained from a strained MQW (five wells) laser structure studied in Reference [73], and $n_{act} = 3.31$ and $t_{act} = 0.21\,\mu$m obtained from a strained single QW laser structure reported in Reference [55]. Refractive indices for given InGaAsP compositions are obtained from Reference [74]. For QWs, the refractive index of bulk material is used that has the same band-gap as the ground state electron-to-heavy-hole transition energy in the well.

The filled squares in Figure 4-5 show the calculated κ values for the above three sets within a RWGDFB structure described by the parameters shown in the inset. Clearly, κ depends on n_{act} and t_{act}. In order to better understand this dependence, κ values are calculated for some additional values of t_{act} for each n_{act} and are shown as empty squares in Figure 4-5. As shown in the figure, higher n_{act} gives larger κ at fixed t_{act}. Also κ peaks at a certain value of t_{act} with given n_{act}, where the peak position increases with decreasing n_{act}. This dependence is entirely due to the different overlap integral, Γ, resulting from the different field profiles with different values of n_{act} and t_{act}. Since the variation in κ for ranges of n_{act} and t_{act} of interest is not too great and the number of parameters involved needs to be reduced, we use $n_{act} = 3.45$ and $t_{act} = 0.3\,\mu$m for the subsequent investigations. In other words, all our investigation in the following sections are based on the epitaxial layer structure used in Reference [73]. This is only a choice of convenience and all the observations should hold qualitatively for different layer structures that may be more desirable for specific applications.

4.2.3   Dependence of κ on Ridge Structures

Since κ in the present RWGDFB laser is influenced by any elements that change the field profile, such elements need to be identified and their influence on κ investigated. Here, we consider four such elements: width of the ridge, the ridge side-wall angle
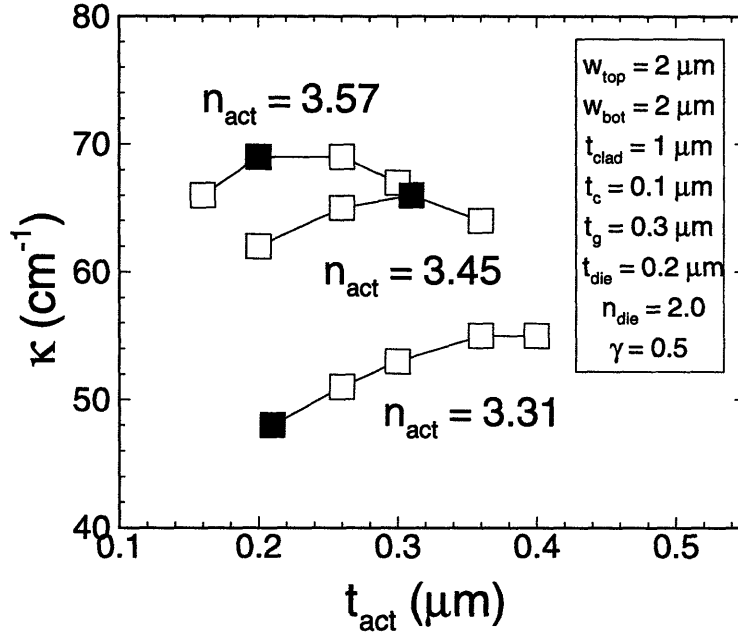
Figure 4-5: κ dependence on various combinations of n_{act} and t_{act}. Filled squares represent three laser structures taken from the literature as mentioned in the text.

(Θ), the separation between the grating region and the active and SCH layers (t_c), and the refractive indices of dielectric materials covering the ridge (n_{die}).

Figure 4-6 (a) shows the dependence of κ on the ridge width ranging from 2 to $4\,\mu m$, the usual range for RWG lasers. It shows that a narrower ridge width gives larger κ, an expected result since a narrower ridge provides less lateral optical confinement and, hence, more field leaking out to the grating region. Furthermore, the sensitivity of κ to the ridge width variation is higher for narrower ridges. This implies that RWGDFB lasers with extremely small ridge widths are not desirable since they may suffer from a severe fluctuation of κ. In fact, the high κ value obtained for very narrow ridges is not optimal for actual device applications, either, since a κL product (L is the laser cavity length) of only about 1.25 is desirable [75]. If κL is too high, spatial hole burning reduces the gain margin against undesired side modes; if κL is too low, distributed feedback is insufficient. κL of 1.25 corresponds to κ of $25\,cm^{-1}$ for a typical cavity length of $500\,\mu m$ and, thus, if other parameters are kept the same, a device with a 3-μm-wide ridge is more desirable than $2\,\mu m$ as far as κ is concerned.
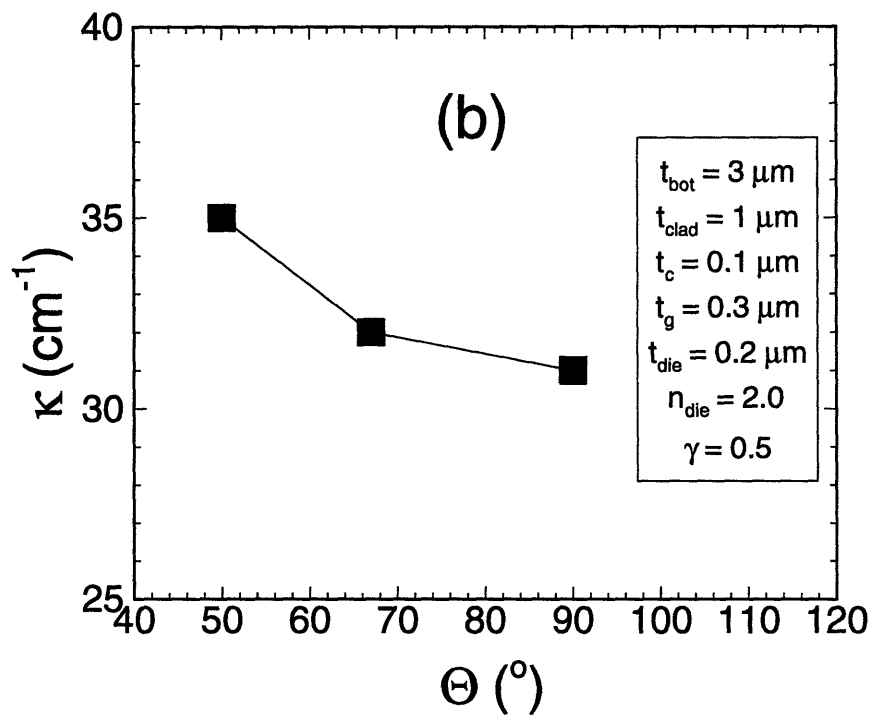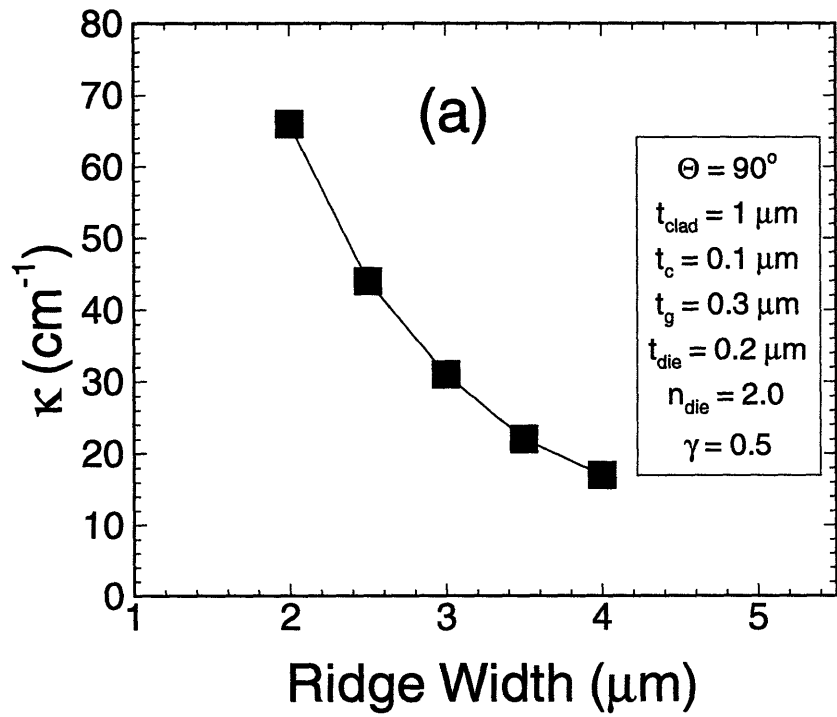
Figure 4-6: κ dependence on (a) ridge width, and (b) the side-wall angle.

For the investigation of Θ dependence, the bottom width of the ridge, w_{bot}, is kept at $3\,\mu\text{m}$, and the top width, w_{top}, is reduced in order to distinguish the influence of Θ from that of the ridge width investigated above. Under this condition, Figure 4-6 (b) shows that Θ does not greatly affect κ. This is because the field decays relatively quickly in the top cladding and decreasing the top ridge width does not greatly affect the overall field profile.

Figure 4-7 (a) and (b) show the dependence of κ on t_c and n_{die} respectively. As can be seen, κ decreases as t_c increases since the field decays rapidly in the cladding below the grating region. On the other hand, κ increases only slightly as n_{die} increases. Although larger n_{die} gives slightly larger κ because the field is pulled more into the grating region with larger n_g resulting from larger n_{die} (See Eq. 4.2), this is a minor effect. The κ dependence on dielectric materials can be ignored for practical purposes given reasonably deep gratings. The values of n_{die} used are selected from three possible dielectric materials: SiO_x with the refractive index of 1.5, polyimide with 1.8, and SiN_x with 2.0.

4.2.4 Dependence of κ on Grating Structures

Three factors are considered here: grating etching depth (t_g), the grating duty cycle (γ), and the lateral proximity of gratings to the ridge. Figure 4-8 (a) and (b) show the dependence of κ on t_g and γ, respectively. The κ dependence on t_g reveals that κ saturates quickly as t_g increases. This is because the field in the grating region decays quickly with the relatively low value of n_g. From the perspective of κ stability, grating etch depths larger than $0.2\,\mu\text{m}$ should be preferred since then κ is not very sensitive to the variation in t_g. The required gratings have a higher aspect ratio than those in conventional DFB structures, but such gratings can be easily fabricated with dry etching techniques [76].

The κ dependence on γ is due to the different field profiles caused by different n_g values resulting from different γ values (See Eq. 4.2). Although the $\sin(\pi\gamma)$ term in Eq. 4.1 is maximum at $\gamma = 0.5$, Γ becomes larger for larger γ since the field decays less rapidly in the grating region with larger n_g. This strong dependence of κ on
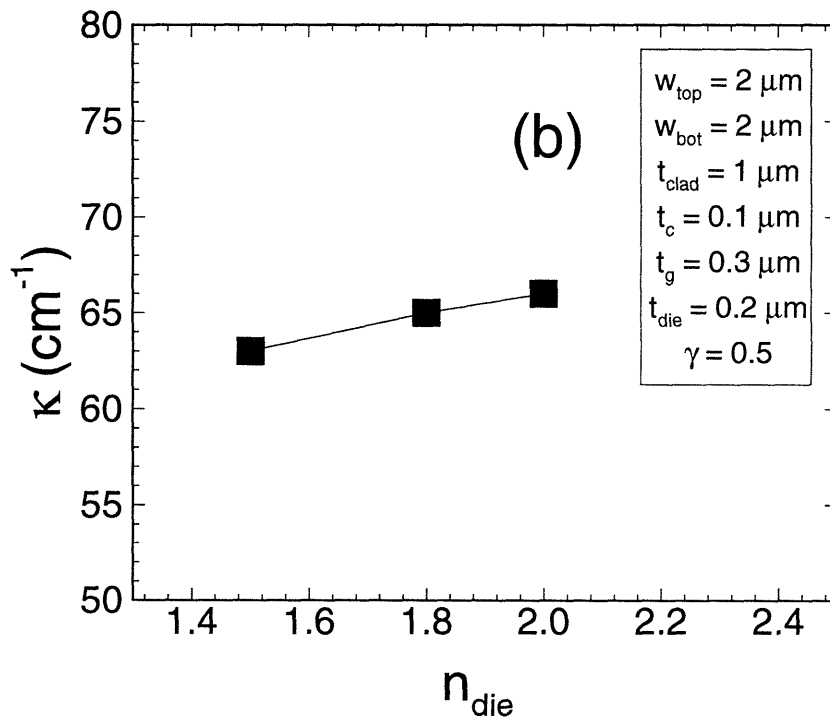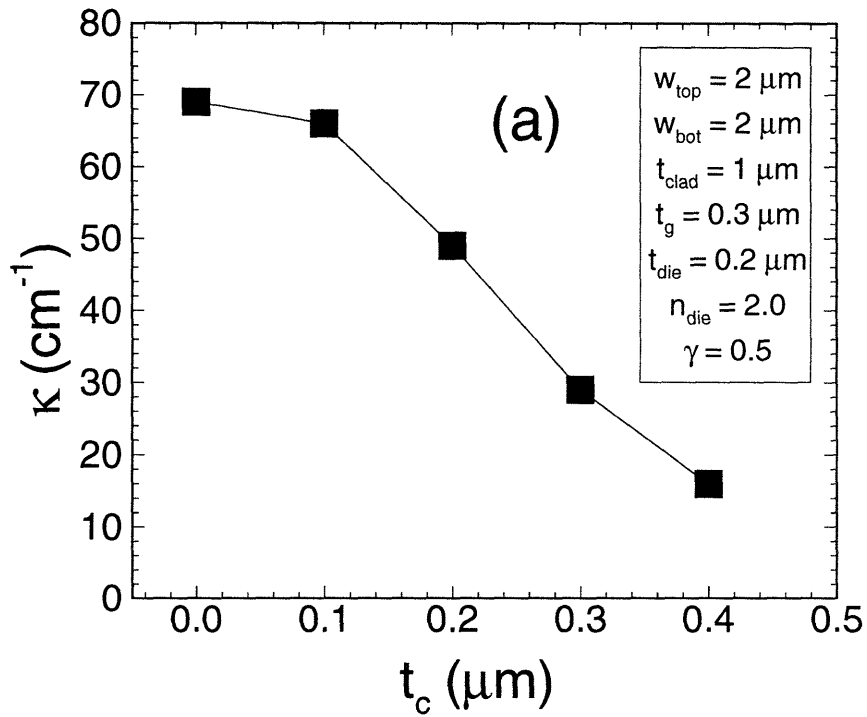
Figure 4-7: κ dependence on (a) t_c, the separation between the grating region and the active and SCH layers, and (b) n_{die}, the refractive index of the dielectric material covering the ridge.
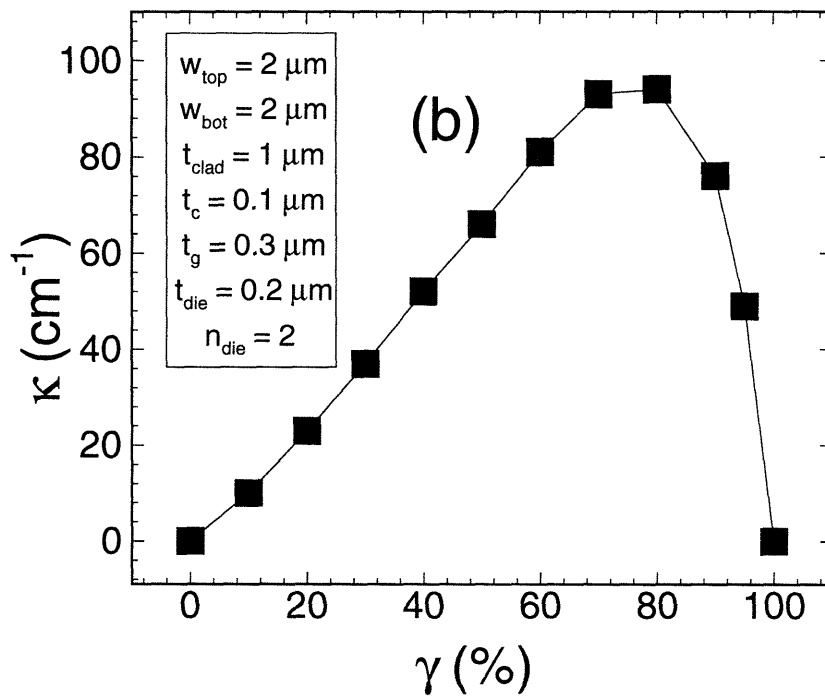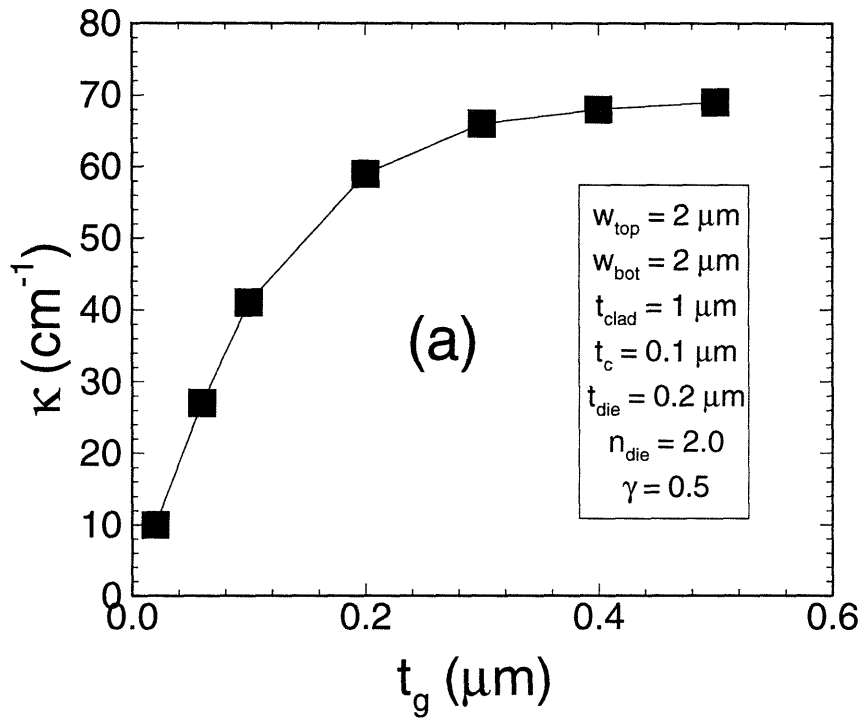
Figure 4-8: κ dependence on (a) t_g, the grating etching depth, and (b) γ, the grating duty cycle. γ is larger if less InP is etched away.
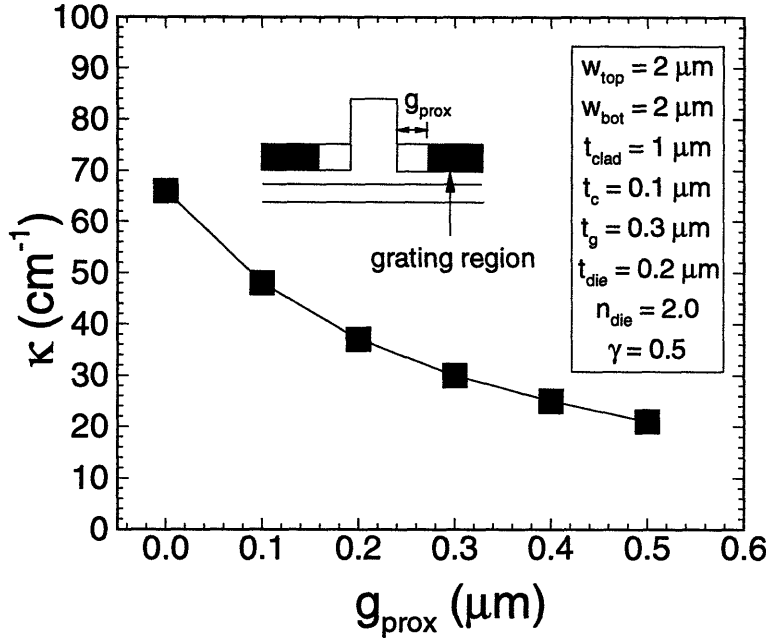
Figure 4-9: κ dependence on the grating proximity to the ridge, g_{prox}, where the definition of g_{prox} is shown in the figure.

the grating duty cycle is a unique feature for the present RWGDFB structure; in conventional DFB structures with buried gratings, there is very little change in Γ as the grating duty cycle changes and the only γ dependence comes from the $\sin(\pi\gamma)$ term.

Figure 4-9 shows the dependence of κ on the proximity of gratings to the ridge. By this, we are interested in how close gratings are fabricated to the ridge and its influence on κ, as schematically shown in the figure. The figure shows that κ decays rapidly as the grating region moves away laterally from the ridge side-wall. For actual device fabrication, it is then desired that this proximity is well controlled. This is an issue of importance since it is not an easy task to reliably fabricate gratings in the region right next to the ridge where there will exist a huge thickness variation of spun-on resists. The conventional grating fabrication techniques such as holographic and electron-beam lithography would have difficulty in fabricating gratings in such regions. However, this can be accomplished without difficulty by x-ray lithography that has large depth-of-focus and no proximity effect. We have demonstrated this

by patterning 230 nm PMMA gratings on a 1.8-μm-high ridge with 60 degree side-walls [77] and, as discussed in Section 4.4, succeeded in fabricating 0.25-μm-deep InP gratings right next to an 1.0-μm-high ridge with vertical side-walls.

4.3 Advantages of Ridge-Waveguide DFB Lasers

The results of the above investigations should be of great help in designing a RWGDFB laser with a target value of κ. Although details of the layer structure given and the ridge and grating structures required by the processing considerations may differ from case to case, the qualitative aspects of the κ dependence on the parameters investigated above should still hold. With the separation of epitaxy growth and grating fabrication, and the κ tuning capability through straight-forward processing modifications, an approach can be easily envisioned in which one first finds out the qualities of the epitaxially grown laser materials and the characteristics of RWG devices without gratings, and designs and fabricates a RWGDFB structure that achieves the required single-mode operation at the target wavelength. It is believed that this type of *modular* approach is much simpler than the conventional way of making buried heterostructure (BH) DFB lasers and, consequently, much more cost-effective. In fact, there are emerging research efforts to replace BH laser devices used in the local-loop application with RWG devices for the reason of superior cost effectiveness of RWG devices [78]. Such attempts are now successful because the current state-of-the-art epitaxy technology provides such excellent material qualities that even RWG lasers can be sufficient enough for many demanding applications. It is easily conceivable that the same approach can be taken toward reducing the cost of DFB lasers with the present RWGDFB devices.

There are two additional advantages of RWGDFB over the conventional BH DFB structures that deserve discussions. First, the effective mode index, n_{eff}, in RWGDFB is less sensitive to possible processing variations. The processing variation of particular concern here is that occurring during the stripe etching for the active region definition before regrowth in BH and for the ridge formation in RWG devices. Any
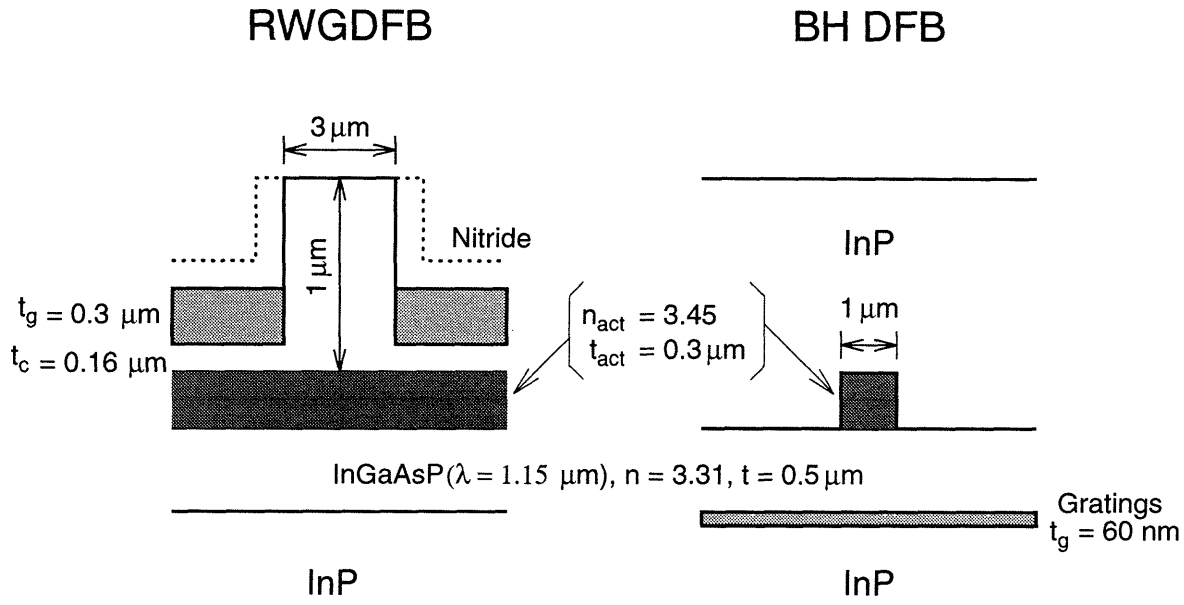
RWGDFB   **BH DFB**

Figure 4-10: Schematic drawings of (a) RWGDFB and (b) BH DFB structure that are used for the investigation of the sensitivities of n_{eff} and other parameters to variations in the etched stripe width.

etching processes have within-the-wafer or wafer-to-wafer nonuniformity, and it is extremely important that a device structure guarantees device parameters that are insensitive to such variations. In order to investigate n_{eff} sensitivities to variations in etched stripe width, the change in n_{eff} of RWGDFB and BH DFB was calculated as a function of the change in etched stripe width. Figure 4-10 schematically shows RWGDFB and BH DFB structures that were used for this comparison. The device structures are selected so that, first, the resulting κ is about $25\,\mathrm{cm}^{-1}$ as required for practical applications and, second, the stripe width is minimized to suppress higher-order modes. The selected structures were checked not to have any higher-order modes by calculating the allowed propagation constants with the effective index method in which each required effective index is determined by the transfer matrix method. As can be seen in the figure, this results in much narrower active layer width for the BH DFB. For convenience, the BH DFB structure is used in which gratings are fabricated on the substrate. This requires a layer structure with a quaternary layer, whose composition is set to give the bandgap of $1.15\,\mu$m. For a fair comparison, the same layer

93

structure is used for the RWGDFB.

The results of this comparison are shown in Figure 4-11 (a) and (b). Figure 4-11 (a) shows the change in κ and (b) in n_{eff} as well as in the Bragg wavelength, λ_{Bragg}. The BH DFB and RWGDFB show comparable sensitivity in κ whose magnitude may not be a great concern, but the change in n_{eff} is much larger for BH DFB. This is the direct result of the fact that the lateral optical confinement inside the buried active region in a BH DFB laser is very strong and a little variation in the active layer width can result in a larger change in the lateral field profile. The facts that BH DFB requires very narrow active width that suffers more from the change in the lateral field profile and that such stripes are usually made with wet-chemical etching, which is more prone to processing variations but minimizes surface damage before regrowth, make the situation worse for BH DFB lasers.

In Figure 4-11 (b), the change in λ_{Bragg} is directly proportional to that in n_{eff}. This is because λ_{Bragg} in a DFB laser is determined by $\lambda_{Bragg} = 2 \times n_{eff} \times \Lambda$, where Λ is the grating period. The change in λ_{Bragg} shown in the figure is calculated by assuming a grating period that gives λ_{Bragg} of $1.55\,\mu m$ for n_{eff} without any change in stripe width. As can be seen, RWGDFB has very minimal change in λ_{Bragg} whereas BH DFB has as much as $20\,\text{Å}$ change. Certainly, the yield for desired λ_{Bragg} will be higher for RWGDFB than BH DFB. The requirement for the tight control of n_{eff} is even more stringent, as pointed out by Tsang et al. [79], for wavelength-division-multiplexing applications in which different channels need to be separated by about 8 to $16\,\text{Å}$, and the lasing wavelength variation within one channel has to be much less than the channel separation. It should be noted, however, that the insensitivity of n_{eff} in RWGDFB is due to nature of waveguiding in RWG and has nothing to do with the location of gratings, and, consequently, the same advantage equally applies to a RWGDFB structure in which gratings are made on the substrate or buried by re-grown semiconductor.

Second, advanced techniques, such as phase-shifted gratings and a DFB structure with nonuniform κ, that enhance the yield of the single-mode operation at the desired lasing wavelength can be easily implemented with the present RWGDFB structure.

94
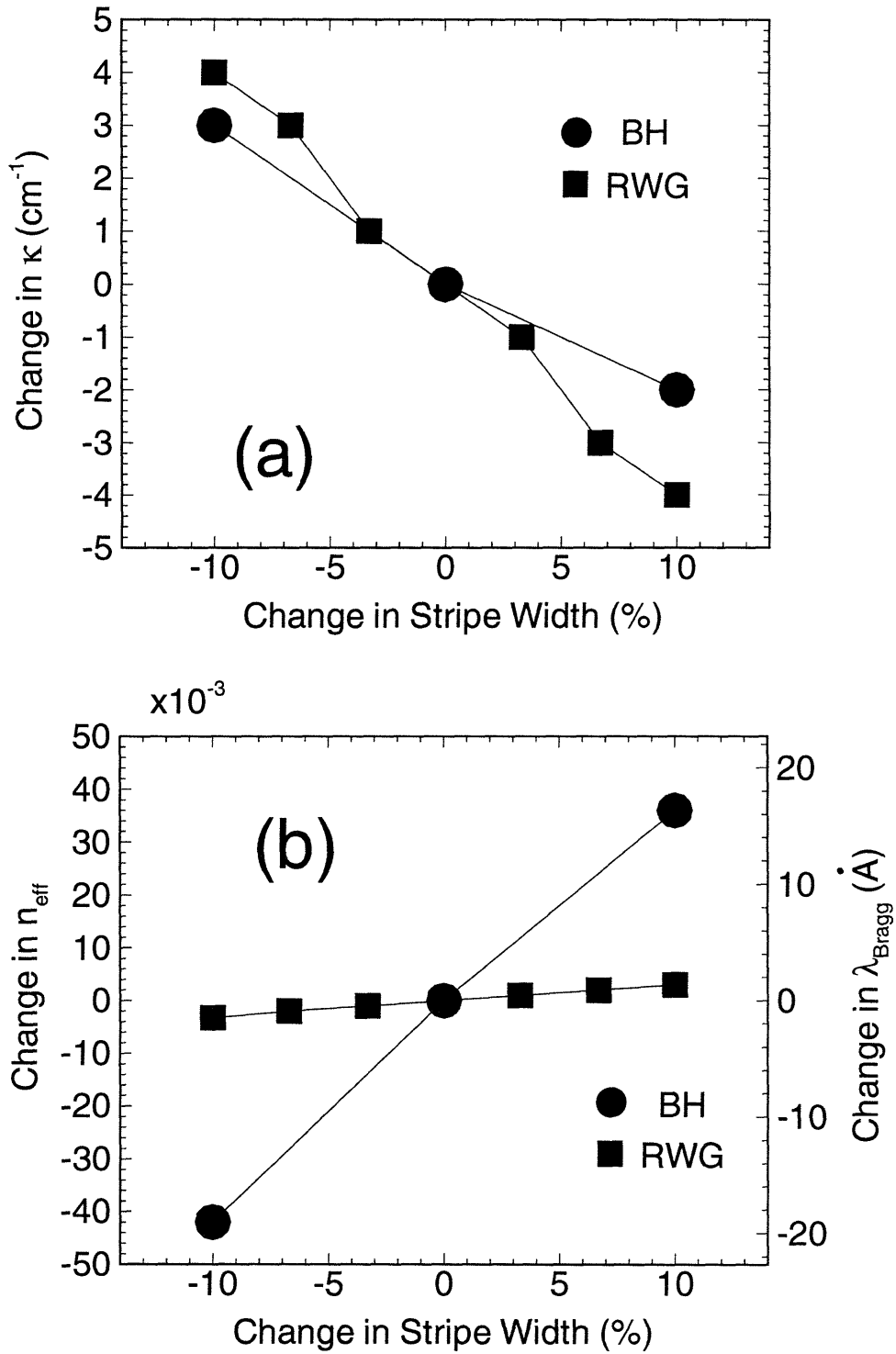
Figure 4-11: Changes in (a) κ and n_{eff}, and (b) Bragg wavelength calculated for changes in the stripe width.

In DFB lasers without phase-shifted gratings, the mode spectrum is symmetric about λ_{Bragg} with two competing modes at the equal separation from λ_{Bragg}, and the selection of the lasing mode among these two is determined by the phases of the cleaved-facet reflection. Since these phases are determined by the distance between the facet and the last complete grating period, they can not be controlled, so the selection among two competing modes is random. To eliminate such uncertainty, $\lambda/4$ phased-shifted DFB lasers are widely used. In addition, in order to further enhance the yield of the single-mode operation, spatial hole burning that reduces the side-mode gain margin [75] needs to be minimized. This can be achieved by any technique that ensures a longitudinally uniform photon distribution inside the laser cavity, and has been demonstrated with multiple-phase-shifted gratings [80], corrugation-pitch-modulated gratings [81], and DFB structures with longitudinally varying κ [82]. The usual methods for implementing these advanced techniques, however, are quite complex and their utility in an actual manufacturing environment may be questionable. With the RWGDFB laser presently investigated, such complexity is not an issue since the device processing sequence is not affected at all with the introduction of any of the above-mentioned techniques, assuming of course a suitable lithographic technique is available. For example, devices with longitudinally varying κ can be easily implemented, as can be seen from Figure 4-8 (b), if the lithography technique provides gratings with a varying duty cycle. We believe x-ray lithography with an electron-beam written mask is the technology of choice for these applications. Once a mask is made by electron-beam lithography for the desired grating patterns, the mask can be repeatedly used for grating fabrication with x-ray lithography, a much simpler task than direct electron-beam writing of gratings for each individual device. Furthermore, the recent development of spatial-phase-locked electron-beam lithography, in which fiducial grids are used to provide feedback on beam location [83], promises to produce x-ray masks for RWGDFB lasers without any sacrifice on the side-mode suppression gain margin due to stitching errors which can be a problem for direct electron-beam written gratings [84].

4.4 Ridge-Waveguide DFB Structure Fabrication

In order to fabricate a RWGDFB device with the above-discussed advantages, we developed processing steps that utilize CH_4/H_2 reactive-ion-etch (RIE)[1] and x-ray lithography[2]. Figure 4-12 schematically shows the developed processing steps. For convenience, this processing development was done using a blank InP wafer but it can be easily extended to the fabrication of real RWGDFB devices. First, about 1000-Å-thick SiO_x is sputtered[3] on an InP wafer, and patterned into about 3-μm-wide stripes by buffered-oxide-etchant (BOE) wet-chemical etching with a photoresist mask. Then, using the oxide as a mask, about 1-μm-high InP ridge is formed by reactive-ion etching of InP with CH_4/H_2. The RIE condition was optimized so that smooth etched surfaces are obtained with a reasonable etch rate: the conditions are 10 sccm for the CH_4 flow rate, 50 sccm for the H_2 flow rate, 20 mTorr for the chamber pressure, and about 400 V for the electrode bias voltage, and 200 W for the incident RF power with the resulting etch rate of about 400 Å/min. We decided to use for ridge formation RIE rather than wet-chemical etching since dry etching is favored over wet etching with its superior reproducibility and uniformity, and our intention is to show that the proposed RWGDFB structure is more manufacturable than the conventional DFB. Next, about 500-Å-thick oxide is deposited. The previous 1000-Å-thick oxide mask is intentionally left on top of the ridge so that the resulting 1500-Å-thick oxide layer prevents grating formation on top of the ridge as will be explained shortly. The sample, then, goes through the x-ray lithography step in which poly (methylmetharcrylate) (PMMA) resist is spun on the sample, baked at 180°C for an hour, exposed to x-ray through an x-ray mask, and developed. The details can be found for our x-ray exposure set-up in Reference [85], and for fabrication of the x-ray mask by holographic lithography in Reference [86]. The resulting PMMA

---

[1]RIE was done using the Plasma-Therm RIE machine located at Polaroid's microelectronics laboratory due to generous help of Dr. Kathy Meehan at Polaroid.

[2]The x-ray lithography step was performed by Vincent Wong at MIT's Nanostructure Laboratories.

[3]Sputtered oxide was used as a matter of convenience. PECVD oxide or nitride could have been used as well.
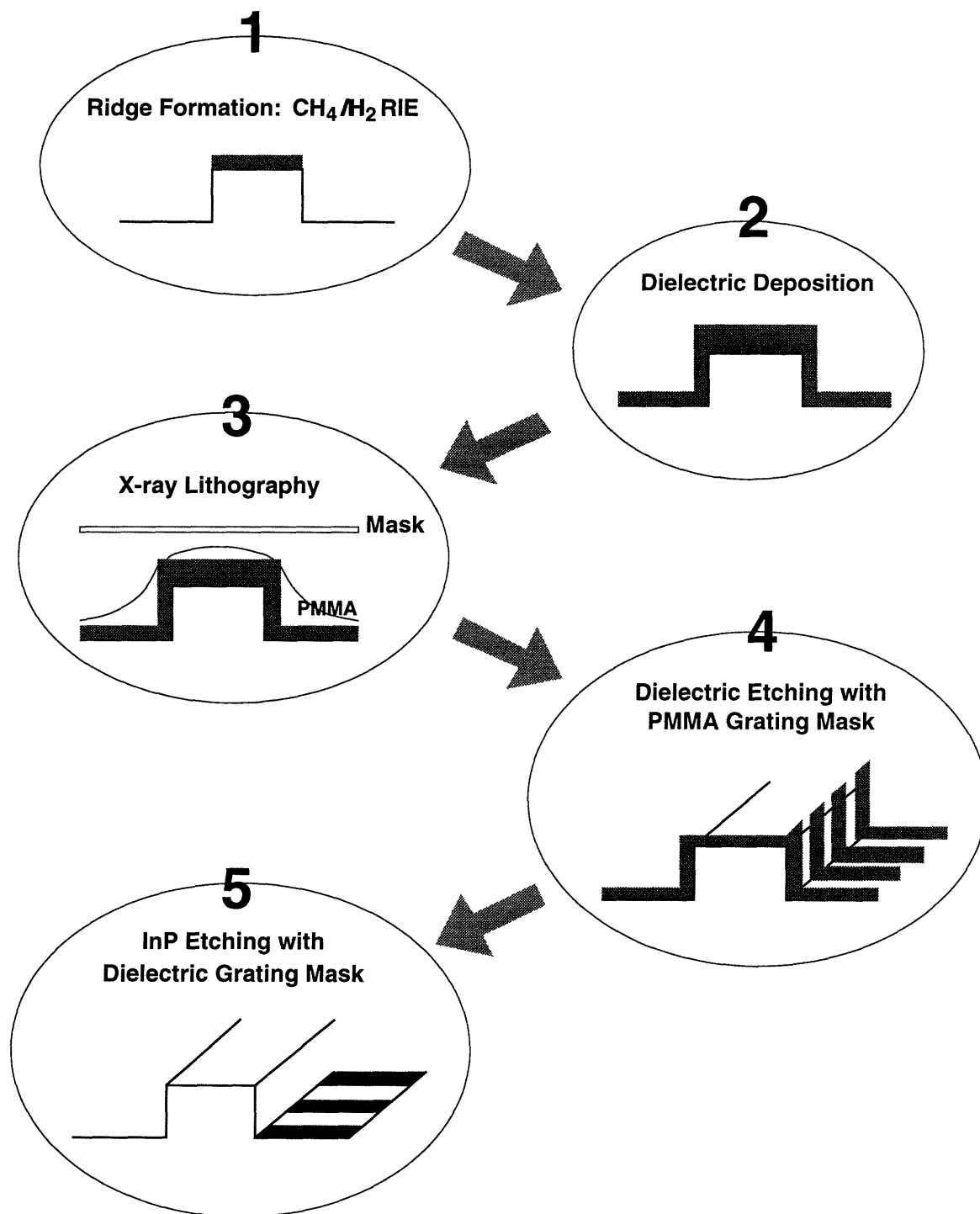
Figure 4-12: Processing steps for making a RWGDFB laser structure.
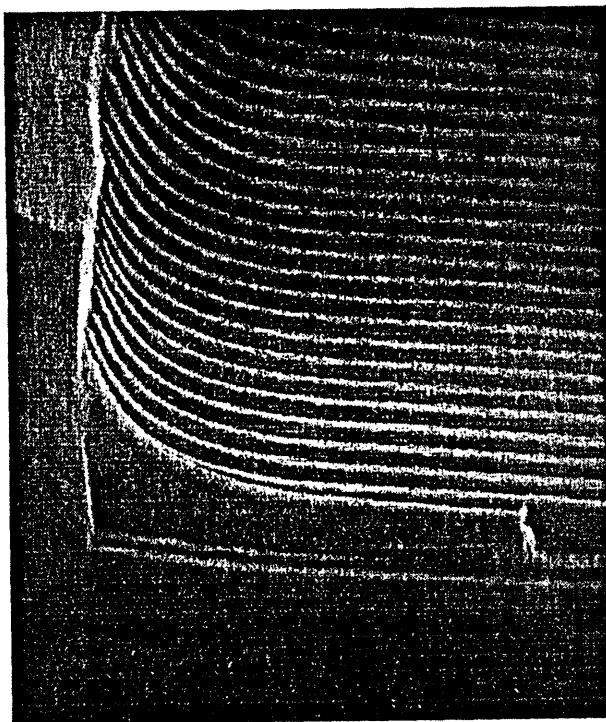
Figure 4-13: A SEM picture of PMMA gratings exposed by x-ray lithography.

gratings are shown in Figure 4-13. As can be seen, the profile of PMMA spun on the ridge has nonuniform thickness; it is much thicker right next to the ridge but becomes gradually thinner away from the ridge. Very little PMMA survives on top of the ridge since PMMA is thinnest there when spun and, exposure and development times are determined in order to completely pattern the thickest portion of PMMA. The PMMA gratings are, however, just fine on the channels next to the ridge where it matters most. Using this PMMA grating as a mask, oxide gratings are formed by CHF_3 reactive-ion etching of oxide. The resulting oxide gratings are shown in Figure 4-14. This oxide etching is carefully timed so that unmasked oxide on the channels is completely etched but thicker unmasked oxide on the top is not. Although the oxide on the sidewall is thin, it does not get completely exposed since the horizontal etch rate is smaller than vertical in RIE. In this way, the top and the sides of the ridge are left covered with oxide, which prevents formation of gratings there during CH_4/H_2 RIE in the next step. Once PMMA is stripped off, another CH_4/H_2 RIE is performed under the same RIE condition as the previous one to etch about 0.25-μm-deep gratings. The
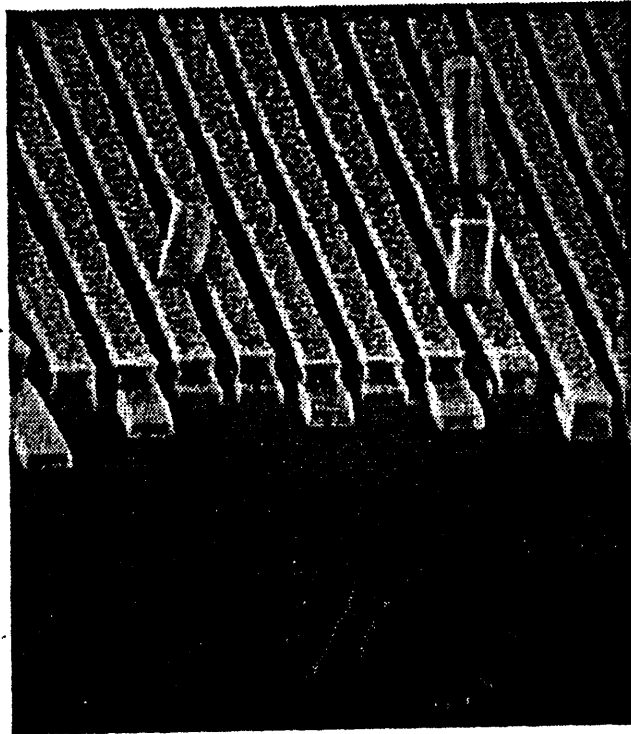
Figure 4-14: A SEM picture of oxide gratings formed by CHF_3 RIE with the PMMA grating mask.

resulting structure after the oxide mask is etched away in BOE is shown in Figure 4-15 along with the closed-up view of gratings. As desired, the gratings with vertical side-walls are formed as close to the ridge as one can hope, and no gratings are formed on the top nor on the side of the ridge. With this RWGDFB structure, the process can be continued into complete DFB lasers. The remaining steps are only dielectric deposition around the ridge, contact opening and metallization. Except the grating fabrication step, the above developed RWGDFB processing steps are identical to the conventional RWG processing steps. Consequently, it is believed easily integrable with already existing mature RWG fabrication technology.

InP gratings : CH_4/H_2 RIE
Λ = 230 nm
etch depth = 250 nm

230 nm
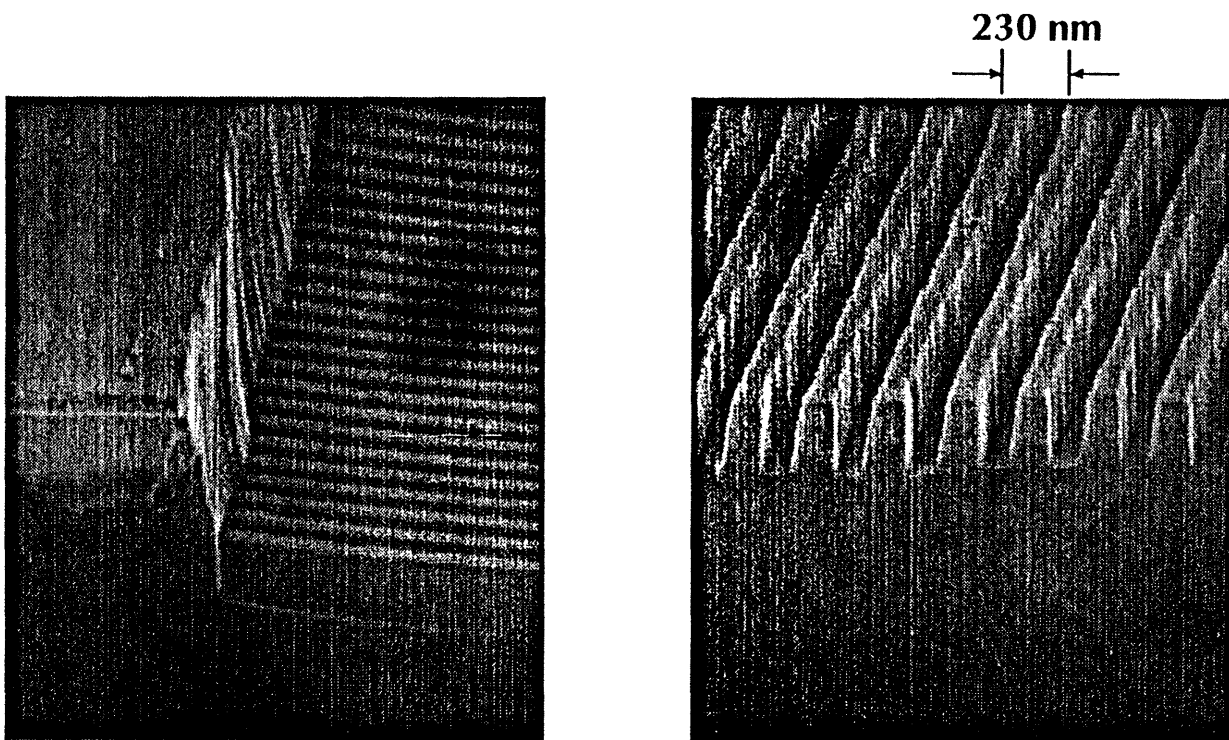
Figure 4-15: A SEM picture of the RWGDFB structure with 2500-Å-deep gratings formed right next to the ridge. The not-so-straight edge profile of the ridge is due to not-so-straight edge profile of the optical mask that was used for patterning the photoresist mask for oxide-stripe etching.

Chapter 5

Conclusion

5.1 Summary of Results

Efforts to realize high-performance InGaAlAs lasers with solid-source MBE technology have been discussed in the previous chapters. The key accomplishments of this research can be summarized as follows:

- The technique of growing high quality InGaAlAs on InP substrates by solid-source molecular beam epitaxy (MBE) was established. In particular, a systematic study was performed (Section 2.2) in which the optimal MBE growth conditions for InAlAs were determined.

- MBE-grown InGaAlAs bulk and quantum well (QW) structures were extensively characterized by double-crystal x-ray diffraction (DCXRD), transmission and PL measurements. These characterizations were performed as the means of assessing qualities of epitaxially grown materials as well as an investigative tool into some fundamental physical processes in semiconductors. In particular, DCXRD measurements were performed and a data-analysis procedure was developed in order to precisely determine the layer composition and thickness of compressively strained multiple QW (MQW) structures (Section 2.3). In addition, excitons in compressively strained MQW structures were investigated by transmission measurements which provided such quantitative parameters as

exciton radii, exciton binding energies, and in-plane reduced effective masses, and by photoluminescence (PL) measurements from which different optical processes due to free excitons, bound excitons, and band-to-band transitions were identified (Section 2.4).

- Compressively strained MQW laser diode structures were designed. The required QW composition and thickness were determined to be 40-Å-thick $In_{0.68}Ga_{0.32}As$ wells and 100-Å-thick $In_{0.52}Ga_{0.24}Al_{0.24}As$ barriers, which provide the desired lasing wavelength of 1.55 μm (Section 3.2.1). In addition, the maximum number of strained QWs and MBE growth temperature that do not result in the strain-relaxed dislocations were experimentally determined by PL characterization of strained MQWs with different total well numbers and grown at different growth temperatures (Section 3.2.2). Furthermore, the optimal graded-index separate confinement heterostructure (GRINSCH) structure was determined by the numerical calculation of the confinement factors for different GRINSCH layer thicknesses (Section 3.2.3).

- The laser structure designed above was grown by MBE, processed into broad-area devices, and characterized for threshold current densities and quantum efficiencies (Section 3.3.1). The lowest threshold current density achieved was 700 A/cm^2 for a laser structure with four QWs. Its estimated internal quantum efficiency and waveguide loss are 0.75 and 15 cm^{-1}, respectively. Some comparisons were made between these results and others found in the literature, and plausible explanations were given.

- The laser material was processed into ridge-waveguide (RWG) devices (Section 3.3.2). To the conventional RWG processing steps, a newly developed technique was added that utilizes an etch stop layer and a selective etching solution, and makes the ridge etching process easier and more accurate. The resulting RWG devices with 3 μm ridge width have a typical threshold current of 30 mA, the external quantum efficiency of about 0.21 for a facet, and far-field full-width-at-half-maximum (FWHM) of 15 °C.

- In order to realize lasers with the single longitudinal mode, a novel RWG distributed-feedback (RWGDFB) structure was proposed and the coupling coefficients possible with such a structure were numerically calculated (Section 4.2). Encouraged by the results of numerical calculations that indicate the proposed RWGDFB laser is feasible, the fabrication technology of a RWGDFB laser was successfully developed in which gratings were fabricated with x-ray lithography and CH_4/H_2-based reactive-ion etching (RIE).

5.2 MBE-Grown InGaAlAs Lasers for Future?

It is now time to re-evaluate the initial motivations of the present study based on the results achieved, and insight and knowledge developed during the study. The motivation for the present study (Section 1.1) can be simply summarized as why not attempt InGaAlAs lasers by MBE since InGaAlAs materials may have some advantages and there is a solid-source MBE available. Accordingly, our re-evaluation should answer following two questions: Is InGaAlAs really a desirable material system for lasers to be used in the fiber-optic application? Is solid-source MBE really the appropriate epitaxy technology for the same lasers?

The first question is basically the question of relative merits of InGaAlAs vs. InGaAsP, and its answer can be given in two parts as materials needed for semiconductor lasers can be divided into two categories: those for cladding layers and those for active and SCH layers. For cladding layers, there is virtually no advantage for InGaAlAs – or InAlAs as was used for claddings in this study – over InP. InP is easier to grow – if the epitaxy technique can handle it – than InAlAs since no lattice-matching is required, it is usually of much better quality than InAlAs that suffers from high susceptibility of Al to defects, and it is much more thermally conductive[1] than InAlAs. The efficient removal of heat generated in the active region is extremely

---

[1]The thermal resistivity is about 1.5 W^{-1}cm K for InP, and 15 W^{-1}cm K for InAlAs lattice-matched to InP. There seems to be no experimental data for the thermal resistivity of InAlAs, and it was estimated using the equation $W(x) = x\ W_{AC} + (1 - x)\ W_{BC} + C_{A-B}\ x(1 - x)$ given for the ternary $A_xB_{1-x}C$. The bowing parameter C_{A-B} was interpolated from the bowing parameters of InGaAs and AlGaAs. All the necessary parameter values are obtained from Reference [87].

important for thermal stability and reliability of laser devices. Furthermore, InAlAs is generally regarded not to be as reliable as InP [2] especially if the layer has to be exposed to the air during processing. This may be the biggest problem for InAlAs cladding layers since reliability is extremely important for fiber-optic lasers that are expected to be operational for tens of years under the ground or even the sea. Based on these observations, it is clear that lasers for the fiber-optic application should have at least InP claddings.

For the active and SCH layers, however, there is a little room for InGaAlAs-based lasers. This is especially the case for RWG devices with InGaAlAs QWs – but with InP claddings – in which processing steps do not expose any Al-containing layers in the SCH or active regions to the air and, consequently, the question of reliability of Al-containing layers is not too critical. With the vision of much extended fiber-optic networks of emerging national (and global) information infrastructure, it is anticipated that there will be a strong demand for large quantities of high-performance but low-price lasers. The most logical response to such demand is to use the most advanced laser layer structure, which requires very little additional cost for epitaxy, and use the simplest fabrication technology, which makes mass production with high yields possible. RWG InGaAlAs strained QW lasers are the perfect candidate for this scenario as InGaAlAs QWs have the advantage of larger conduction band offsets and RWG devices require very simple fabrication steps. In fact, the device performance of $1.3\,\mu m$ InGaAlAs strained MQW RWG lasers (with InP claddings) recently reported by Lasertron [78] clearly demonstrates the validity of this point; by utilizing the InGaAlAs strained QW layer structure and the RWG fabrication technology, Lasertron demonstrated low-cost lasers that satisfy all the requirements of the local-loop application. It is also interesting to note that the concept of RWGDFB lasers developed in Chapter 4 very nicely fits into this scheme since economically affordable DFB lasers such as RWGDFB can greatly enhance the system performance of fiber-optic networks in which now certain performance capabilities have to be sacrificed due to

---

[2]Although there seems to be no published data on the long-term reliability of InAlAs, some inference can be made from those on AlAs or AlGaAs [88, 89].

cost constraints. At the time of this thesis writing, there is a very strong indication that Lasertron is very interested in pursuing RWGDFB laser development based on their 1.3 μm InGaAlAs strained MQW device technology and our grating-fabrication technology with x-ray lithography developed in the present study.

With the above assertion that capability of growing InP layers is an absolute must for lasers to be used in the fiber-optic application, the answer to the second question if solid-source MBE is the appropriate epitaxy technology becomes obviously clear: The current solid-source MBE technology, in which high quality InP layers are not easily available, is not suitable for InP-based lasers. Instead, other technologies such as metalorganic chemical vapor deposition (MOCVD) or gas-source MBE should be pursued. In fact, it is this author's understanding that most of current advanced InP-based laser research and development is done with MOCVD and the trend will not change easily. One final footnote to this assertion is that there are new developments in solid-phosphorus MBE technology which indicate that obtaining InP layers of reasonable quality with solid-source MBE is not an impossible task [90]. This is certainly an interesting development since toxic gases required in MOCVD will most likely find higher and higher resistance against their use in research and production environments with the rapidly increasing environmental consciousness. Nonetheless, it remains questionable if solid-source MBE technology, clean it may be, will be ever able to replace MOCVD technology which already has a strong momentum as the epitaxy technology for InP-based lasers.

Bibliography

[1] C.K. Kao and G.A. Hockman, "Dielectric fiber surface waveguides for optical frequencies," *IEE*, Vol. 133, p. 1151, 1966.

[2] Kessler Marketing Intelligence, 31 Bridge St., Newport, RI.

[3] H. Raussch, "Green light on the superhighway," *Laser Focus*, p. 23, Mar. 1994.

[4] R.D. Dupuis, "An introduction to the development of the semiconductor laser," *IEEE J. Quantum Electron.*, Vol. 23, p. 651, 1987.

[5] R.N. Hall, "Injection lasers," *IEEE J. Quantum Electron.*, Vol. 23, p. 674, 1987.

[6] M.I. Nathan, "Invention of the injection laser at IBM," *IEEE J. Quantum Electron.*, Vol. 23, p. 679, 1987.

[7] N. Holonyak, "Semiconductor alloy lasers–1962," *IEEE J. Quantum Electron.*, Vol. 23, p. 684, 1987.

[8] R.H. Rediker, "Research at Lincoln Laboratory leading up to the development of the injection laser in 1962," *IEEE J. Quantum Electron.*, Vol. 23, p. 692, 1987.

[9] H. Temkin, K. Alavi, W.R. Wagner, T.P. Pearsall, and A.Y. Cho, "1.5–1.6-μm $Ga_{0.47}In_{0.53}As/Al_{0.48}In_{0.52}As$ multiquantum well lasers grown by molecular beam epitaxy," *Appl. Phys. Lett.*, Vol. 42, p. 845, 1983.

[10] E.T. Yu, J.O. McCaldin, and T.C. McGill, "Band offsets in semiconductor heterojunctions," *Solid State Physics*, Vol. 46, p. 1, 1992.

[11] H. Hirayama, Y. Miyake, and M. Asada, "Analysis of current injection efficiency of separate-confinement-heterostructure quantum-film lasers," *IEEE J. Quantum Electron.*, Vol. 28, p. 68, 1992.

[12] J.P. Loehr and J. Singh, "Theoretical studies of the effect of strain on the performance of strained quantum well lasers based on GaAs and InP technology," *IEEE J. Quantum Electron.*, Vol. 27 p. 708, 1991.

[13] See, for example, M.A. Herman and H. Sitter, *Molecular Beam Epitaxy: Fundamentals and Current Status.* New York: Springer-Verlag, 1989.

[14] J.C. Vlcek, "Molecular beam epitaxy growth and applications of graded bandgap InGaAlAs semiconductor alloys," Ph.D. thesis, Dept. of Electrical Engineering and Computer Science., MIT, 1991.

[15] "molly MBE Process Control System," EPI, St. Paul, MN.

[16] *The MBE Manual,* Edt. by I. Hoshino. Compound Semiconductor Materials and Device Group, Dept. of Electrical Engineering and Computer Science, MIT.

[17] K.A. Prior, G.J. Davies, and R. Heckingbottom, "The thermodynamics of oxygen incorporation into III-V semiconductor compounds and alloys in MBE," *J. Cryst. Growth*, Vol. 66, p. 55, 1984.

[18] A.G. Norman, R.E. Mallard, I.J. Murgatroyd, G.R. Booker, A.H. Moore, and M.D. Scott, "TED, TEM and HREM studies of atomic ordering in $Al_xIn_{1-x}As(x\sim0.5)$ epitaxial layers grown by organometallic vapour phase epitaxy," *Inst. Phys. Conf. Ser.*, No. 87, p. 77, 1987.

[19] W.P. Hong, P.K. Bhattacharya, and J. Singh, "Nonrandom alloying $In_{0.52}Al_{0.48}As/InP$ grown by molecular beam epitaxy," *Appl. Phys. Lett.*, Vol. 50, p. 618. 1987.

[20] W.-Y. Choi and C.G. Fonstad, "Growth optimization of molecular beam epitaxy-grown InAlAs on InP," to appear in *J. Vac. Sci. Technol.*, Mar./Apr., 1994.

[21] N. Higushi, T. Ishikawa, K. Imanishi, and K. Kondo, "Doping characteristics of Si into molecular-beam-epitaxially grown InAlAs layers," *J. Vac. Sci. Technol.,* B 6, p. 2802, 1991.

[22] D.F. Welch, G.W. Wicks, and L.F. Eastman, P. Parayanthal, and F.H. Pollak, "Improvement of optical characteristics of $Al_{0.48}In_{0.52}As$ grown by molecular beam epitaxy," *Appl. Phys. Lett.,* Vol. 46, p. 169, 1985.

[23] E. Tournié, Y.-H. Zhang, N.J. Pulsford, and K. Ploog, "Structural and optical properties of $Al_{0.48}In_{0.52}As$ layers grown on InP by molecular beam epitaxy: Influence of the substrate temperature and of a buffer layer," *J. Appl. Phys.,* Vol. 70, p. 7362, 1991.

[24] W.-Y. Choi and C.G. Fonstad, "Determination of the layer structure of embedded strained InGaAs multiple quantum wells by high resolution x-ray diffraction," *Appl. Phys. Lett.,* Vol. 62, p. 2815, 1993.

[25] J.M. Vandenberg, R.A. Hamm, M.B. Panish, and H. Temkin, "High-resolution x-ray diffraction studies of InGaAs(P)/InP superlattices grown by gas-source molecular-beam epitaxy," *J. Appl. Phys.,* Vol. 62, p. 1278, 1987.

[26] A. Segmüller and A. E. Blakeslee, "X-ray diffraction from one-dimensional superlattices in $GaAs_{1-x}P_x$ Crystals," *J. Appl. Cryst.,* Vol. 6, p. 19, 1973.

[27] V. Swaminathan and A.T. Macrander, *Material Aspects of GaAs and InP-Based Structures.* Englewood Cliffs, N.J.: Prentice Hall, 1991, Chap. 3.

[28] W.-Y. Choi, Y. Hirayama, and C.G. Fonstad, "Absorption and photoluminescence investigations of excitonic transitions in compressively strained InGaAs/InGaAlAs multiple quantum wells," in *Proc. 5th Intern. Conf. on InP and Relat. Mater.,* Paris, France, 1993, p. 477.

[29] Y. Hirayama, W.-Y. Choi, and C.G. Fonstad, "Optical study on exciton in InGaAs/InGaAlAs quantum well structures," *Tech. Report of IEICE* (in Japanese), OQE93-42, p. 21, 1993.

[30] Y. Hirayama, W.-Y. Choi, L.H. Peng, and C.G. Fonstad, "Absorption spectroscopy on room temperature excitonic transitions in strained layer InGaAs/InGaAlAs multiple quantum-well structures," *J. Appl. Phys.*, Vol. 74, p. 170, 1993.

[31] B.V. Shanabrook, O.J. Glembocki, and W.T. Beard, "Photoreflectance modulation mechanisms in GaAs-$Al_xGa_{1-x}As$ multiple quantum wells," *Phys. Rev.*, B 35, p. 2540, 1987.

[32] C.G. Van de Walle, "Band lineups and deformation potentials in the model-solid theory," *Phys. Rev.*, B 35, p. 8154, 1987.

[33] M. Sugawara, T. Fujii, S. Yamazaki, and K. Nakajima, "Theoretical and experimental study of the optical-absorption spectrum of exciton resonance in $In_{0.53}Ga_{0.47}As$/InP quantum wells," *Phys. Rev.*, B 42, p. 9587, 1990.

[34] G. Bastard, E.E. Mendez, L.L. Chang, and L. Esaki, "Exciton binding energy in quantum wells," *Phys. Rev.*, B 26, p. 1974, 1982.

[35] J. Christen and D. Bimberg, "Line shapes of intersubband and excitonic recombination in quantum wells: Influence of final-state interaction, statistical broadening, and momentum conservation," *Phys. Rev.*, B 42, p. 7213, 1990.

[36] G. Bastard C. Delalande, M.H. Meynadier, P.M. Frijlink, and M. Voos, "Low-temperature exciton trapping on interface defects in semiconductor quantum wells," *Phys. Rev.*, B 29, p. 7042, 1984.

[37] J.P. Bergman P.O. Holtz, B. Monemar, M. Sundaram, J.L. Merz, and A.C. Gossard, "Temperature dependent studies of the radiative recombination in GaAs/AlGaAs multiple quantum wells," *Inst. Phys. Conf. Ser.*, Vol. 123, p. 73, 1991.

[38] H.K. Choi and C.A. Wang, "InGaAs/AlGaAs strained single quantum well diode lasers with extremely low threshold current density and high efficiency," *Appl. Phys. Lett.*, Vol. 57, p. 321, 1990.

[39] J.D. Ralston, S. Weisser, I. Esquivias, E.C. Larkins, J. Rosenzweig, P.J. Tasker, J. Fleissner, "Control of differential gain, nonlinear gain, and damping factor for high-speed application of GaAs-based MQW lasers," *IEEE J. Quantum Electron.*, Vol. 29, p. 1648, 1993.

[40] See, for example, *Quantum Well Lasers*, Edt. by P. Zory. San Diego: Academic Press, 1993.

[41] M.P.C.M. Krijn, G.W. 't Hooft, M.J.B. Boermans, P.J.A. Thijs, T. van Dongen, J.J.M. Binsma, L.F. Tiemeijer, and C.J. van der Peol, "Improved performance of compressively as well as tensile strained quantum-well lasers," *Appl. Phys. Lett.*, Vol. 61, p. 1772, 1992.

[42] S.W. Corzine, R.H. Yan, and L.A. Coldren, "Optical gain in III-V bulk and quantum well semiconductors," in *Quantum Well Lasers*, Edt. by P. Zory. San Diego: Academic Press, 1993.

[43] S.W. Corzine, R.H. Yan, and L.A. Coldren, "Theoretical gain in strained In-GaAs/AlGaAs quantum wells including valence-band mixing effects," *Appl. Phys. Lett.*, Vol. 57, p. 2835, 1990.

[44] K.Y. Lau, "Ultralow threshold quantum well lasers," in *Quantum Well Lasers*, Edt. by P. Zory. San Diego: Academic Press, 1993.

[45] M.G.A. Bernard and G. Duraffourg, "Laser conditions in semiconductors," *Phys. Status Solidi*, Vol. 1, p. 699, 1963.

[46] J.W. Mathews and A.E. Blakeslee, "Defects in epitaxial multilayers," *J. Cryst. Growth*, Vol. 27, p. 118, 1974.

[47] B.W. Dodson and J.Y. Tsao, "Relaxation of strained-layer semiconductor structures via plastic flow," *Appl. Phys. Lett*, Vol. 51, p. 1325, 1987.; Erratum: Vol. 52, p. 852, 1988.

[48] B.W. Dodson and J.Y. Tsao, "Structural relaxation in metastable strained-layer semiconductors," *Annu. Rev. Mater. Sci.*, Vol. 19, p. 419, 1989.

[49] B.R. Bennett and J.A. del Alamo, "High quality InGaAs/InP and InAlAs/InP heterostructures beyond the Matthews-Blakeslee critical layer thickness," in *Proc. 4th Int. Conf. on InP and Relat. Mater.*, New Port, RI, 1992, p. 650.

[50] M. Gal, P.C. Taylor, B.F. Usher, and P.J. Orders, "Photoluminescence in strained InGaAs/GaAs heterostructures," *J. Appl. Phys.*, Vol. 62, p. 3898, 1987.

[51] J. Nagle, S. Hersee, M. Krakowski, T. Weil, and C. Weisbuch, "Threshold current of single quantum well lasers: The role of the confining layers,", *Appl. Phys. Lett.*, Vol. 49, p. 1325, 1986.

[52] J.C. Vlcek, and C.G. Fonstad, "Precise computer control of the MBE process - Application to graded InGaAlAs/InP alloys," *J. Cryst. Growth*, Vol. 111, p. 56, 1991.

[53] R. Nagarajan, T. Fukushima, M. Ishikawa, J.E. Bowers, R.S. Geels, and L.A. Coldren, "Transport limits in high-speed quantum-well lasers: experiment and theory," *IEEE Photon. Technol. Lett.*, Vol. 4, p. 121, 1992.

[54] W.T. Tsang, M.C. Wu, L. Yang, Y.K. Chen, and A.M. Sergent, "Strained-layer 1.5 μm wavelength InGaAs/InP multiple quantum well lasers grown by chemical beam epitaxy," *Electron. Lett.*, Vol. 26, p. 2035, 1990.

[55] W.T. Tsang, F.S. Choa, M.C. Wu, Y.K. Chen, and A.M. Sergent, "Very low threshold single quantum well graded-index separate confinement heterostructure InGaAs/InGaAsP lasers grown by chemical beam epitaxy," *Appl. Phys. Lett.*, Vol. 58, p. 2610, 1991.

[56] J.S. Osinski, Y. Zou, P. Grodzinski, A. Mathur, and P.D. Dapkus, "Low-threshold-current-density 1.5 μm lasers using compressively strained InGaAsP quantum wells," *IEEE Photon. Technol. Lett.*, Vol. 27, p. 1440, 1991.

[57] P.J.A. Thijs, L.F. Tiemeijer, P.I. Kuindersma, J.J.M. Binsma, and T.V. Dongen, "High-performance 1.5 μm wavelength InGaAs-InGaAsP strained quantum well lasers and amplifiers," *IEEE J. Quantum Electron.*, Vol. 27, p. 1426, 1991.

[58] A. Kasukawa, R. Bhat, C.E. Zah, M.A. Koza, and T.P. Lee, "Very low threshold current density 1.5 μm GaInAs/AlGaInAs graded-index separate-confinement-heterostructure strained quantum well laser diodes grown by organometallic chemical vapor deposition," *Appl. Phys. Lett.*, Vol. 59,. p. 2486, 1991.

[59] M.J. Mondry, Z.M. Chuang, M.G. Peters, and L.A. Coldren, "Low threshold current density 1.5 μm (In,Ga,Al)As quantum well lasers grown by MBE," *Electron. Lett.*, Vol. 28, p. 1471, 1992.

[60] W.T. Tsang, F.K. Reinhart, J.A. Ditzenberger, "The effect of substrate temperature on the current threshold of GaAs-Al$_x$Ga$_{1-x}$As double-heterostructure lasers grown by molecular beam epitaxy," *Appl. Phys. Lett.*, Vol. 36, p. 118, 1980.

[61] W.T. Tsang in *The Technology and Physic of Molecular Beam Epitaxy*, Edt. by E.H.C. Parker. New York: Plenum, 1985.

[62] K. Xie, C.R. Wie, J.A. Varriano, and G.W. Wicks, "Interface traps and interface recombination in AlGaAs/GaAs quantum well laser diodes," *Appl. Phys. Lett*, vol. 60, p. 428, 1992.

[63] W.-Y. Choi and C.G. Fonstad, "Photoluminescence and x-ray diffraction studies of MBE-grown compressively strained InGaAs and InGaAlAs quantum wells for 1.55 μm laser diode applications," *J. Cryst. Growth*, Vol. 175, p. 555, 1993.

[64] H. Temkin, M.B. Panish, R.A. Logan, and J.P. van der Ziel, "$\lambda = 1.5$ μm InGaAsP ridge lasers grown by gas source molecular beam epitaxy", Vol. 45, p. 330, 1984.

[65] W.Y. Choi, T.P.E. Broekaert, and C.G. Fonstad, "MBE-grown InGaAlAs 1.5 μm MQW ridge waveguide laser diodes with AlAs etch stop layers," *Electron. Lett.*, Vol. 29, p. 483, 1993.

[66] T.P.E. Broekaert and C.G. Fonstad, "AlAs etch-stop layers for InGaAlAs/InP heterostructure devices and circuits", *IEEE Trans. Electron Devices*, Vol. 39, p. 533, 1992.

[67] H. Kogelnik and C.V. Shank, "Coupled-wave theory of distributed feedback lasers," *J. Appl. Phys.*, Vol. 43, p. 2327, 1972.

[68] G.P. Agrawal and N.K. Dutta, *Long-wavelength semiconductor lasers.* New York: Van Nostrand Reinhold Co., 1986, p. 304,

[69] J. Hong, Weiping Huang, and T. Makino, "On the transfer matrix method for distributed-feedback waveguide devices," *J. Lightwave Technol.*, Vol. 10, p. 1860, 1992.

[70] S. Jüngling and J.C. Chen, "A study and optimization of eigenmode calculations using imaginary beam propagation method," to be published in *IEEE J. Quantum Electron.*

[71] K. Handa, S.T. Peng, and T. Tamir, "Improved perturbation analysis of dielectric gratings," *Appl. Phys.*, Vol. 5, pp. 325-328, 1975.

[72] G.M. Alman, L.A. Molter, H. Shen, and M. Dutta, "Refractive index approximations from linear perturbation theory for planar MQW waveguides," *IEEE J. Quantum Electron.*, Vol. 28, pp. 650-657, 1992.

[73] K. Sato, S. Sekine, Y. Kondo, and M. Yamamoto, "Simultaneous operation of ten-channel tunable DFB laser arrays using strained-InGaAsP multiple quantum wells," *IEEE J. Quantum Electron.*, Vol. 29, pp. 1805-1809, 1993.

[74] C.H. Henry, L.F. Johnson, R.A. Logan, and D.P. Clarke, "Determination of the refractive index of InGaAsP epitaxial layers by mode line luminescence spectroscopy," *IEEE J. Quantum Electron.*, Vol. 21, pp. 1887-1992, 1985.

[75] H. Soda, Y. Kotaki, H. Sudo, H. Ishikawa, S. Yamakoshi, and H. Imai, "Stability in single longitudinal mode operation in GaInAsP phase-adjusted DFB lasers," *IEEE J. Quantum Electron.*, Vol. 23, pp. 804-814, 1987.

[76] G.J. Van Gurp and J.M. Jacobs, "Dry etching of InP, applied to laser devices," *Philips J. Res,* Vol. 44, pp. 211-239, 1989.

[77] V.V. Wong, W.Y. Choi, J.M. Carter, C.G. Fonstad, H.I. Smith, Y. Chung, and N. Dagli, "Ridge-waveguide sidewall-grating distributed feedback structures fabricated by x-ray lithography," *J. Vac. Scien. Technol.,* B 11, p. 2621, 1993.

[78] D. Darby, Z. Wang, and P. Whitney, "Reliable low cost lasers for local loop applications," LEOS93, San Jose, CA, 1993.

[79] W.T. Tsang, R.M. Kapre, R.A. Logan, and T. Tanbun-Ek, "Control of lasing wavelength in distributed feedback lasers by angling the active stripe with respect to the grating," *IEEE Photon. Technol. Lett.,* Vol. 5, p. 978, 1993.

[80] S. Ogita, Y. Kotaki, M. Matsuda, Y. Kuwahara, and H. Ishkawa, "Long-cavity multiple-phase-shift distributed feedback laser diode for linewidth narrowing," *IEEE J. Quantum Electron.,* Vol. 8, p. 1596, 1990.

[81] M. Okai, T. Tsuchiy, K. Uomi, and T. Harada, "Corrugation-pitch-modulated MQW-DFB lasers with narrow spectral linewidth," *IEEE J. Quantum Electron.,* Vol. 27, p. 1767, 1991.

[82] S. Nilsson, T. Kjellberg, T. Klinga, J. Wallin, K. Streubel, and R. Shatz, "DFB laser with nonuniform coupling coefficient realized by double-layer buried gratings," *IEEE Photon. Technol. Lett.,* Vol. 5, p. 1128, 1993.

[83] J. Ferrera, V.V. Wong, S. Rishton, V. Boegli, E.H. Anderson, D.P. Kern, and H.I. Smith, "Spatial-phase-locked electron-beam lithography: initial test results," *J. Vac. Sci. Technol.,* B 11, p. 2342, 1993.

[84] T. Kjellberg and R. Schatz, "The effect of stitching errors on the spectral characteristics of DFB lasers fabricated using electron beam lithography," *J. Lightwave Technol.,* Vol. 10, p. 1256, 1992.

[85] A. Moel, M.L. Schattenburg, J.M. Carter, and H.I. Smith, "A compact, low-cost system for sub-100 nm x-ray lithography," *J. Vac. Sci. Technol.,* B 8, p. 1648, 1990.

[86] R.A. Ghanbari, W. Chu, E.E. Moon, M. Burkhardt, K. Yee, D.A. Antoniadis, H.I. Smith, M.L. Schattenburg, K.W. Rhee, R. Bass, M.C. Peckerar and M.R. Melloch, "Fabrication of parallel quasi-one-dimensional wires using a novel conformable x-ray mask technology," *J. Vac. Sci. Technol.,* B 10, p. 3196, 1992.

[87] V. Swaminathan and A.T. Macrander, *Material Aspects of GaAs and InP-Based Structures.* Englewood Cliffs, N.J.: Prentice Hall, 1991, p. 15 and p. 33.

[88] J.M. Dallesasse, P. Gavrilovic, N. Holonyak, R.W. Kaliski, D.W. Nam, E.J. Vesey, and R.D. Burnham, "Stability of AlAs in $Al_xGa_{1-x}As$-AlAs-GaAs quantum well heterostructures," *Appl. Phys. Lett.,* Vol. 56, p. 2436, 1990.

[89] J.M. Dallesasse, N. El-Zein, N. Holonyak, K.C. Hsieh, R.D. Burnham, and R.D. Dupuis, "Environmental degradation of $Al_xGa_{1-x}As$-GaAs quantum-well heterostructures," *Appl. Phys. Lett.,* Vol. 68, p. 2235, 1990.

[90] J.N. Baillargeon, A.Y. Cho, R.J. Fischer, P.J. Pearah, and K.Y. Cheng, "Electrical and optical characteristics of InP grown by MBE using a valved-phosphorus cracking cell," Presented in *1993 North American MBE Conf.,* Palo Alto, CA; also to appear in *J. Vac. Sci. Technol.*